“Therapeutic reprogramming of bone marrow derived mesenchymal stem cells during influenza infection is mediated by type I interferon signaling and interleukin 11”

Inaugural Dissertation
submitted to the Faculty of Medicine
in partial fulfillment of the requirements
for the PhD-Degree
of the Faculties of Veterinary Medicine and Medicine
of the Justus Liebig University Giessen

by
Barroso, Margarida Maria
of
Lisboa, Portugal

Giessen, July 12th, 2023

From the Department of Medicine V, Infectious Diseases, and Infection Control
of the Faculty of Medicine of the Justus Liebig University Giessen
Director: Prof. Dr. Susanne Herold, PhD

Chair: Prof. Dr. Klaus-Dieter Schlüter
Vice-chair and Co-Supervisor: Prof. Dr. Friedemann Weber
First Reviewer and Supervisor: Prof. Dr. Susanne Herold, PhD
Second Reviewer: Prof. Dr. med. Dr. rer. nat. Burkhard Tümmler

Date of Doctoral Defense: July 12th 2023

TABLE OF CONTENTS

I. INTRODUCTION 4

Biology of the lung 4

Anatomy of the respiratory system in mice and humans 4

Stem cell niches present in the distal adult lung 4

Organoid models 6

Acute Respiratory Distress Syndrome (ARDS) 7

Clinical aspects 7

Influenza A Virus (IAV) infection-induced ARDS 8

Molecular mechanisms in viral injury and repair 9

Mesenchymal Stem Cells (MSC) 11

Origin, definition, and characteristics 11

Immunomodulatory properties 13

MSC as a promising therapy for ARDS 15

II. AIMS 19

III. MATERIALS AND METHODS 20

Mice strains, harbouring and scoring 20

Influenza-A virus (IAV) strains 21

Flow Activated Cell Sorting (FACS) 21

Isolation and culture of primary cells and cell lines 21

Primary AEC 21

Lung-derived mesenchymal stem cells (lung-MSC) 22

BM-MSC 23

3T3 cell line 24

Routine experiments 24

BM-MSC phenotype and differentiation ability 24

Virus titration assay 25

In-vitro experiments 26

AEC infection 26

MSC co-cultured with AEC 26

Cell proliferation, infection, and viability assays 27

Cell priming, labelling and treatment 27

Enzyme-Linked ImmunoSorbent Assay (ELISA) 28

RNA isolation 28

Ex-vivo experiments 28

BALO generation and staining 28

BALO microinjection – preparation, infection, and cell injection 29

In-vivo experiments 30

Intra-tracheal IAV infection 30

Intra-tracheal cell application 30

Lung preparation and BAL collection 30

Recovery of labeled BM-MSC 31

Bulk-RNA sequencing 31

Microscopy 32

Histological assessment of the lung 32

Statistics 33

IV. RESULTS 34

IV.1. Lung-MSC can respond to IAV-infection *in vivo* and exhibit protective effects towards infected AEC *in vitro* 34

IV.2. Bone-marrow isolated mesenchymal stem cells have stem cell potential and exert similar AEC protective effects as lung-MSC 38

IV.3. BM-MSC change their phenotype after being exposed to IAV and depend on external activation to potentiate their protective effects 42

IV.4. Intra-tracheally delivered BM-MSC show protective effects towards AEC and anti-viral properties *in vivo* 50

IV.5. Type I interferon pathway plays a key role in BM-MSC anti-viral potential 54

IV.6. Activated BM-MSC release IL-11 and increase AEC resilience via a protective type I IFN/IL-11 signaling loop 59

V. DISCUSSION 65

VI. SUMMARY 70

VII. ZUSAMMENFASSUNG 71

VIII. REFERENCES 73

IX. SUPPLEMENTS 94

IX.1. Chemicals and Consumables 94

IX.2. List of Abbreviations 97

IX.3. List of Figures 100

IX.4. List of Tables 108

IX.5. Affirmation 109

IX.6. Curriculum vitae 110

IX.7. Acknowledgments 113

I. Introduction

Biology of the lung

Anatomy of the respiratory system in mice and humans

The respiratory system is structured, complex, and allows effective gas exchange between the blood stream and the external environment. It comprises diverse anatomical regions populated by up to 40 different cell types (epithelial, vascular, mesenchymal, neuroendocrine, and immune cells) that work together for the perfect function of the lung [1]. Understanding the developmental processes and homeostasis is crucial to study lung diseases and to formulate therapies that could trigger cell regeneration [1], [2].

Anatomically, the respiratory system can be separated in two associated zones: the conducting zones (nose to bronchioles) that form a route for the inhaled gases, and the respiratory zone (alveolar duct to alveoli) where gas exchange occurs [3]. At the end of the respiratory zone, alveolar sacs allow for efficient gas exchange, through capillaries, due to the vast surface area that in humans reaches approximately 143 square meters (m^2) [4].

In lung-related research, animal models have been developed to study most of the common human lung disorders including idiopathic pulmonary fibrosis, chronic obstructive pulmonary disease (COPD) and acute lung injury (ALI). Although animal research presents inherent limitations, a higher number of mice can be bred and studied in shorter time periods, with several genetic modifications being relatively easy to perform, contrary to human-derived models [5], [6].

Stem cell niches present in the distal adult lung

The alveolar niche shows low self-renewal during homeostasis. However, upon damage, distinct cell populations in the alveolar compartment can respond in order to restore homeostasis by activating molecular pathways of self-renewal and differentiation [1], [7]. Several cell populations are involved in this response, including alveolar epithelial cells (AEC), alveolar endothelial cells (AEnC), alveolar mesenchyme, and immune cells (Figure **I-1**).

In the alveolar epithelium, AEC type 1 (AEC1) mediate gas exchange and cover more than 90% of the alveolar surface, while AEC type 2 (AEC2) are responsible for surfactant production, essential to prevent alveolar collapse by reducing the surface tension of the alveolar space [8]. In adult mice, the AEC2 population expressing Axin2, capable of

responding to Wnt and fibroblast growth factor 7 (FGF-7) signaling, can act as a self-renewing stem cell population and is responsible for AEC1 re-population after acute injury [9], [10].

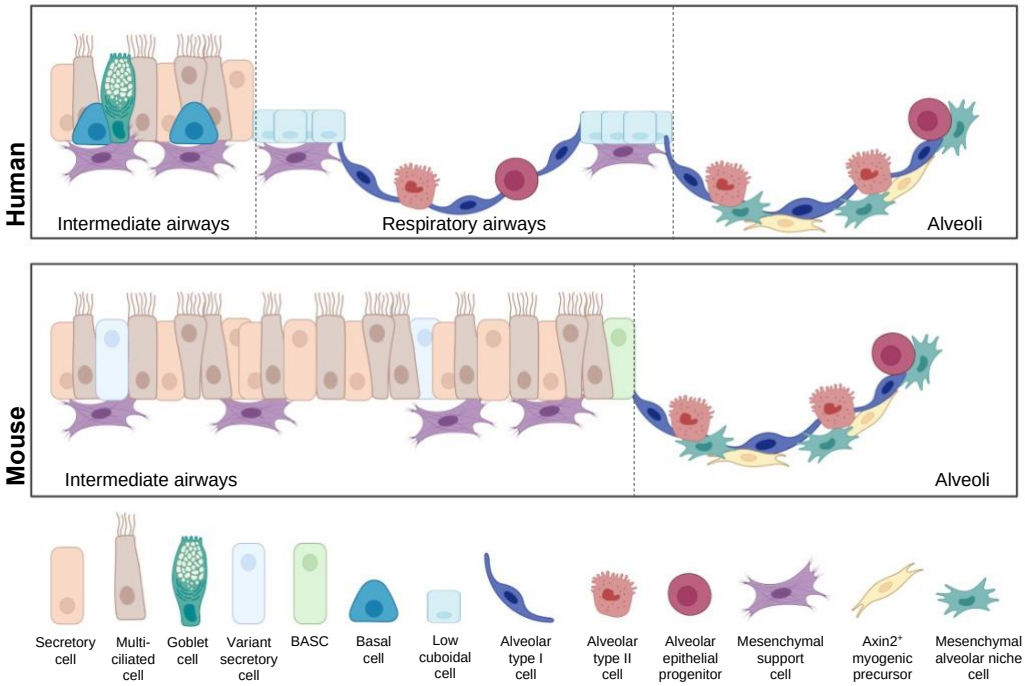

Figure I-1. Lung cell lineages involved in lung repair and regeneration. In both human and mouse, the lung architecture and cell lineages are similar, with both species having alveolar type 1 and alveolar type 2 epithelial cells, as well as secretory cells, multi-ciliated cells, and various mesenchymal lineages (mesenchymal support cell, Axin2$^+$ myogenic precursor and mesenchymal alveolar niche cells). However, humans have a pseudostratified epithelium in the intermediate airways (containing secretory, goblet and ciliated cells) while mice do not have respiratory bronchioles and the intermediate airways exhibit a pseudostratified nature without basal cells. The murine distal region contains a population of bronchoalveolar stem cell (BASC). Adapted from M.C. Basil et al., 2020 [1]. Created using BioRender.com.

Distal airway epithelial cells also get activated after severe lung injury [11]. For instance, club-like progenitors expressing H2-K1 have high proliferative capacity and are suggested to give rise to AEC1 and AEC2 after bleomycin injury [12]. In distal airway epithelium, small populations of progenitor cell types have been reported to also contribute to injured-tissue regeneration. Variant club/secretory cells (v-club cells) that lack cytochrome Cyp2f2 expression are resistant to naphthalene injury and can give rise to club and ciliated cells during homeostasis [13]. A bleomycin injured- v-club cell population expressing uroplakin 3A was also found to contribute to AEC1 and AEC2 regeneration [14]. Bronchoalveolar stem cells (BASC), located at the branching points between distal murine airways and the alveolus (Figure **I-1**), co-express secretoglobin family 1A member 1 (SCGB1A1) (secretory cell marker) and pro-surfactant protein C (SFTPC) (AEC2 marker) [15], [16] and contribute to both airway and alveolar epithelium regeneration after influenza damage [17]. Notably, stem cell antigen-1 (Sca-1) was also identified as a BASC maker for flow cytometry isolation [18].

Lineage-negative epithelial progenitors (LNEPs, also known as distal airway stem cells) were originally identified by the expression of the distal integrin ß$^{+}$/CD200^{+} [19] and sex determining region Y-box transcription factor (Sox) 2 [20] and later proved to also be composed of cells expressing and lacking transformation related protein 63 (Trp63) [21]. Within Trp63^{+} LNEPs, keratin 5 (Krt5) positive cells are shown to appear after virus injury, generating pods of Krt5^{+} basal-like cells in heavily damaged areas [19]. Although presenting an initial protective effect, Krt5^{+} basal cell pods have limited AEC2 differentiation capacity, leading to permanent cystic structure formation in the alveolar compartment [20].

Resident and circulating leukocytes can also drive repair and regeneration by releasing, among other factors, inflammatory cytokines (like interleukin 1 – IL-1 – and tumor necrosis factor alpha – TNFα) [22], [23]. However, the crosstalk between AEC and resident or circulating leukocytes has not been extensively studied. Macrophages can impact survival and self-renewal of AEC2 and recruited monocytes expressing C-C motif chemokine receptor 2 have also been linked to alveolar repair after lung fibrosis [24], [25].

A complex population of mesenchymal cell types present in the alveolus also plays an active role in alveolar regeneration by interacting with both epithelium and endothelium [26]. For instance, mesenchymal cells expressing platelet-derived growth factor receptor alpha (PDGFRα or CD140a) are found to support AEC2 self-renewal and differentiation (in an organoid co-culture system) by activating multiple signaling pathways such as Fgf-7, bone morphogenetic proteins (Bmp), and IL-6 [1], [9]. Recently, this cell population was further defined as a cluster of fibroblasts co-expressing Axin2 and Pdgfrα, localized close to AEC2 (Figure **I-1**) [27]. The mesenchyme also has a critical role in the function of distal airway epithelium by providing signaling cues via Wnt-Fgf-10 signaling, indispensable for stem cell response during injury [28].

Organoid models

Traditional cell cultures models have been extensively used in basic pulmonary research, however, translating cell cultures findings to *in vivo* settings has been challenging [29]. Recent three-dimensional (3D) approaches can better mimic specific microenvironments and cell-to-cell interactions, compared to two-dimensional (2D) cell cultures. “Organoids” – a 3D mini organ – replicate histological and some functional aspects of the *in vivo* tissue and can be used to study a variety of mechanisms like embryonic development, pathogenesis, disease modeling and drug discovery, as well as cell niches interactions [30], [31]. *Ex vivo* formation of lung organoids requires the isolation of specific stem cell populations, the use of gels that

contain a mixture of extracellular matrix components and air-liquid interface culture systems that stimulate organoid growth, polarization, and cell differentiation [32]. A specialized *in vitro* cell culture technique has been developed by Vazquez-Armendariz *et al.* to promote the formation of 3D structures able to recapitulate morphological and functional characteristics of the lung [33]. This model describes a protocol for isolation and co-culture of murine progenitor cells with BASC signature, together with lung-resident mesenchymal stem cells to form bronchoalveolar lung organoids (BALO), exhibiting distinct bronchiolar-like and alveolar-like structures after 21 days of culture. Culture enrichment with $EpCAM^{high}$ $CD24^{low}$ $Sca\text{-}1^{+}$ progenitor cells create higher BALO numbers, lowering alveolosphere- and bronchiolosphere-forming progenitor cells, making this model ideal to mimic lung structure and cell complexity. Organoids derived from adult stem and progenitor cells not only translate structural cues for regeneration after injury but also allow to study stem cell crosstalk and lineage commitment [34]. In the described model, lung mesenchymal stem cells ($CD45^{-}$ $CD31^{-}$ $EpCAM^{-}$ $Sca\text{-}1^{+}$) are indispensable for BALO formation and contain $PDGFR\alpha^{+}$ progenitor cells capable of differentiating into lipo- and myo-fibroblasts [33]. More broadly, lung organoid models not only allow to investigate lung stem cell function but also monitor their behavior after different stimulus. Although lung organoid culture systems are still being developed to become increasingly more complex, it is already possible to extend their use to therapeutic applications [35].

Acute Respiratory Distress Syndrome (ARDS)

Clinical aspects

Acute respiratory distress syndrome (ARDS) can occur after severe bacterial or viral pneumonia, but also from non-pulmonary sepsis, aspiration of gastric content and major trauma [36]. It is characterized clinically by acute hypoxemia, non-cardiogenic pulmonary edema, increased lung stiffness and breathing difficulty, which requires positive pressure ventilation [37]. Even when it is estimated that 38.5% of 200 000 annual cases of ARDS (United States of America) result in hospital mortality, ARDS diagnosis is still underestimated by some clinicians [36]. To overcome this, the 2012 Berlin definition and the 2016 Kigali modification established that clinical ARDS is characterized by (1) respiratory failure that occurs within one week of a known trigger (or worsening of respiratory symptoms) that (2) cannot be fully explained by cardiac malfunction or volume overload (excluded with an echocardiography to discard hydrostatic edema), it should have (3) observable bilateral opacities on chest radiograph or ultrasonography scan (that aren't fully explained by effusion,

collapse or nodules) and present with (4) acute onset of hypoxemia defined as PaO_2/FiO_2[1] <300 mmHg and SpO_2[2]/FiO_2 <315) [38], [39]. In 2021, an expansion to the Berlin definition was proposed to accommodate earlier recognition of symptoms, by incorporating patients using high-flow nasal oxygen of at least 30 L/min [40].

Influenza A Virus (IAV) infection-induced ARDS

Influenza viruses have annually a significant impact on human health, with seasonal influenza A virus (IAV) infection being a recurrent epidemic disease [41]. IAV primarily targets airway cells and AEC and can be clinically identified by the presence of bilateral infiltrates and hypoxemia.

IAV is an enveloped negative-sense single-stranded ribonucleic acid (RNA) virus, containing eight RNA segments that encode for RNA polymerase subunits, viral glycoproteins (neuraminidase – NA – and hemagglutinin – HA), viral nucleoprotein (NP), matrix proteins (M1 and M2), non-structural protein NS1, and nuclear export protein (NS2 or NEP) [42]. The course of IAV infection begins with viral dissemination on the airway and alveolar epithelium. The HA protein binds to the airway or alveolar epithelium by interacting with sialic acid residues linked to cell-surface glycans, allowing the virion to enter the cell by endocytosis; the viral core dissociates, and the ribonucleoprotein complex is transported to the nucleus to begin the replication. The newly formed HA binds to sialic acid receptors on the cell surface and virus are then free to infect other cells once NA cleaves the sialic links [43]. Early on, the virus inhibits the amiloride-sensitive epithelial sodium channels (ENaCs), triggering fluid accumulation in the alveolar lumen [44]. Infection-associated apoptosis and necrosis and denudation of the airways are direct viral-induced pathologies observed in ARDS patients. Immune responses also contribute to the worsening of ARDS outcome by local (and systemic) cytokine production, infiltration of neutrophils and inflammatory monocytes, exuberant T-cell responses, and extracellular matrix degradation [45]. Histopathology from ARDS patients show evidence of alveolar inflammation and injury, related to increased pulmonary capillary permeability [46]. ARDS patients often present impaired gas exchange with arterial hypoxemia, as a result of ventilation perfusion mismatch, right-to-left intrapulmonary shunting, impaired carbon dioxide release, and increase in pulmonary dead space [36], [46].

[1] PaO_2 – partial pressure of arterial oxygen, FiO_2 – fraction of inspired oxygen
[2] SpO_2 – peripheral capillary oxygen saturation

Molecular mechanisms in viral injury and repair

The molecular response to viral infections is complex and involves multiple key players. The release of pro-inflammatory cytokines by the infected epithelium starts a cascade of responses, with circulating cells being recruited to defend the host; however, the aggravation of injury signals and considerable cell recruitment leads to unwanted effects.

The viral presence triggers the innate immune response by activating three main intracellular pathways: retinoic acid inducible gene-1 (RIG-1), toll-like receptors (TLR, mainly TLR3 and TLR7) and the inflammasome [43]. When the viral RNA binds to RIG-1, it initiates an interaction with mitochondria associated antiviral signaling (MAVS) protein that induces the production and release of type I and III interferons (IFNs) (IFNα/β and IFNλ), IL-1β and IL-18 [43]. The viral presence in the alveolus leads to epithelial injury by inducing inflammation and cell death (Figure **I-2**). Infected TLR-activated AEC2 and alveolar resident macrophages induce a chemokine response that recruits immune cells to the alveolar space [36]. Neutrophils migrate across the epithelium and release toxic mediators (proteases, reactive oxygen species – ROS – and neutrophil extracellular traps) important for host defense but responsible for endothelial and epithelial damage [47]. Bone marrow-derived macrophages are also recruited to the alveolar space and can cause injury in epithelial cells by activating cell death receptors and releasing TNF-related apoptosis-inducing ligands [48].

Upon infection, the endothelial cell barrier is disrupted after vascular endothelial cadherin (VE-cadherin) phosphorylation [36], [47]. Furthermore, influx of immune cells, neutrophil-derived mediators and inflammatory macrophages induce epithelial cell death [48]. Additionally, disruption of gap junctions to neighboring epithelial cells cause mitochondrial dysfunction and loss of the barrier integrity [36]. Endothelial and epithelial cell permeability increases and leads to hypoxemia, impaired sodium transport and reduced edema clearance (Figure **I-2**) [36].

Once exposed to injury, the alveolar cell populations re-establish homeostasis, initiating complex repair mechanisms [49]. Surviving $Axin2^{+}$ AEC2 [50], [51] proliferate and differentiate into AEC1 to replace epithelial cell loss, with proliferation being promoted by growth factors (e.g., keratinocyte growth factor – KGF, epidermal growth factor – EGF, hepatocyte growth factor – HGF and granulocyte-macrophage colony-stimulating factor – GM-CSF [52]) and activated via transcriptional pathways (WNT-β-catenin pathway and fork-head box protein M1 pathway) [36]. Other cell types, like $KRT5^{+}$ epithelial progenitors and club cells are also mobilized to differentiate into AEC2 [36].

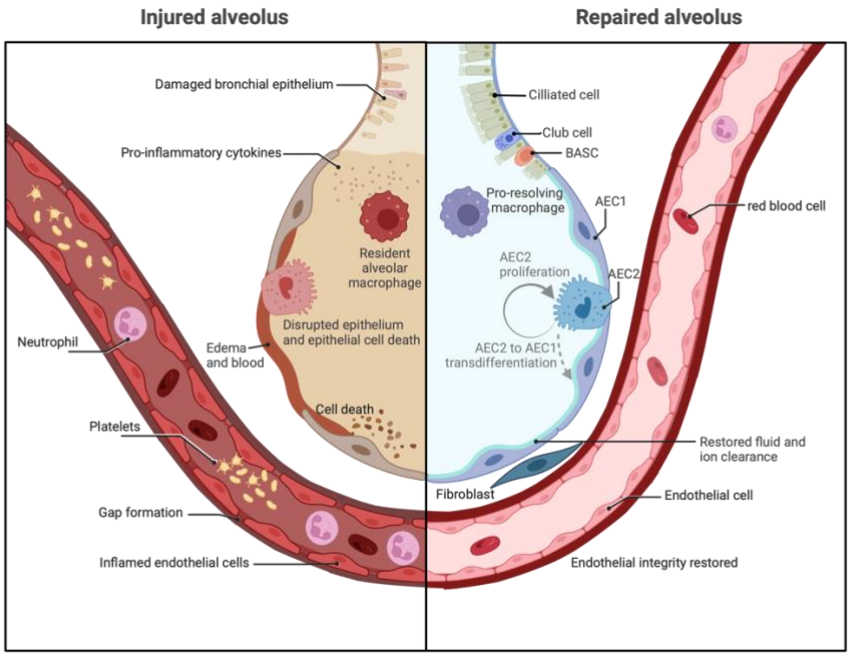

Figure I-2. Mechanisms of injury and repair in the alveolus after IAV-infection. (Left side) Injured alveolus after IAV-infection. Released pro-inflammatory cytokines activate inflammation, leading to epithelial injury and neutrophil migration. The epithelial-endothelial barrier integrity is lost, with cell death, disruption of gap junctions and impaired fluid clearance. **(Right side)** Repaired alveolus after IAV-infection. The release of factors contributes to AEC2 proliferation and differentiation into AEC1, indispensable for the restitution of the epithelial barrier. Pro-resolving macrophages eliminate dead cells and debris, helping in restoring endothelial integrity and fluid clearance. AEC1 alveolar epithelial cell type 1, AEC2 alveolar epithelial cell type 2, BASC bronchoalveolar stem cell. Adapted from M.A. Matthay *et al*, 2019 [36]. Created using BioRender.com.

Once the alveolar epithelium is regenerated and the epithelial barrier integrity is restored, pro-resolving macrophages can eliminate dead cells and debris, and edema can be cleared by AEC1 and AEC2 [36]. Unfortunately, during ARDS, some repair mechanisms are specifically inhibited. For example, IAV infects epithelial stem/progenitor cell niches, thus preventing proliferation and differentiation [53]. Molecularly, although KGF stimulates growth, it also increases AEC2 susceptibility to IAV infection in mice [54]. Moreover, the biological changes from endothelial and epithelial injury contribute to surfactant dysfunction that can increase atelectasis, and consequently rise the risk of biophysical injury [55].

Mesenchymal Stem Cells (MSC)

Origin, definition, and characteristics

Stem cells are defined as cells that can preserve themselves through self-renewal and that can differentiate into mature cells of a particular tissue [56]. Due to these abilities, stem cells have been extensively used as cell therapy for the treatment of diverse medical conditions, such as spinal cord injury, hearth failure or degenerative diseases [57]. However, each stem cell population has inherited heterogeneity as it can originate from multiple organs/tissue, can have different differentiation ability and can be sampled in diverse stages of development. [58]. Therefore, stem cells are defined based on three main properties: self-renewal, clonality and potency [59]. According to the development stage, stem cells can be classified as totipotent, pluripotent, multipotent and unipotent. In this regard, mesenchymal stem cells (MSC) are multipotent adult stem cells that can be found in multiple tissues, including umbilical cord (UC), bone marrow (BM) and adipose tissue (AT) [60].

MSC have a multi-directional differentiation potential that is affected by the organ of origin [61]. Despite being multipotent cells from a 'mesenchymal' origin rather than true stem cells, several studies involving MSC show high tissue-repair potential by demonstrating their capacity to differentiate into cells from the three germ layers (mesodermal, ectodermal, and endodermal) [61], [62]. MSC are capable of differentiating (*in vitro* and *in vivo*) into mesenchymal tissues, like osteoblasts [63], chondrocytes [64], adipocytes [65], tendons and skeletal muscle cells [66]; cardiomyocyte- and hematopoietic-supporting stroma cells [67]; ectodermal tissues, as skin [68] and neurons [69]; and endodermal tissues, including lung [70], hepatocytes [71], pancreatic β-cells [72] and endothelial cells [73]. Because of the rapidly expanding information and published data, unifying the definition of the basic characteristics of MSC was required. Although MSC isolation and identification relies on morphology, adherence to plastic, and a combination of surface markers, there is no cell expression marker unique to MSC [74]. According to the International Society for Cellular Therapy (ISCT), human MSC should follow three minimal criteria: (1) must be plastic adherent, (2) express CD105, CD90, CD73 and CD44, and lack the expression of CD45 (pan-leukocyte marker), CD34 (primitive hematopoietic progenitors and endothelial cells), CD14 and CD11b (prominently expressed on monocytes and macrophages), CD79 and CD19 (B cells) and HLA-DR (major histocompatibility complex (MHC) class II surface receptor) molecules such as CD80 (B7-1), CD86 (B7-2), or CD40, and (3) must be able to differentiate into osteoblasts, adipocytes and chondroblasts *in vitro* [75], [76]. In 2007, Chamberlain *et al.* mentioned that MSC also express CD44, CD71, CD117, and Stro-1, as well as the adhesion molecule CD106

(vascular cell adhesion molecule [VCAM]-1), CD166 (activated-leukocyte cell adhesion molecule), intercellular adhesion molecule (ICAM)-1, and CD29 [77]. The ISCT definition was precise enough to combine most of the existing knowledge at that time; yet, more recently, it has been suggested that MSC are biologically more contradictory, with different sources of these cells exhibiting different gene expression profiles, proliferation rates, differentiation potential, and functional properties [78], [79].

Fetal and adult stem cells have different therapeutic potential, with adult sources presenting higher population homogeneity [80]. BM is the most studied source of MSC, with BM stromal cells being present in trabecular (spongy) bones [81]. Due to their accessibility, expandability, and multipotent nature, BM-derived MSC (BM-MSC) hold significant promise for application in tissue engineering and regenerative medicine [82]. The selection of an ideal source of MSC for a specific therapeutic use should be critically evaluated and compared with other potential sources as their functional properties (e.g., differentiation potential, immunomodulation, secretion of bioactive factors), tissue availability and cell proliferation capacity may differ [79].

To date, BM-MSC have been successfully isolated from several animal species but there are significant differences since known human markers are, at times, different/absent in mice. BM-MSC from C57BL/6 mouse do not express CD90, contrary to human [83]. Furthermore, BM-MSC from C57BL/6 mice are positive for Sca-1, but BALB/c mice are negative, indicating a heterogeneity within mouse strains [83]. Despite these challenges, Matsuzaki *et al.* found a way to simplify murine BM-MSC isolation by combining a double positive selection of the markers PDGFRα and Sca-1 [84]–[87].

Proliferation, multipotency, trophic ability and homing are some of the essential properties inherent to the therapeutic abilities of MSC [88]. When in culture, MSC proliferation is tightly regulated by a low activity of Wnt/ß-Catenin signaling [89]. *In vivo*, the expression of cell cycle genes is modulated by the hypoxia-inducible factor 1, present under hypoxic conditions (oxygen levels lower than 10%) and is essential to protect the mitochondria from the oxidative metabolism [90]. After isolation and successful expansion, the final assessment for MSC characterization is their ability to differentiate *in vitro*. To promote adipogenic differentiation, confluent cultures are incubated with dexamethasone, insulin, isobutyl methylxanthine, and indomethacin [91]. Accumulation of lipid-rich vacuoles within the cells that can be assayed histologically by oil red O staining [92]. Chondrocyte formation occurs when a cell-pelleted-micromass is cultured in the presence of transforming growth factor-β1 or -β3 (TGF-β1 or -β3) and/or insulin-like growth factor 1 (IGF-1), FGF-2, or BMP-2 [93], [94]. After weeks, the

cell pellet develops a multi-layered morphology, with a strong staining with toluidine blue or Alcian blue, indicating an abundance of glycosaminoglycans within the extracellular matrix, concordant to chondrocytes [95], [96]. To generate osteoblasts *in vitro,* a confluent monolayer of MSC is incubated with ascorbic acid, β-glycerophosphate, vitamin D3 and/or BMP-2, -4, -6 and -7, leading to increased expression of alkaline phosphatase and calcium deposits (bone nodules) that stain positive for alizarin red and *von Kossa* [97], [98].

MSC trophic function is vast and characterized by the production of growth factors (such as platelet-derived growth factor [PDGF], macrophage-colony stimulating factor (M-CSF), granulocyte- colony stimulating factor, erythropoietin, angiopoietin 1 [Ang-1]), chemokines (C-X-C motif chemokine ligand [CXCL] 12 and C-C motif ligand 5 [CCL5]), IL-3 and IL-6 and extracellular matrix molecules (hyaluronans) [99], [100]. Besides sustaining homeostasis, MSC trophic function might also be beneficial for tissue healing and regeneration, with pre-clinical studies concluding that adoptive transfer of MSC in COPD patients improved lung function and slowed down pathological degeneration [101].

MSC homing and migration involves chemotaxis, rolling/adhesion diapedesis, and interstitial migration, allowing cells to travel blood vessels, cross endothelial walls and reach damaged tissues, with the production of metalloproteins being crucial for MSC trafficking [102]. MSC used in therapies can be injected topically, directly in damaged tissues, or systemically, travelling via peripheral blood. When delivered locally, MSC do not depend on homing/migration and avoid physical barriers whereas systemic injections entail movement to reach damaged tissue, that might result in reduced MSC cell number reaching the local and loss of function [103]–[105].

Immunomodulatory properties

The therapeutic effects of MSC are largely related to their secretion of soluble factors that contribute to microenvironment change and promote tissue repair, making these cells the "guardians of inflammation" [91]. While MHC expression on all cells allow the immune system to distinguish self from non-self, MSC express low levels of the immunogenic surface antigens (MHC I and MHC II) and share surface markers with the thymic epithelium. Additionally, MSC express adhesion molecules that are essential for T-cell interaction, including VCAM-1, ICAM-2 and lymphocyte function-associated antigen III [105], [106]. This characteristic of MSC is clinically important since it is possible to transplant these cells from an allogeneic host without the need for additional immunosuppression [107].

MSC can sense danger signals through TLRs that recognize molecules from injured cells or pathogens – TLR2, TLR3, TLR4, TLR7 and TLR9 [108]. After recognition, MSC specifically respond to TLRs, e.g., TLR3 activation induces an anti-inflammatory phenotype while TLR4 activation will shift MSC to act more pro-inflammatory [109]. Pro-inflammatory MSC are only active when low levels of inflammatory signals (TNF-α and IFN-λ) are present, can activate T-cells and recruit more lymphocytes by secreting macrophage inflammatory protein 1 (MIP-1), CCL5, CXCL9 and CXCL10 [110]. Yet, when the levels of inflammation signals increase, MSC secrete inducible nitric oxide synthase (iNOS) (in case of mice) and indoleamine 2,3 dioxygenase (IDO) (in humans) leading to the inhibition of T-cell proliferation and changing to an anti-inflammatory phenotype [111]. Clearly, there is a significant difference between quiescent MSC that can promote an immune response with low levels of inflammation and activated MSC that suppress the immune response (Figure **I-3**). Quiescent MSC produce TGF-β and IL-10 that, when over-stimulated with pro-inflammatory factors like IFN-γ, IL-1β and TNF-α [112] change MSC into an activated stage that will eventually lead to the release of immune suppressors such as PD-L1 and PD-L2 (programmed cell death ligands 1 and 2), IDO or iNOS, prostaglandin E_2 (PGE2), TGF-β, IL-10, HGF and CCL2 [113].

The immunosuppressive nature of MSC not only depends on their activation but also on tight regulation from immune cells, including T-cells, natural killer (NK) cells, dendritic cells (DCs), B-cells, neutrophils, monocytes, and macrophages (Figure **I-3**) [60]. Most MSC-mediated immunosuppression on activated T-cells has been attributed to the secretion of anti-proliferative soluble factors, such as TGF-β, HGF, PGE2, IDO (essential factor for lymphocyte proliferation), and IL-10 [114]. It has also been reported that MSC are able to suppress NK cell proliferation after stimulation with IL-2 or IL-15 [115] and can interfere with the differentiation, maturation, and function of DCs [116]. Human MSC have also been demonstrated to suppress the proliferation of B-cells activated with anti-Ig antibodies, soluble CD40 ligand and cytokines, as well as to interfere with differentiation, antibody production and chemotactic behavior of B lymphocytes [117].

Release of cytokines promoting tissue repair is one the major advantages in the therapeutic application of MSC. Once in contact with an injured microenvironment, MSC release growth factors that additionally stimulate repair mechanisms in endothelial, epithelial, and local tissue stem/progenitor cells [118], [119]. Some of those factors include EGF, FGF, PDGF, TGF-β, vascular endothelial growth factor (VEGF), HGF, IGF-1, and stromal cell-derived factor-1 [120].

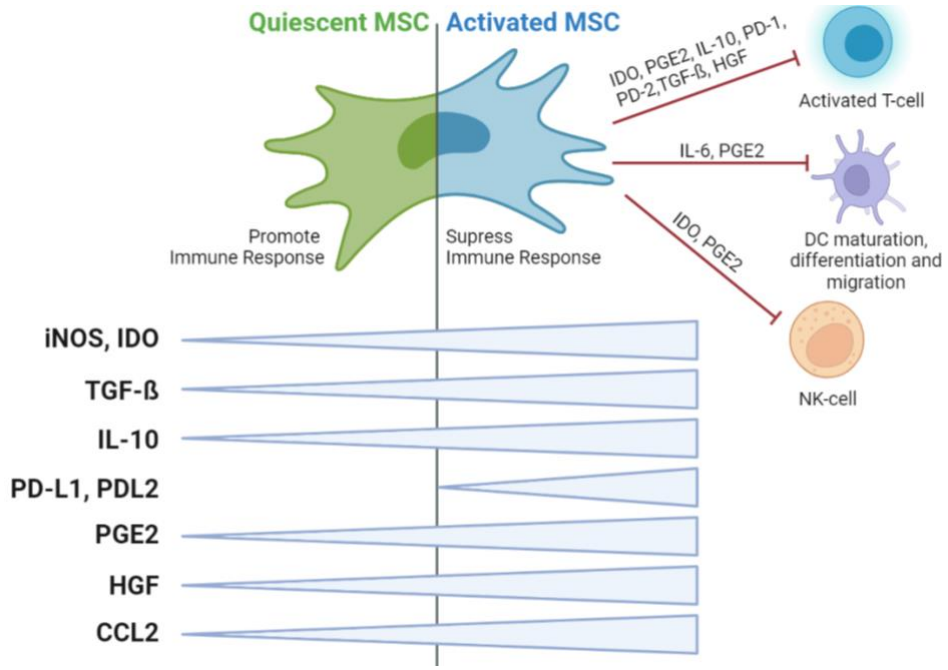

Figure I-3. Immune modulators and immune suppressive potential of MSC. MSC express immune modulators both in quiescent and activated states. Some modulators are expressed in basal concentrations on the quiescent state but are upregulated upon activation – iNOS or IDO, TGF-β, IL-10, PGE2, HGF and CCL2. PD-L1 and PD-L2 are only expressed in the activated state. All modulators are upregulated by pro-inflammatory factors in the concentration-dependent manner. In the activated state, MSC have immunosuppressive potential, that can directly impact the proliferation and inhibition of T-cells, NK-cells, and DC, among others. The soluble factors released by MSC that play a key role in these effects are IDO, PGE2, IL-10 and IL-6, PD-1 and -2, TGF-β and HGF. CCL2 C-C motif chemokine ligand 2, DC dendritic cells, HGF hepatocyte growth factor, IDO indoleamine 2,3-dioxygenase, IL-10 interleukin-10, IL-6 interleukin-6, iNOS inducible nitric oxide synthase, MSC mesenchymal stem cells, NK-cell natural killer cell, PD-L1 and PD-L2 programmed cell death ligands 1 and 2, PGE2 prostaglandin E2, TGF-β transforming growth factor beta. Adapted from W. Jiang et al. 2019 [113], Q.Zhao *et al.* 2016 [60] and F. van den Akker *et al.* 2013 [105]. Created using BioRender.com.

MSC as a promising therapy for ARDS

The immunosuppressive, anti-inflammatory, anti-microbial, and regenerative characteristics of MSC have made it possible to consider them as a cell therapy for the treatment or prevention of numerous disorders, diseases or injuries, such as sepsis, diabetes, graft-versus-host disease, acute myocardial infarction, hepatic failure, amyotrophic lateral sclerosis, COPD, spinal cord injury and Crohn's disease [121], [122].

In the past years, the number of clinical trials using MSC has exponentially grown, and even though available data supports safety of MSC therapy with both autologous and allogeneic cells, results on cell efficacy are often just preliminary [123]. A closer look at the active and completed trials suggest that BM aspirates are the most frequent source of MSC [124]. Regarding cell delivery, intravenous application is the most used route throughout clinical trials. Nevertheless, this present major drawbacks on the treatment efficacy, since the vast majority of MSC can modulate inflammation systemically and get trapped before reaching

the lungs [125]. A more targeted approach would be to rely on localized applications to surpass the lung barrier [126].

From a total of 4623 active and completed MSC-related clinical trials (as of February 2023, www.clinicaltrials.gov), 25 studies claim the use of MSC for ALI/ARDS treatment. Notably, despite years of research and medical care advances, there is still no available drug for ARDS with only a few treatment options including lung-protective ventilation, prone-positioning and conservative fluid strategies [47]. To test the specificity of MSC in the treatment of ARDS, several research groups focused their investigation in MSC capability to reduce lung injury severity [127] including MSC's ability to (1) support tissue repair, (2) release anti-inflammatory cytokines, (3) diminish lung endothelial and alveolar epithelial permeability, (4) promote alveolar fluid clearance and (5) reduce cell apoptosis [122]. Overall, MSC paracrine activity, release of extracellular vesicles, mitochondrial transfer or cell-to-cell contact, and tissue integration represent the hallmarks for MSC therapeutic potential in clinical trials (Figure **I-4**).

In pre-clinical data from bacterial-derived ARDS, BM-MSC treatment of mice infected with *Escherichia coli (E. coli)* resulted in faster lung recovery and enhanced bacterial clearance [128], [129], by modulating release of anti-inflammatory cytokines (interleukin 1 receptor antagonist – IL1-ra – and IL-13) [130]. Bacterial clearance was also related to reduced monocyte apoptosis through AKT phosphorylation that related to the secretion of KGF by MSC [131]. The interaction between MSC and immune cells in this model was found to occur via IL-6 production by MSC, improving neutrophils recruitment [132], as well as mitochondria transfer from MSC to macrophages [133], with consequent rise of their phagocytic capacities. Moreover, in human *ex-vivo* perfused models, using *E. coli* endotoxin-induced lung injury, the administration of human BM-MSC (or just BM-MSC-derived conditioned media) showed a decrease in lung endothelial injury and restored alveolar fluid clearance to levels compared to homeostatic lungs [134]. In bleomycin-injured mice, TNF-α stimulated tumor necrosis factor inducible gene 6 (TSG-6), an inflammatory protein produced by MSC, was essential for mice survival following bleomycin [135].

Lipopolysaccharide (LPS)-induced lung injury resolution by conditioned media from murine BM-MSC was directly related with high IGF-1 concentrations that promoted an anti-inflammatory macrophage phenotype [136]. Also, in an LPS-injury model, human MSC expressing a pro-resolving lipid mediator, lipoxin A4, increased mice survival and decreased production of TNF-α and MIP-2 in bronchoalveolar lavage fluid [137].

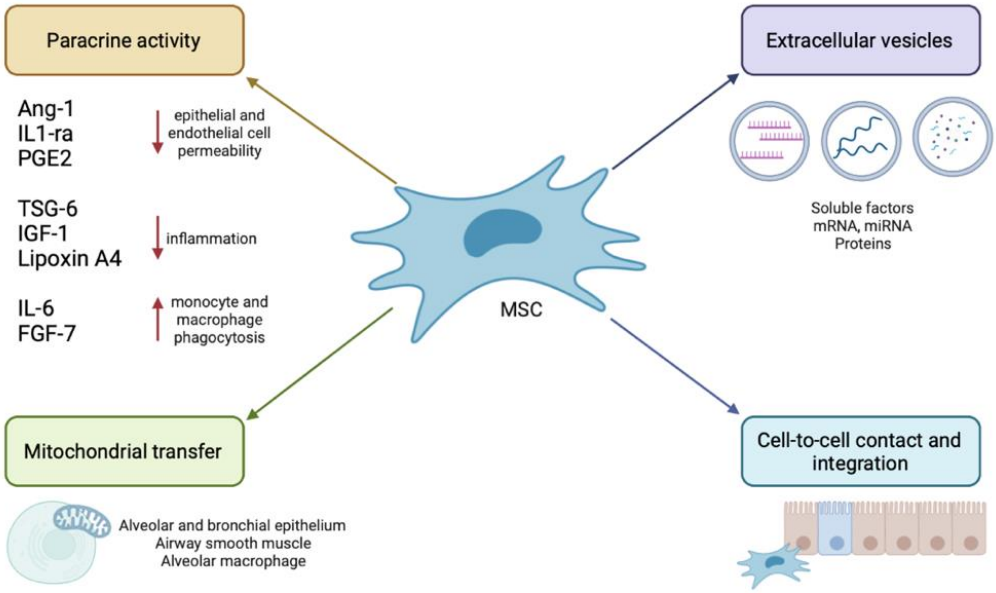

Figure I-4. MSC therapeutic potential in ARDS. The beneficial effects of MSC in the context of ARDS include their production of paracrine factors, mitochondrial transfer, release of extracellular vesicles, cell-to-cell contact, and integration with the damages tissue. The secretion of Ang-1, IL1-ra and PGE2 by MSC can decrease epithelial and endothelial cell permeability, while release of TSG-6, IGF-1 and Lipoxin A4 (and IL1-ra) reduces inflammation. Monocyte and macrophage phagocytosis is increased by MSC production of IL-6 and FGF-7 (also contributes for improving alveolar fluid clearance). Extracellular vesicles from MSC containing genetic information (mRNA and miRNA), soluble factors and proteins also contribute to tissue repair. Mitochondria are efficiently transfer from MSC to alveolar and bronchial epithelium, airway smooth muscle cells and alveolar macrophages by overexpression of Miro1. Lastly, MSC can physically communicate with the damaged tissue, differentiate, and effectively integrate in the host. Ang-1 angiopoietin 1, FGF-7 fibroblast growth factor 7, IGF-1 insulin-like growth factor 1, IL1-ra interleukin 1 receptor antagonist, IL-6 interleukin 6, mRNA messenger ribonucleic acid, miRNA micro ribonucleic acid, MSC mesenchymal stem cells, PGE2 prostaglandin E_2, TSG-6 tumor necrosis factor-inducible gene 6 protein. Adapted from C. Li *et al.*, 2019 [138], L.A. Huppert *et al.*, 2019 [122], S.C. Abreu *et al.*, 2016 [139] and X.L Fan *et al.*, 2020 [140]. Created using BioRender.com.

MSC paracrine cytokine release also improves lung endothelial and epithelial permeability, usually damaged upon ARDS [141]. Ang-1 secretion by MSC is thought to restore protein permeability of injured AEC2 to basal levels, while IL1-ra and PGE2 are associated with restoring epithelial permeability after inflammation and hypoxia [142]. FGF-7 release by MSC is associated with edema resolution after FGF-7 depleted BM-MSC conditioned media failed to increase transepithelial sodium transport by decreasing the apical expression of the epithelial sodium channel (typically high during ARDS) [142]. MSC secretion of anti-apoptotic factors like VEGF, IGF-1, TGF-β and GM-CSF is also linked to repair mechanisms after lung injury[143].

As stated before, MSC transfer mitochondrial deoxyribonucleic acid (DNA), not only to macrophages [144] but also to damaged alveolar epithelial cells, reestablishing AEC2 surfactant production [145]. A possible transfer mechanism is thought to involve the formation of intercellular cytoplasmatic bridges [146]. MSC differentiate, as described before,

and can successfully integrate, although at very low rates, in damaged tissue to either replace damaged cells [147] or re-establish tissue function [148].

Extracellular vesicles (EVs) have been thought to play also a critical role in making MSC reliable therapeutic candidates [139]. EVs are formed by budding of multivesicular bodies to the cell membrane and contain RNA, micro-RNA (miRNA), proteins and lipids [122]. Multiple studies revealed that microvesicles reduce inflammation and alveolar edema [149], alter macrophage function [150], increase alveolar fluid clearance and reduce bacterial load [151].

Even though MSC are promising candidates for ARDS future treatments, using MSC as a cell therapy still carries challenges. Not only is it necessary to fully understand MSC's mechanisms that contribute to improved disease outcomes, but it is also essential to standardize quality and cell preparation, especially given the heterogeneity present in both MSC populations and ARDS phenotypes.

II. Aims

MSC show promising therapeutic potential in different forms of acute lung injury, particularly in virus-induced ARDS. However, the molecular mechanisms by which MSC treatment can drive epithelial repair during lung infections are not yet fully understood. Therefore, this study was focused on:

(1) Understanding BM-MSC response towards viral infection *in vitro* and how BM-MSC modulate infected AEC outcome, also in comparison with the lung resident mesenchyme.
(2) Analyzing how pre-conditioning could improve the alveolarization capacity of BM-MSC to generate lung organoids, elucidating what factors are necessary to drive activation.
(3) Using BM-MSC as a cell treatment for influenza-infected mice and, upon cell recovery, studying how BM-MSC gene expression profile changes with viral exposure, to better understand the molecular mechanisms behind their pro-resolving phenotype.
(4) Elucidating the molecular crosstalk between BM-MSC and the injured epithelium to identify therapeutic targets.

III. Materials and Methods

Mice strains, harbouring and scoring

Wildtype (WT) C57BL/6-N mice were obtained from Charles River Laboratories. From Jackson Laboratories, B6.129(Cg)-Gt(ROSA)26Sor$^{tm4(ACTB-tdTomato,-EGFP)Luo}$/J (mT/mG) mice were used. Type I IFN receptor (IFNAR) deficient mice (IFNAR$^{-/-}$) were provided by U. Kalinke (Paul-Ehrlich Institute, Langen, Germany) [152].

Mice used for organ retrieving (WT, mT/mG and IFNAR$^{-/-}$) were 8-10 weeks old and housed under specific pathogen-free conditions at the Justus-Liebig University of Gießen, Germany. WT mice (10-12 weeks old and average weight of 20 g) *in vivo* experiments were performed in Justus-Liebig University of Gießen and monitored up to 3 times a day, following the approved daily scoring criteria (Table III-1). IFNAR$^{-/-}$ mice (10-12 weeks old and average weight of 20 g) *in vivo* experiments were performed in cooperation with IBioBA-MPSP (Instituto de Investigación en Biomedicina de Buenos Aires – Parter Institute of the Max Planck Society), under specific pathogen-free conditions, and monitored up to 3 times a day, following the approved daily-scoring criteria (Table III-1).

Mice daily-scoring was developed and approved according to the following criteria: weight loss, general condition, spontaneous behavior, and trial specific conditions (Table III-1). Mice were suggested to be unburdened if they would score 0, determined to suffer from low stress levels and thus checked daily with a 5-9 score; scoring 10-19 points would define moderate stress level and result in twice a day check-up; and 20 or higher scoring would result in severe distress for the mice, with euthanasia being necessary. Termination was directly allowed if mice (1) scored parameters were equal or higher than 20, (2) presented significantly cyanotic mucous membranes, (3) gasped, (4) showed apathy and immobility, (5) indicated extremely low skin temperature, (6) loss more than 25% of their body weight within 3 consecutive days, (7) did not increase body weight 24 h after 5% glucose administration, and (8) showed moderate stress for more than 5 days.

Table III-1. Scoring criteria approved for *in vivo* experiments.

Criteria	Score and criteria description
Weight loss	0, unaffected or increased weight 10, weight reduction higher than 10% in 2 days 15, weight reduction higher than 20% in 2 days (additional measure: administration of 100 microliters (µl) of 5% glucose) 20, weight reduction higher than 25% in 3 days
General condition	0, smooth and shiny coat with shiny eyes and clean orifices 5, dull fur and cloudy eyes 10, dull fur, sunken and cloudy eyes, and moist body orifices

	20, ruffled fur, low body temperature, closed eyes, convulsions, paralysis and breathing noises
Spontaneous behavior	0, attentive, curious, straightening up and quick movements 5, unusual behavior, limited movements or overactivity, reduced exploratory behaviors 10, isolation, apathy, coordination disorder, hyperkinetic 20, automutilation, necrosis
Trial specific	5, shortness of breath or rapid breathing 10, visible chest breathing with reduced respiratory rate 20, bluish mucous membranes

Influenza-A virus (IAV) strains

A/Puerto Rico/8/1934 H1N1 (PR8) mouse adapted influenza A virus was used for all experiments, unless specified otherwise. The virus stock was propagated on Madin Darby Canine Kidney II (MDCK II) cells and virus titers were regularly checked. For organoid infection, SC35M-Cre (IAV-Cre) virus was also used [153].

Flow Activated Cell Sorting (FACS)

Primary cell populations were flow-sorted using BD FACSAria III™ Cell sorter with the 85 micrometers (μm) nozzle, running on BD FACSDiva™ Software. For cell population analysis, samples were run on BD LSRFortessa™ Flow cytometer (with BD FACSDiva™ Software). All the following analysis were carried out employing BD FlowJo software (version 10). Antibodies used for cell sorting or cell analysis are mentioned in the respective experiments.

Isolation and culture of primary cells and cell lines

Primary AEC

Murine AEC were isolated based on the protocol developed by Corti *et al.* [154] with modifications made by Herold *et al.* [155]. Mice were sacrificed by cervical dislocation, while under isoflurane anesthesia. The lung was filled with 1.5 milliliters (ml) of sterile dispase to allow enzymatic separation of distal epithelial cells. The lungs and trachea were dissected out, washed in phosphate buffer saline (PBS), and placed in dispase for 40 minutes (min) at room temperature (RT). The heart, trachea and large airways were removed, and the remaining lung tissue was dissociated in Dulbecco's Modified Eagle's Medium (DMEM) supplemented with 2.5% N-(2-Hydroxyethyl)piperazine-N′-(2-ethanesulfonic acid) (HEPES) and 0.01% DNase I in MACS C-tubes, using the gentle MACS dissociator. Cells were filtered through 100 μm, 40 μm and 20 μm cell filters, centrifuged (500 relative centrifugal force – xg – for 10 min),

resuspended in DMEM-2.5% HEPES and counted. The cell suspension was incubated with biotinylated-rat anti-mouse CD31, CD16/32 and CD45 antibodies for 30 min at 37 Celsius (°C) to remove residual leukocytes and endothelial cells. Calculated antibody volumes are present on Table III-2. After incubation, the cell suspension was centrifuged (500 xg for 10 min) and resuspended in the calculated dilution volume (Table III-2). Previously washed biotin-linked magnetic beads (volume calculated using Table III-2) were added to the cell suspension for 30 min at RT with gentle rocking. After incubation, magnetic separation was performed for 15 min and the remaining cells were centrifuged (500 xg for 10 min) and resuspended with DMEM supplemented with 10% fetal bovine serum (FBS) and 1% penicillin/streptomycin/L-glutamine (Pen/Strep/L-Glu) (AEC media). Cell suspensions with a purity ≥ 90% were seeded and used for further experiments.

Table III-2. Antibodies, media volume and biotinylated beads calculations for AEC isolation.

Cell number: $\frac{\text{counted cell number}}{1\times10^6}$		
Biotinylated rat anti-mouse CD45 (BD Bioscience)	Antibody volume (µl)	cell number × 0.9
Biotinylated rat anti-mouse CD16/32 (BD Bioscience)		cell number × 0.675
Biotinylated rat anti-mouse CD31 (BD Bioscience)		cell number × 0.4
	Dilution volume (ml)	$\frac{\text{cell number} \times 0.675}{3}$
	Magnetic beads volume (µl)	dilution volume (ml) × 50

Lung-derived mesenchymal stem cells (lung-MSC)

Lung-MSC from either WT or genetically modified mice were isolated, following AEC isolation protocol. After excluding endothelial and lymphoid cells, the remaining cell suspension was stained according to Table III-3 for 15 min at 4 °C. Next, the stained cell suspension was centrifuged (500 xg for 10 min) and resuspended in PBS supplemented with 7.4% ethylenediamine tetraacetic acid (EDTA) and 0.5% FBS (final pH of 7.2) (sorting buffer). Live/dead staining (SYTOX™) was added before sorting. Lung-MSC were isolated based on live/dead staining, negative expression of CD31, CD45 and EpCAM and positive expression of Sca-1 and PDGFRα.

Table III-3. Staining antibodies and respective dilutions for lung-MSC isolation with FACS.

Antibody	Clone	Fluorochrome	Dilution	Manufacturer
CD31	390	Alexa Fluor 488	1:50	Biolegend
CD45	30-F11	FITC	1:50	BD Biosciences
EpCAM (CD326)	G8.8	APC-Cy7	1:50	Biolegend
PDGFRα	APA5	APC	1:50	Biolegend
SYTOX™	-	PB	1:1000	Thermo Fisher Scientific
Sca-1 (Ly-6A/E)	D7	PE	1:50	Biolegend

BM-MSC

BM-MSC from either WT mice or genetically modified mice were isolated according to manufacturer's instructions (MesenCult™ Expansion Kit Mouse). Mice were sacrificed by cervical dislocation while under isoflurane anesthesia and femurs and tibias were removed. The bones were cleaned from muscle tissue and kept on ice in PBS supplemented with 2% FBS and 1 millimolar (mM) EDTA. Both bones' ends were cut, allowing the exposure of the marrow shaft. Using a 6 ml syringe with a 23-gauge needle, 37 ºC MesenCult™ Basal Medium Mouse (MSC basal media) supplemented with 10% MesenCult™ 10X Supplement Mouse (complete MSC media) was flushed inside the bones. The bone marrow recovered was placed in a conical tube and this process was repeated until the bones appear white. The cell suspension was filtered (70 μm) and centrifuged for 10 min at 300 xg. The supernatant was discarded, and the pellet resuspended in complete MSC media. The cells were plated and monitored every day for 5-7 days. After reaching confluency, the cells were trypsinized (Stem-Pro® Accutase®) and flow sorted according to BM-MSC expression profile – negative for CD31, CD45 and Ter119 and positive for Sca-1 and PDGFRα. Antibody dilutions are present in Table III-4. After cell sorting, the pure cell population without contaminant cells was seeded for expansion and incubated at 37 °C, 5% carbon dioxide (CO_2), using MSC complete media that was changed every 2-3 days.

Due to a high demand of cell numbers, BM-MSC were passaged and frozen for a maximum of 10-12 passages. The freezing media was prepared by diluting 1:10 of dimethylsulfoxid (DMSO) in MSC basal media and cells were frozen in a concentration of $1x10^6$ cells/ml at -80 °C. For thawing, triple the volume of warm MSC media was added until the frozen cell suspension melted. The cells were centrifuged for 10 min at 500 xg and seeded as required. After cell manipulation, an aliquot of the passaged cells was tested for phenotype confirmation and differentiation capacity (see Routine experiments).

Table III-4. Staining antibodies and respective dilutions for BM-MSC isolation with FACS.

Antibody	Clone	Fluorochrome	Dilution	Manufacturer
CD31	390	Alexa Fluor 488	1:50	Biolegend
CD45	30-F11	FITC	1:50	BD Biosciences
PDGFRα	APA5	APC	1:50	Biolegend
Sca-1 (Ly-6A/E)	D7	PB	1:50	Biolegend
SYTOX™	-	PB	1:1000	Thermo Fisher Scientific
Ter119	TER-119	FITC	1:50	Biolegend

3T3 cell line

A NIH/3T3 mouse fibroblast cell line (ATCC) was used for *in vivo* experiments. The cell line was thawed and propagated according to the manufacturer's instructions, using ATCC-DMEM supplemented with 10% bovine calf serum. Seeded cells were incubated at 37 °C, 5% CO_2, and expanded and used until passage 5-6.

Routine experiments

The following described protocols were performed routinely to verify cell viability and virus efficiency.

BM-MSC phenotype and differentiation ability

BM-MSC were characterized often to ensure their agreement with ISCT criteria [74]. To examine BM-MSC surface antigen expression, the cells were stained with the anti-mouse antibodies CD11b, CD19, CD31, CD34, CD44, CD45, CD105, CD117, Sca-1 and PDGRFα with the dilutions present in Table III-5.

Table III-5. Staining antibodies and respective dilutions for BM-MSC characterization in flow cytometry.

Antibody	Clone	Fluorochrome	Dilution	Manufacturer
CD11b	M1/70	PB	1:200	Biolegend
CD19	1D3/CD19	APC	1:100	Biolegend
CD31	390	AlexaFluor 488	1:50	Biolegend
CD34	MEC14.7	PE-Cy7	1:50	Biolegend
CD44	IM7	APC-Cy7	1:10	Biolegend
CD45	30-F11	FITC	1:50	BD Biosciences
CD105	MJ7/18	APC	1:50	Biolegend
CD117 (c-kit)	2B8	PE	1:50	Biolegend
PDGFRα	APA5	APC	1:50	Biolegend
Sca-1 (Ly-6A/E)	D7	PB	1:50	Biolegend

To test their differentiation capacity, BM-MSC were seeded and manipulated according to manufacturer's instructions – MesenCult™ Osteogenic Stimulatory Kit Mouse, MesenCult™ Adipogenic Stimulatory Kit Mouse, and MesenCult™-ACF Chondrogenic Differentiation Kit.

For osteogenic differentiation, BM-MSC were cultured with MSC full media at a density of 50 000 cells per centimeter square (cm^2) and let to expand until 80-90% confluency. MSC full media was substituted for MesenCult™ MSC Basal Media Mouse supplemented with 20% MesenCult™ Osteogenic Stimulatory Supplement Mouse (complete osteogenic media). Complete osteogenic media was changed every 3 days, for a total of 21 days of stimulation. At day 21, the differentiated cell layer was washed with PBS and fixed for 30 min with Saccomano Fixation Solution. Following fixation, the cells were washed with distilled water

(dH_2O) and covered in Alizarin Red S for 15 min (at RT, in the dark). The staining solution was removed and washed with dH_2O. BM-MSC derived osteoblasts were microscopically observed, with extracellular calcium deposits being orange red.

BM-MSC underwent adipogenic differentiation after cultured at 1 000 cells/cm^2 density in MSC complete media. After reaching 90% confluency, MSC full media was replaced for MesenCult™ MSC Basal Media Mouse supplemented with 10% MesenCult™ Adipogenic Differentiation 10X Supplement Mouse and 0.1% of L-Glutamine (complete adipogenic media). Complete adipogenic media was changed every 3 days for a total of 7 days of stimulation. After complete differentiation, the cell layer was fixed for 1 hour (h) with 10% formalin, washed with water and incubated for 5 min with 60% isopropanol. Next, after the cells were washed, Oil Red O solution was added for 20 min and hematoxylin for 1 min. All the stain was washed away with water and red lipid droplets (and blue nuclei) were observed under a microscope.

To test if BM-MSC can turn into cartilage, $2x10^6$ cells resuspended in 2 ml of MesenCult™-ACF Chondrogenic Differentiation Basal Medium supplemented with 0.05% MesenCult™-ACF Chondrogenic Differentiation 20X Supplement and 2 mM L-Glutamine (complete chondrogenic media) were distributed into 15 ml polypropylene tubes. The cell suspension was centrifuged at 300 xg for 10 min. The resulting pellet and supernatant were incubated for 3 days with the tube's cap unscrewed. At day 3 of differentiation, 0.5 ml of complete chondrogenic media was added. From day 6 to day 21, exhausted media was replaced by fresh media. The newly formed cartilage spheroids were washed with PBS, fixed with Saccomano Fixation Solution for 3 h (at RT) and stained with Alcian Blue for 45 min (at RT, in the dark). The stain was carefully washed, and a de-staining solution (100 ml methanol, 100 ml acetic acid and 800 ml of water) was added for 10 min. After removal, the cartilage spheroids were embedded in glycerin (Tissue Tek®) and frozen at -80 °C until 10 µm slices were cut (Leica CM1850 UV) and placed in microscopy slides for visualization.

Virus titration assay

Before infection, MDCK II cells were seeded in 96 well-plates and cultured at 37 °C, 5% CO_2. On infection day, the cell layer was infected using cell culture supernatants for 1 h at 37 °C, with 10-fold sequential dilution steps. Pre-warmed Avicel medium (Minimum Essential Media – MEM – supplemented with 0.12% bovine serum albumin (30%) – BSA, 1% Pen/Strep, 50% Avicel®, 1% diethylaminoethyl (DEAE)-Dextran and 4% sodium

bicarbonate) supplemented with 1 μg/ml trypsin was added and plates were incubated at 37 °C, 5% CO_2 for 36 h.

After incubation time, Avicel overlay was removed, and the cells were washed with PBS and fixed (PBS supplemented with 10% paraformaldehyde – PFA – and 1% Triton X-100) for 30 min at RT. Staining for viral proteins was done using a monoclonal antibody against Influenza A virus (anti NP-antibody) (Abcam) diluted 1:100 in PBS with 3% BSA and a mouse anti-mouse HRP antibody (SantaCruz) diluted 1:1000 in PBS with 3% BSA. Cells were washed with PBS supplemented with 0.05% Tween-20 and incubated with mouse anti-NP antibody for a minimum of 60 min at RT. The primary stain was washed and the secondary stain with goat HRP antibody (Abcam) was added for 60 min at RT. NP staining was visualized using TrueBlue™ peroxidase substrate, added for up to 45 min. Cells were washed with dH_2O to stop the reaction. Stained plaques were counted, and virus titration was accessed.

In-vitro experiments

AEC infection

Primary isolated AEC (see Isolation and culture of primary cells and cell lines) were cultured in AEC media either in transwell (12-well plates) or in 12-24 well plates for 5 days, until 70-80% confluency. Unless specified otherwise, a multiplicity of infection (MOI) of 0.1 was used to infect the AEC monolayer. The virus inoculum was prepared by diluting the virus (PR8) stock solution in PBS supplemented with 0.2% of BSA and added to the washed cells for 1 h, at 37 °C and 5% CO_2. Cells were then washed with PBS and submerged in DMEM supplemented with 1% Pen/Strep/L-Glu, 0.1% BSA and 0.001% trypsin-TPCK. Infected cells were kept at 37 °C, 5% CO_2 for 24 h or 48 h until further analysis.

MSC co-cultured with AEC

Following the isolation protocol (see Isolation and culture of primary cells and cell lines), AEC were seeded with AEC media on transwell inserts at density of $1.6x10^5$ cells/well for 5 days. Meanwhile, 3 days before infection, MSC were seeded in complete MSC media at a $6x10^4$ cells/well density in 12 well-plates. MSC from either lung or BM (WT or $IRNAR^{-/-}$) origin were used. At confluency, AEC were infected with PR8, 0.1 MOI, for 1 h, following the protocol previously described. The transwell containing mock and infected AEC were combined with 80-90% confluent MSC. The co-cultured AEC were analyzed after 24 h or 48 h post infection by flow cytometry.

Cell proliferation, infection, and viability assays

Following co-culture, the mock or infected AEC were washed and detached with trypsin-EDTA at 37 °C, for 10 min. The cell suspension was distributed for negative, isotype and stained samples, in 1.5 ml vials, and centrifuged at 1000 xg for 5 min at 4 °C. To determine proliferation and infection efficiency, the cell pellet was resuspended in 150 microliters (µl) of diluted permeabilization/fixation buffer (eBioscience™ Foxp3/Transcription Factor Staining Buffer Set) and incubated for 30 min at RT. 100 µl of permeabilization/wash buffer (eBioscience™ Foxp3/Transcription Factor Staining Buffer Set) was added after the incubation period and the cell suspension centrifuged at 1000 xg for 5 min at 4 °C. The supernatant was discarded and 50 µl of the staining solution (antibodies diluted in permeabilization/wash buffer, Table III-6) was added to each sample with 1 h incubation, in the dark, at 4 °C. After staining, the cells were washed with permeabilization/wash buffer and centrifuged at 500 xg for 5 min. The resultant pellet was resuspended in 100 µl of sorting buffer. For cell apoptosis, the cell pellet was resuspended in 10 µl of sandoglobulin and AnnexinV antibody (Table III-6) diluted in AnnexinV buffer. The samples were incubated for 15-25 min at 4 °C and 400 µl of AnnexinV buffer was added. All stained cell suspensions were filtered in 5 ml polystyrene tubes and analyzed by BD LSRFortessa™ Flow cytometer.

Table III-6. Staining antibodies for proliferation, infection, and apoptosis analysis of AEC.

Antibody	Clone	Fluorochrome	Dilution	Manufacturer
Ki67	11F6	PE	1:50	Biolegend
NP	D67J	FITC	1:20	Abcam
AnnexinV	-	Alexa Fluor 647	1:20	Biolegend

Cell priming, labelling and treatment

BM-MSC activation was performed by adding conditioning media into freshly seeded naïve BM-MSC, in 1:10 dilution. Conditioned media was recovered from either MOI 0.1 infected (PR8) AEC (48 h culture, UV-inactivated) or by bronchoalveolar lavage fluid (BALF) collection. BALF was collected by installing volumes of 0.3 ml, 0.4 ml, and 0.5 ml of PBS/EDTA into lungs from mock and day 3 or day 7 infected mice (500 foci forming units – ffu). All collected BALF was concentrated using Thermo Scientific™ Pierce™ Protein Concentrators PES (according to manufacturer's instructions). After confluency, activated BM-MSC were detached (Stem-Pro® Accutase®) and used in further experiments. BM-MSC were also stimulated with IFNα and IFNβ, at a concentration of 150 pg/ml or 20 pg/ml, respectively.

To follow or recover BM-MSC, the cells were labelled with Qtracker® Cell Labelling Kit 625 nanometers (nm). Labelling was performed according to manufacturer's instructions.

Confluent cells were detached (Stem-Pro® Accutase®) and the labelling mix (1 µl Qtracker® Component A and 1 µl Qtracker® Component B diluted in 200 µl of complete MSC media) was added for 45-60 min. After washing, the labelled cells were intra-tracheally injected and FACS-recovered from mock or infected mice or micro-injected in infected BALO.

Treatment of BM-MSC with silencing RNA (siRNA) was also performed to impair the expression of IL-11, according to manufacturer's instructions. Lipofectamine™ RNAiMAX transfection reagent and Silencer® Select IL-11 were diluted in Opti-MEM media and incubated for 5 min. The siRNA-lipid complex was added to 60-80% confluent cells for a minimum of 24 h. Silenced BM-MSC were then collected, frozen (see Isolation and culture of primary cells and cell lines) and used for further analyses.

Enzyme-Linked ImmunoSorbent Assay (ELISA)

Commercially available ELISA kits (R&D Systems) were used according to the manufacturer's instructions to determine the concentrations of IFNα, IFNβ, IFNγ and IL-11 from supernatants. Samples were stored at -80 °C and used undiluted. Cytokine concentration was quantified by colorimetric detection at 450 nanometers (nm) wavelength in a microplate reader (Bio-Rad) and calculated using a standard curve of known concentration samples. Each biological sample had three experimental replicates.

RNA isolation

RNA was isolated from flow-sorted cells using RNeasy Micro Kit, preceding RNA bulk sequencing analysis. After cell sorting, cells were centrifuged (500 xg, 10 min, 4 °C) and washed once with PBS. After a second centrifugation, cells were lyzed in 350 µl RLT buffer. RNA isolation was then processed according to the manufacturer's instructions. RNA concentration and purity were analyzed by spectrophotometry (Nanovue Plus, GE Healthcare).

Ex-vivo experiments

BALO generation and staining

This protocol is an adaptation on the original published by Vazquez-Armendariz *et al*, 2020 [33], replacing lung-MSC with BM-MSC. BASC ($EpCAM^{hi}$ $CD24^{low}$ $Sca\text{-}1^{+}$) were stained according to Table III-7 and flow sorted after AEC isolation (see Isolation and culture of primary cells and cell lines). Lung-MSC and BM-MSC were stained according to Table III-3

and Table III-4, respectively. For co-cultivation, approximately 4 000 BASC were co-culture with either 15 000-20 000 lung-MSC or 1 000-2 000 BM-MSC. The combined cell suspension was added to Matrigel® (in a 1:1 ratio) and cultured in 12 millimeters (mm) cell culture inserts, with αMEM supplemented with 10% FBS, 1% Pen/Strep/L-Glu, 1% insulin and 0.1% heparin (organoid medium). BM-MSC were seeded either as naïve or activated cells. Cultures were incubated under air-liquid conditions at 37 °C with 5% CO_2 for 21-26 days with organoid media being replaced every 2 days. To control the growth and analyze development, cysts were measured every 2-3 days and followed for 15-19 days by microscopy (see Microscopy). Branching/alveologenesis capacity was microscopically accessed. To stain for differentiated AEC2, LysoTracker™ Green DND-26 was added to organoid media with 1:100 dilution and incubated for 30 min at 4 °C. To remove the staining solutions, organoids were washed once with 3% BSA in PBS. Organoids were fixed (4% PFA, 4 °C) and used for nuclear staining, with one drop of NucBlue® Fixed Cell Stain ReadyProbes™ reagent Dapi Special Formulation added to 500 µl of organoid medium, for 40 min at 4 °C. Finally, the membrane was removed from the insert and mounted on glass slides for confocal or light microscopy analysis.

Table III-7. Staining antibodies and respective dilutions for sorting BASC with FACS, for the generation of BALO.

Antibody	Clone	Fluorochrome	Dilution	Manufacturer
CD24	M1/69	PE-Cy7	1:200	Biolegend
CD31	390	Alexa Fluor 488	1:50	Biolegend
CD45	30-F11	FITC	1:50	BD Biosciences
EpCAM (CD326)	G8.8	APC-Cy7	1:50	Biolegend
Sca-1 (Ly-6A/E)	D7	PB	1:50	Biolegend

BALO microinjection – preparation, infection, and cell injection

On day 21 of the BALO development, microinjection of virus and cells was performed. Before the procedure, the membrane was cut from the insert and transfered to 145 µm Cell Imaging Dishes with Matrigel® filled-0.5 mm iSpacers IS008. The next day, microinjection was performed using an oil-filled microinjection system (CellTram®Vario, Eppendorf) with 14 µm diameter capillary needle and DMIL LED microscope (Leica). Cultures were kept in the incubator with 5% CO_2 at 37 °C until further analysis.

For infection, the organoid cultures were washed once with PBS and infected with mock (PBS) or virus (see Influenza-A virus (IAV) strains). PBS or virus solution was aspirated inside the capillary needle and injected inside the BALO (in air-liquid conditions with αMEM supplemented 1% Pen/Strep/L-Glu and 0.2% BSA). For cell injection, a drop of cell

suspension in polyvinylpyrrolidone (PVP) solution was placed into a low attachment plastic insert for 5-10 min at RT and aspirated into the capillary needle. Both infection and cell injection were followed by microscopy and prepared for analysis according to above mentioned protocols.

In-vivo experiments

Intra-tracheal IAV infection

For *in-vivo* infection, animals were sedated by isoflurane inhalation. During anesthesia, mice were kept warm to maintain a stable body temperature. The mouse's nose was inserted into a mask constantly releasing isoflurane and oxygen and his body extremities were fixed with chirurgical tape, to ensure the stretching of the respiratory airways. The stand was rotated to a 45-degree angle and the tongue was rolled out to allow the insertion of an intubation guide wire coupled with an endotracheal tube that reached the trachea. The guide wire was removed, securing the endotracheal tube in place. Using a Hamilton syringe, mice were inoculated with 500 ffu of PR8 virus, diluted in 50 µl of sterile PBS. After installation, mice were removed from the isoflurane mask and monitored until complete recovery.

Intra-tracheal cell application

The cell (or PBS) application followed the same guidelines as the mouse intra-tracheal (IT) infection. 250 000 cells diluted in 50 µl of sterile PBS were applied 3 days post infection (dpi). In cell application experiments, BM-MSC were used in different conditions –naïve, stained, pre-conditioned, or treated. 3T3 cell line was used as cell control and PBS as negative control.

Lung preparation and BALF collection

At the end of each *in vivo* experiment, both lung homogenate (LH) and BALF were collected. Mice were sacrificed by cervical dislocation, while under isoflurane anesthesia. LH preparation starts with the opening of the chest cavity to access the lungs, followed by perfusion with sterile Hank's balanced salt solution (HBSS) via the right ventricle. A small incision made into the trachea was used to fill the lung with 1.5 ml of sterile dispase (via a shortened 21-gauge cannula). The lungs and trachea were resected, washed in PBS, and placed in dispase for 40 min at RT. The homogenized lung was then processed to obtain either AEC, lung-MSC or recover injected BM-MSC.

For BALF collection, a small tracheal incision was made, and a 21-gauge cannula inserted. Consecutive instillations and collection of 300 µl, 400 µl and 500 µl of ice-cold 2 mM EDTA/PBS were performed. The supernatants were used for BALF concentration and stored at -80 °C.

Recovery of labeled BM-MSC

Following BM-MSC labelling (see *In-vitro* experiments) and intra-tracheal application (see *In-vivo* experiments), the LH was prepared to recover the marked cells. A simplified version of the AEC isolation protocol (see Isolation and culture of primary cells and cell lines) is applied and stopped right before biotinylated rat anti-mouse antibodies are added. The cell suspension is stained according to Table III-8 and labelled BM-MSC are flow sorted as $CD45^-$ $CD31^-$ $Ter119^-$ $TexasRed^+$, using BD FACSAria III™ Cell sorter and analyzed by bulk-RNA sequencing.

Table III-8. Staining antibodies and respective dilutions for FACS recovery of labelled BM-MSC.

Antibody	Clone	Fluorochrome	Dilution	Manufacturer
CD31	390	Alexa Fluor 488	1:50	Biolegend
CD45	30-F11	FITC	1:50	BD Biosciences
Ter119	TER-119	FITC	1:50	Biolegend

Bulk-RNA sequencing

After isolation, RNA was extracted (see *In-vitro* experiments) from FACS-recovered AEC and intra-tracheal injected BM-MSC. Both lung-MSC and cultured BM-MSC were also isolated as controls, and their RNA extracted for bulk-RNA sequencing. All the samples were subjected to QC (quality control) analysis before entering the RNA sequencing (RNAseq) pipeline, performed at the Deep Sequencing Platform, by Dr. Stefan Günther, from Max Planck Institute for Heart and Lung Research in Bad Nauheim, Germany. Depending on the QC and RNA concentration, samples were chosen for analysis. A minimum of four biological replicates were analyzed per condition and a minimum of three biological replicates were selected to be presented in the final plots. The RNAseq pipeline followed standard protocols, starting with mapping of the RNA, gene count for each sample and elaboration of a matrix, combining samples and conditions. The final analysis was performed using correlations of Rlog/Spearman and TOP50 DEG Heatmaps Plots.

Microscopy

Microscopic images for bright field were taken using EVOS^{TM} FL Auto Imaging System (Thermo Fisher Scientific). For confocal pictures, a Leica SP8 DMi microscope running on LAS X 3.5.7 software was used, together with a multi-photon laser Spectra Physics Insight X3^{+}. The objectives utilized were 10X Air 0.4NA, 20X Air 0.75NA and 25X Water 0.95NA. The raw images were processed using Fiji (version 2.1.0/1.53c) [156]. For organoid area quantification, confocal z-stacks were acquired for each organoid with the eGFP channel corresponding to the virus-infected cells, while the tdTomato signal indicating the mT/mG. For analysis, a custom-made ImageJ/Fiji macro was used to generate a maximum intensity projection for each organoid. With the user's input, the organoids were delineated, with the background signals from the infected areas (eGFP) and the organoid areas (tdTomato) being automatically excluded. The measure was taken from total area selection (in μm^2) of eGFP and tdTomato positive pixels, corresponding to the infected and organoid area, respectively. The results were presented as the ratio of infected area/organoid area.

Histological assessment of the lung

To prepare the lung for paraffin embedment, mice were sacrificed by cervical dislocation, while under isoflurane anesthesia and their trachea and chest were carefully exposed. The lung was perfused with HBSS and following tracheostomy and the trachea was cannulated. 4% PFA was carefully instilled through the trachea to fill in the lobes, and the lung was removed and transferred into 4% PFA solution overnight, at 4 °C. The lung was then placed for dehydration for 13 h (Leica Tissue Processor) and finally embedded in paraffin (Leica ASP200S). Afterwards, 3-5 μm thick tissue sections were cut, put on slides, and kept at RT until hematoxylin/eosin (H&E) staining.

Tissue cuts were prepared for H&E staining by submerging the slides in xylol for 5 min (twice), ethanol (EtOH) 100% for 30 s (twice), EtOH 96% for 30 s (twice) and EtOH 70% for 30 s (twice). Hematoxylin was then added for 3 min, washed away with hydrochloric acid and water, followed by eosin staining for 3 min, washed away using water. To fix the stain, the slides were flooded in EtOH 70% for 20 s (twice), EtOH 96% for 20 s (twice), EtOH 100% for 20 s and 2 min, and xylol for 5 min (twice). Stained tissue cuts were analyzed using bright field.

Statistics

All data are given as mean ± standard error of mean (SEM). Statistical significance between two groups was estimated using the unpaired Student's t test. For three group comparison, ANOVA test were performed. Calculations were done with GraphPad Prism 9 (GraphPad Software, Inc.). P-values lower than 0.05 were considered significant.

IV. Results

IV.1. Lung-MSC can respond to IAV-infection *in vivo* and exhibit protective effects towards infected AEC *in vitro*

Mesenchymal stem cells present in the lung alveolus play an important role in alveolar regeneration. The PDGFRα$^+$ cell population can interact with both alveolar epithelial and endothelial cells and support AEC2 self-renewal and differentiation [1], [9], [26]. To investigate the active role of lung-MSC in viral infection, it is important to characterize these cells during homeostasis. Lung-MSC were isolated from lung homogenate of adult mice by FACS, and cell suspension was subjected to doublet discrimination followed by live-cell selection (SYTOX$^+$). After exclusion of leukocytes, endothelial and epithelial cell populations (CD45$^-$ CD31$^-$ EpCAM$^-$), lung-MSC were isolated based on PDGFRα$^+$ Sca-1$^+$ expression profile (Figure **IV-1**). Sorted cells had always ~90% purity. Following cell sorting, lung-MSC were seeded, expanded for 3-5 passages, and used in subsequent experiments.

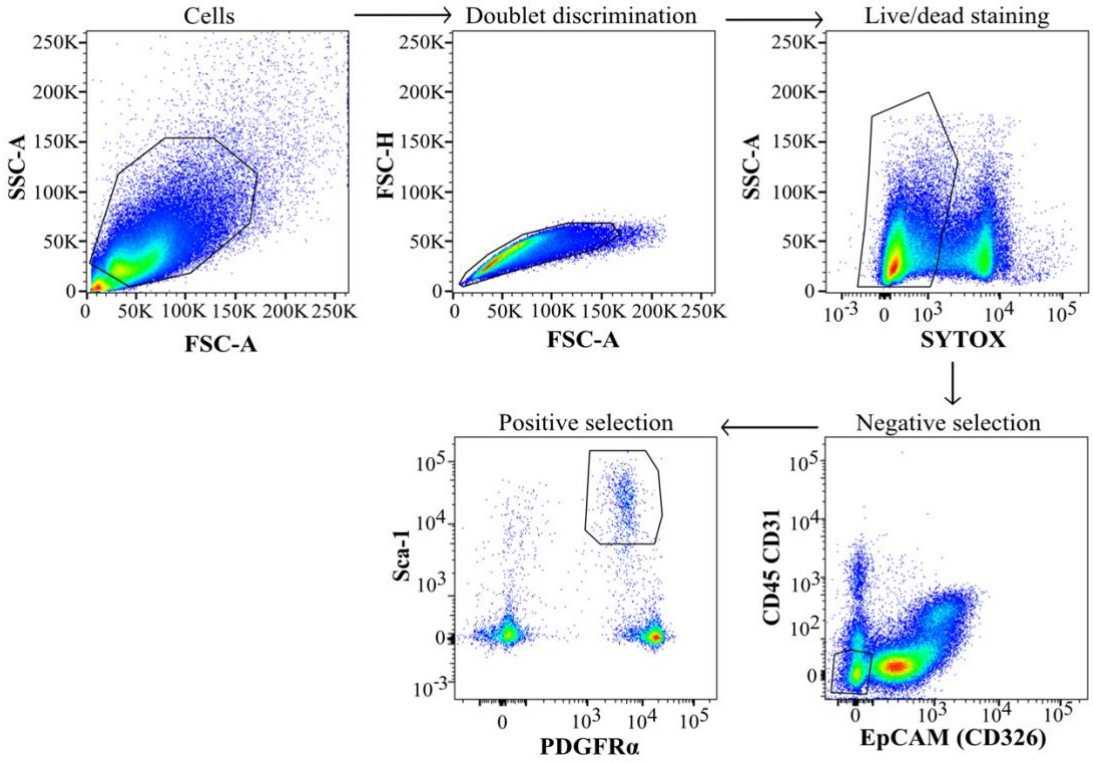

Figure IV-1. Lung-MSC isolation from adult murine lungs. Gating strategy for cell sorting of lung-MSC after lung homogenization. After leukocyte, endothelial and epithelial exclusion, the cell suspension was subjected to doublet discrimination and live-cell selection (SYTOX$^+$), with the mesenchymal population being sorted based on the CD45$^-$ CD31$^-$ EpCAM$^-$ PDGFRα$^+$ Sca-1$^+$ expression signature.

To assess lung-MSC population´s response to viral infection, cells isolated from mock (PBS) or 3 dpi (PR8) adult murine lungs were analyzed by bulk RNAseq. For these experiments, 3 biological replicates with 20-25 000 cells/sample were used for each condition.

Figure IV-2. Heatmap and Gene Set Enrichment for mock (PBS) or PR8 isolated lung-MSC. (A) Heatmap of top 50 differently expressed genes (DEG) from lung-MSC recovered from mock (PBS) or 3 dpi PR8 infected mice. Red squares represent upregulated genes and blue squares represent downregulated genes, with Z-score from -2 to 2. N=3 biological replicates. **(B-C)** DEG up and down regulated after gene set enrichment using KOBAS, with each graph representing the top 10 gene sets or pathways enriched from **(B)** gene ontology or **(C)** PANTHER databases. Dashed line represents a p-value=0.05. log10 FDR are represented as dark green for significantly upregulated in PR8, light green for not-significant up-regulation in PR8, dark red for significantly downregulated in PR8 and light red for not-significant down-regulation in PR8.

The top 50 up- and down-regulated genes were presented in a heatmap (Figure **IV-2**. A) with a false-discovery-rate (fdr) lower than 0.05. Gene Set Enrichment (using KOBAS) graphs with fdr lower than 0.2 were generated from gene ontology (Figure **IV-2**. B) and PANTHER (Figure **IV-2**. C) databases, with p-value=0.05 represented by a dashed line. Within the heatmap top cluster (Figure **IV-2**. A), genes involved in cell differentiation (*Fat3* and *Rtkn2*), wound healing and epidermal cell migration (*Macf1*) and recruitment of mesenchymal cells into epithelial structures (*Itga8*) were downregulated in lung-MSC isolated from PR8-infected lungs. Contrarily, interferon type I and II genes (*Mx1*, *Gbp11*, *Cmpk2*, *Ccl2*), anti-inflammatory genes (*Chil1*, *Hp*, *Lipg*, *Ptx3*, *Fam26f*) and genes related to stem cell self-renewal, proliferation, and pluripotency (*Psat1*, *Tk1*, *Aspm*, *Cenpe*, *Top2a*, *Mki67*) were upregulated in lung-MSC obtained from virus-infected lungs. After gene set enrichment analysis (Figure **IV-2**. B-C), pathways with a p-value lower than 0.05 upregulated in lung-MSC isolated from PR8-infected mice included cell cycle, response defence to virus, negative regulation of viral genome replication and interleukin signalling pathways. The change in the transcriptomic profile in lung-MSC after viral exposure suggests an increased stem-cell potential of the population as shown by upregulation of genes related to stem cell self-renewal and pluripotency, and an anti-viral response directed towards the infected lung epithelium, given the strong upregulation of interferon type I and II related genes.

To further prove the protective effects of lung-MSC, proliferation (Ki67), apoptosis (AnnexinV), and virus detection (NP) in mock and infected AEC (iAEC, MOI 0.1, PR8) were tested with and without the presence of lung-MSC in a co-culture model, 24 and 48 hours post infection (hpi) using flow cytometry (Figure **IV-3**). Co-culture of un-infected AEC with (16% ±1.7) and without lung-MSC (15.5% ±0.6) did not cause a significant difference in AEC proliferation after 24 h (Figure **IV-3** A.). Conversely, iAEC proliferative capacity increased in the presence of lung-MSC, from 4.2% ±1.8 to 39.5% ±2.2 $Ki67^+$AEC 24 hpi. Similar results were obtained at 48 hpi (Figure **IV-3** A.). The percentage of $AnnexinV^+$ AEC were similar in both time points, either with (31% ±2.6, 24 hpi and 26.8% ±2.7, 48 hpi) or without lung-MSC (32.2% ±3, 24 hpi and 25.5% ±1.7, 48 hpi) ((Figure **IV-3**. B.).

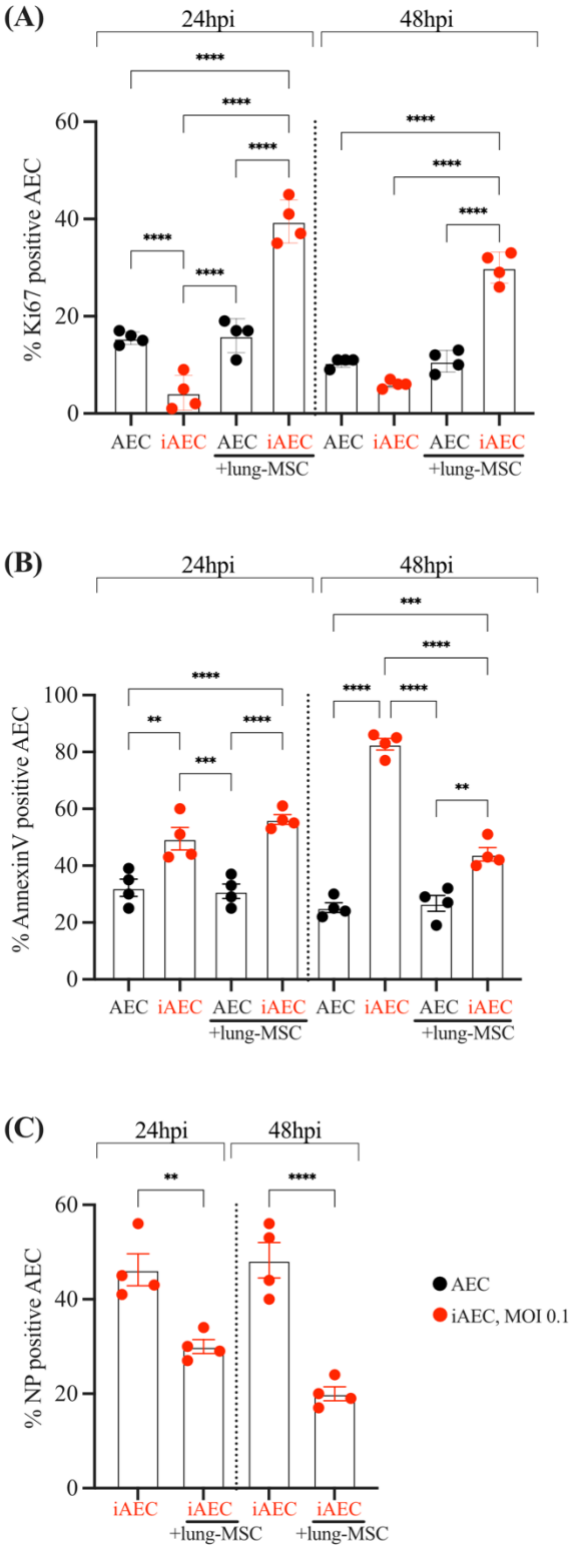

As expected, infection-related apoptosis increased in a time dependent manner, with 49.5% ±3.9 AnnexinV$^+$ iAEC after 24 hpi and 82.7% ±2 AnnexinV$^+$ iAEC after 48 hpi. Notably, while 24 hpi co-culture with lung-MSC failed to reduce AEC apoptosis levels, a significant decrease in apoptotic iAEC was observed after 48 hpi (44.4% ±2.4). Lastly, a decrease in the percentage of NP expression was observed in iAEC co-cultured with lung-MSC, indicating a possible anti-viral effect, more prominent at 48 hpi (20% ±1.4, compared to 30% ±1.5 after 24 hpi) (Figure **IV-3** C.)

In summary, these results show that the lung-MSC population is active and responsive to viral infections and thus suggested to play an active role in aiding epithelial cell recovery after damage.

Figure IV-3. Lung-MSC protective effects towards iAEC *in vitro*. (A) Proliferation, **(B)** apoptosis and **(C)** NP expression of mock (black) and infected (MOI 0.1, PR8) (red) AEC co-cultured with and without lung-MSC after 24 and 48 hpi (N=4 biological replicates). AEC alveolar epithelial cells, hpi hours post infection, iAEC infected alveolar epithelial cells, MSC mesenchymal stem cells, MOI multiplicity of infection. Bar charts presented as mean ± SEM and probability determined using one-way ANOVA (*p<0.05, **p<0.01, ***p<0.001, ****p<0.0001).

IV.2. Bone-marrow isolated mesenchymal stem cells have stem cell potential and exert similar AEC protective effects as lung-MSC

Due to their accessibility, expandability, and multipotent nature, BM-MSC hold significant promise for applications in regenerative medicine [82]. Matsuzaki *et al.* demonstrated that mouse adult BM-MSC can be isolated by combining PDGFRα and Sca-1 [84]–[87]. Several research groups have validated that BM-MSC could reduce the severity of lung injury primarily through the release of paracrine factors. In the present work, isolation of murine BM-MSC was performed by bone flushing, followed by FACS. The cell suspension was subjected to doublet discrimination followed by live-cell selection ($SYTOX^+$). After excluding the leukocyte and endothelial cell populations ($CD45^-$ $Ter119^-$ $CD31^-$), BM-MSC were flow-sorted based on the $PDGFR\alpha^+$ $Sca\text{-}1^+$ expression profile (Figure **IV-4**).

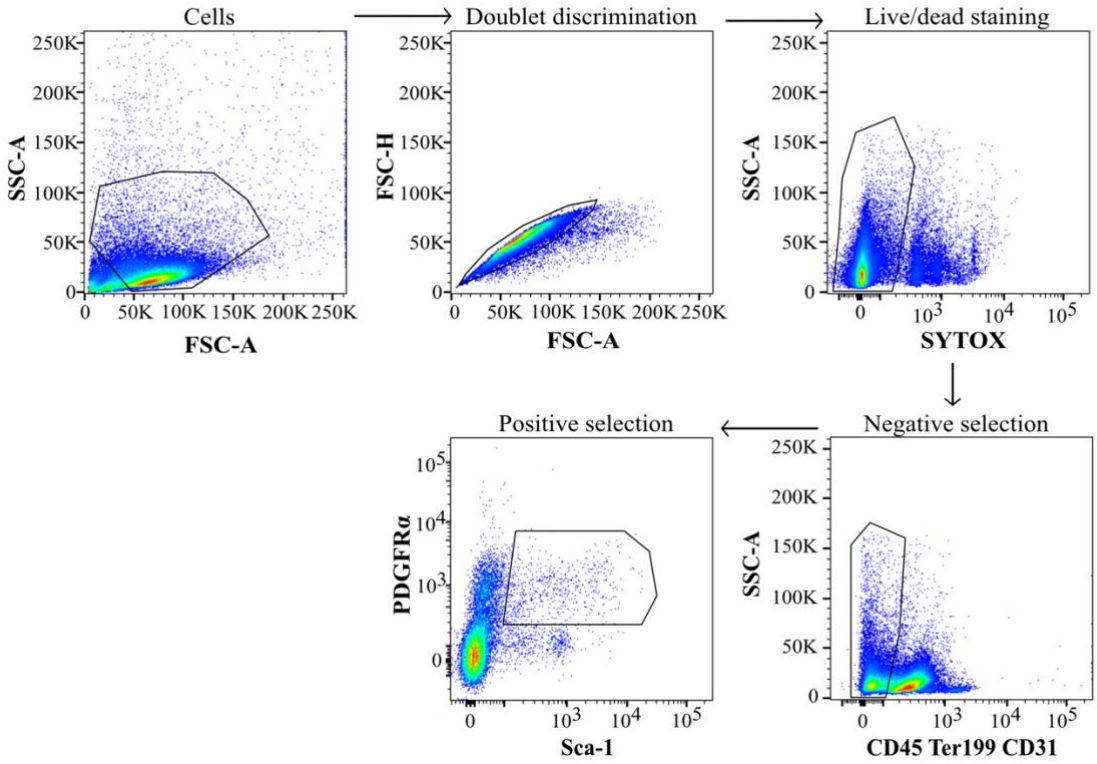

Figure IV-4. BM-MSC isolation from healthy adult murine bone marrow. Gating strategy for cell sorting of BM-MSC after bone flushing. The cell population was subjected to doublet discrimination and live-cell selection ($SYTOX^+$), with sorted mesenchymal population having a $CD45^-$ $Ter119^-$ $CD31^-$ $PDGFR\alpha^+$ $Sca\text{-}1^+$ signature.

Following cell sorting, the BM-MSC population had a purity always higher than 90%. After isolation and characterization, the cells were seeded, expanded for 5-10 passages, and used in subsequent experiments. BM-MSC were tested after several passages to assess stem cell potential according to ISCT criteria. After approximately 15 passages, BM-MSC stayed negative for leukocyte (CD11b, CD19, CD45), hematopoietic (CD34), and endothelial cell

(CD31) markers and stained positive for stem cell markers CD44, CD105, CD117, Sca-1 and PDGFRα (CD140a) (Figure **IV-5**. A). Phenotypically, BM-MSC remained adherent to plastic and were able to differentiate into osteoblasts, adipocytes and chondroblasts *in vitro* (Figure **IV-5**. B-C) [75], [76].

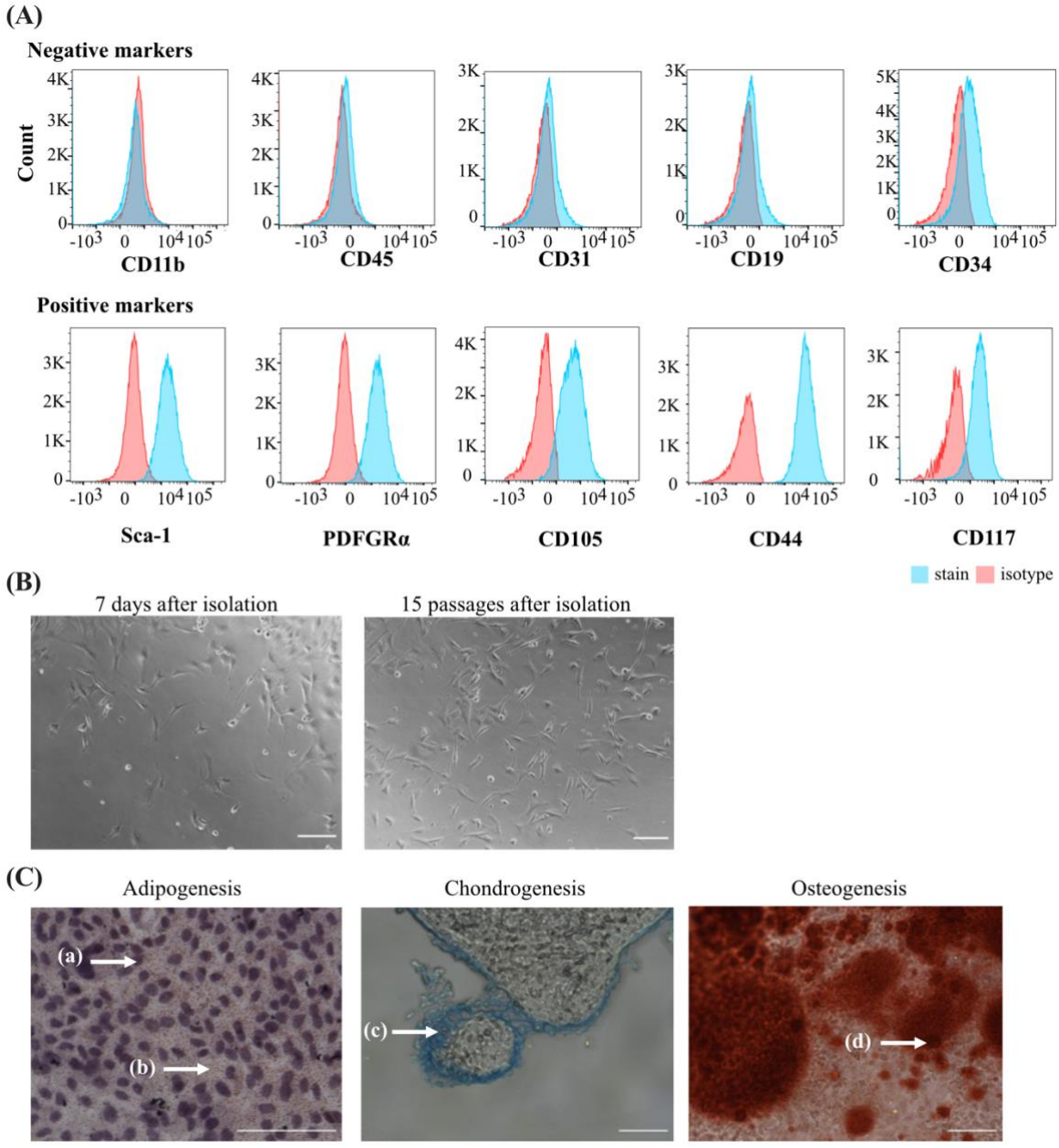

Figure IV-5. BM-MSC characterization. (A) Flow cytometric histograms of surface expression in BM-MSC of negative (CD11b, CD45, CD31, CD19 and CD34) and positive (Sca-1, PDGFRα, CD105, CD44 and CD117) markers after 15 passages. Red histograms represent isotype control and blue histograms represent stained sample. **(B)** Microscopic images of BM-MSC 7 days after flow cytometric isolation and after 15 passages. **(C)** Microscopic images of BM-MSC differentiation into adipocytes, chondrocytes, and osteocytes after 15 passages. Arrows represent (a) nuclei staining in blue using hematoxylin, (b) lipid droplets stained with Oil Red O, (c) acidic polysaccharides present in cartilage spheroids stained with Alcian Blue and (d) extracellular calcium deposits produced by osteocytes stained with Alizarin Red. Scale bars represent 144 µm.

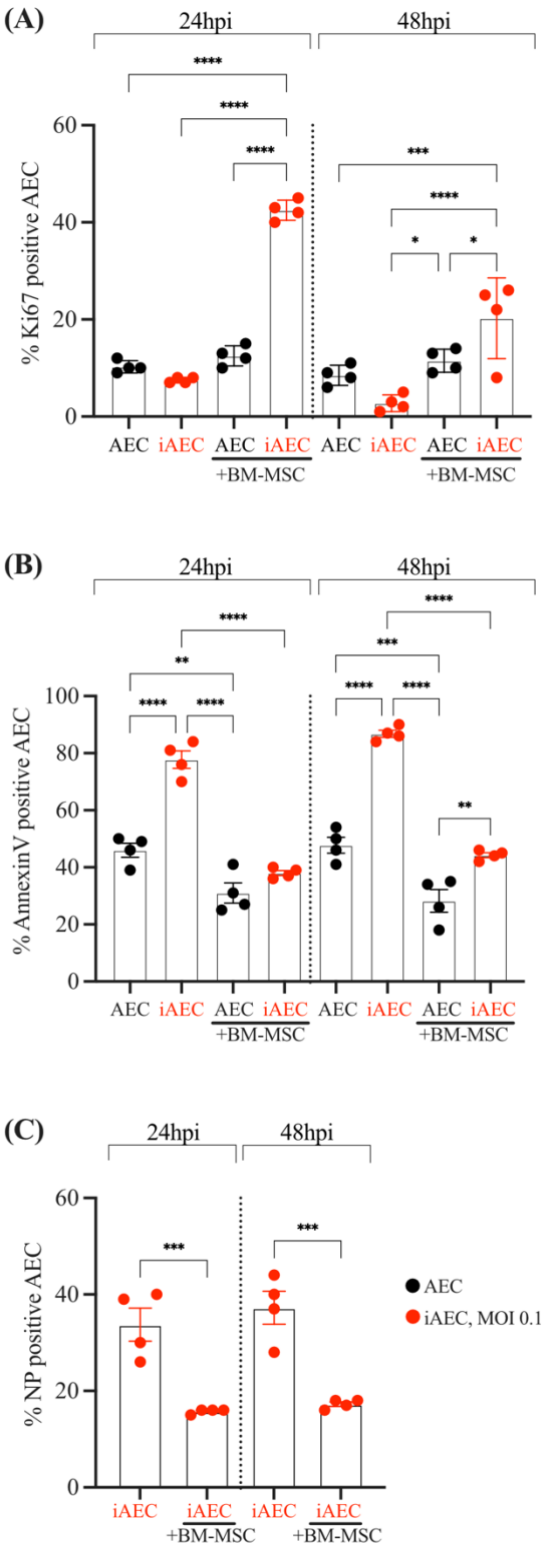

When considering cell-based therapies, BM-MSC have been extensively used for the treatment of multiple diseases. In ARDS, BM-MSC have been shown to reduce the severity of lung injury but the underlying mechanisms by which MSC exert their beneficial effects are not well known. The first hallmark was to confirm that BM-MSC can respond to IAV-infection. To test this hypothesis, BM-MSC were co-cultured with iAEC (MOI 0.1, PR8) for 24 h and 48 h, with AEC proliferation, apoptosis, and virus detection assessed by flow cytometry (Figure **IV-6**). AEC proliferation was not altered by the presence (12.5% ±1, 24 h) or absence (10.25% ±0.6, 24 h) of BM-MSC (Figure **IV-6**. A). However, PR8 infection negatively affected iAEC proliferation (24 hpi at 7.5% ±0.3 and 48 hpi at 2.75% ±0.8 $Ki67^+$ iAEC) while BM-MSC co-culture considerably increased the number of $Ki67^+$ iAEC (42.5% ±1, 24 hpi and 20.2% ±4.2, 48 hpi). Regarding cell apoptosis, BM-MSC showed anti-apoptotic effects towards iAEC (Figure **IV-6**. B). The percentage of $AnnexinV^+$ AEC after 24 h (38% ±0.9) or 48 h (44.25% ±0.8) was significantly lower in BM-MSC co-cultures when compared to $AnnexinV^+$ iAEC seeded alone (77.75% ±3.1 for 24 hpi and 86.75% ±1.2 for 48 hpi).

Figure IV-6. BM-MSC proliferative, anti-apoptotic and anti-viral effects towards iAEC *in vitro*. (A) Proliferation, **(B)** apoptosis and **(C)** NP expression of mock (black dots) and infected (MOI 0.1, PR8) (red dots) AEC co-cultured with and without BM-MSC for 24 hpi and 48 hpi (N=4 biological replicates). AEC alveolar epithelial cells, hpi hours post infection, iAEC infected alveolar epithelial cells, BM-MSC bone marrow-derived mesenchymal stem cells, MOI multiplicity of infection. Bar charts presented as mean ± SEM and probability determined using one-way ANOVA (*p<0.05, **p<0.01, ***p<0.001, ****p<0.0001).

To evaluate the anti-viral potential of BM-MSC, the percentage of NP^+ iAEC was assessed. BM-MSC presence decreased NP expression from 33.7% ±3.4 to 15.7 ±0.2 at 24 hpi and from 37.2% ±3.4 to 17.2 ±0.5 at 48 hpi (Figure **IV-6**. C). In summary, BM-MSC showed protective effects towards iAEC *in vitro,* by increasing their proliferative capacity, while reducing cell apoptosis and percentage of virus-infected cells.

IV.3. BM-MSC change their phenotype after being exposed to IAV and depend on external activation to potentiate their protective effects

Human BM-MSC administration has been shown to reduce lung endothelial injury and restore alveolar fluid clearance in *E. coli* endotoxin-induced lung injury models [134]. However, the molecular mechanisms by which BM-MSC act in the lung compartment are not fully understood in the context of influenza.

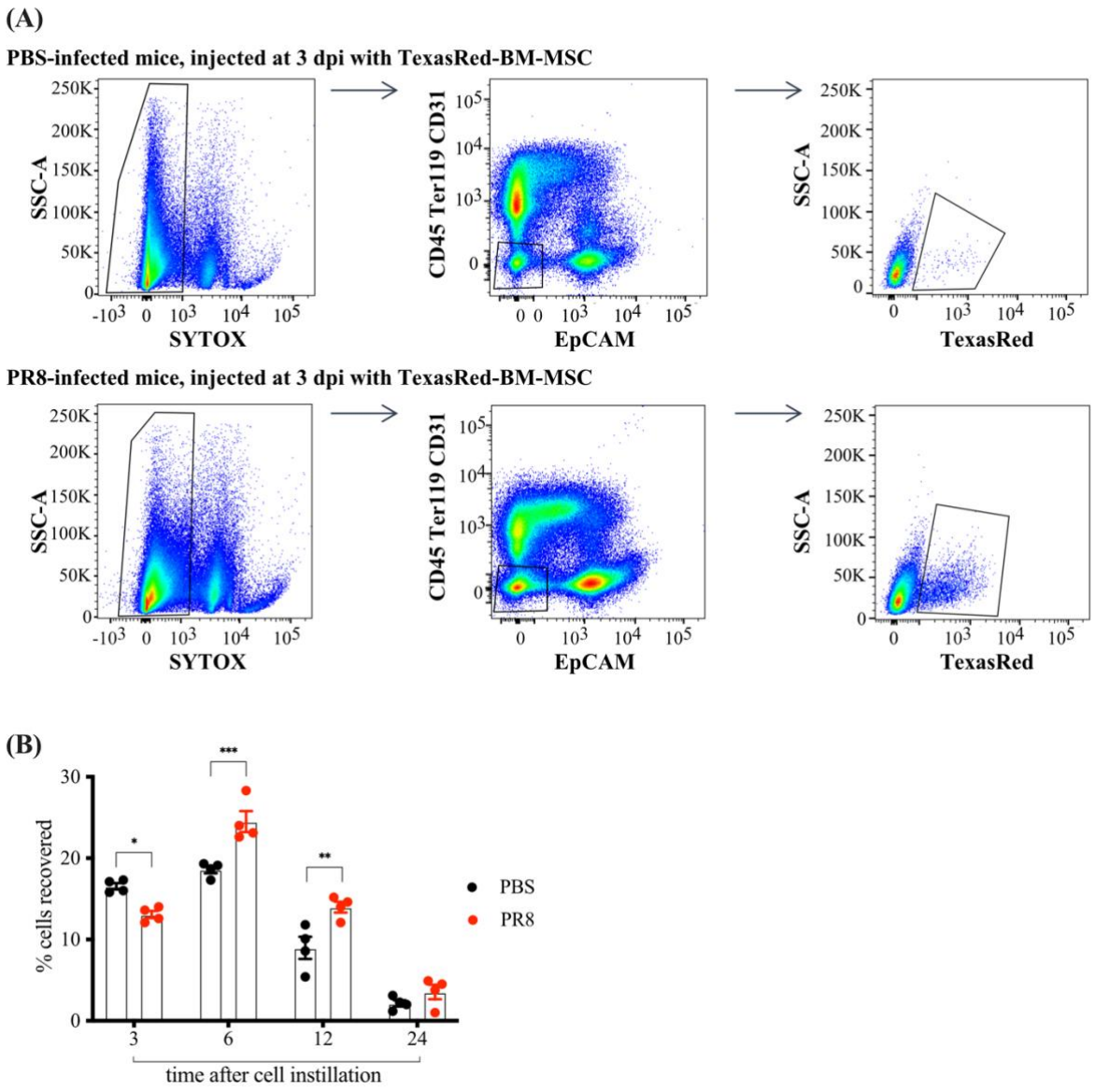

Figure IV-7. Recovery of TexasRed-BM-MSC from adult 3-day mock- or PR8- infected murine lung homogenate. (A) Example of gating strategy (6 h after cell instillation) used in FACS to recover TexasRed-BM-MSC delivered 3 dpi from mock (PBS) or PR8 infected (500 ffu) murine lungs. The cell population was subjected to doublet exclusion and live-cell selection ($SYTOX^+$), with the sorted mesenchymal population being $CD45^-$ $Ter119^-$ $CD31^-$ $EpCAM^-$ $TexasRed^+$. **(B)** Percentage of FACS recovered TexasRed-BM-MSC after 3 h, 6 h, 12 h or 24 h post-instillation. Cells were intra-tracheally delivered 3 days after mock-PBS (black) or PR8 (red) infection. N=4 biological replicates. Bar charts presented as mean ± SEM and probability determined using two-way ANOVA (*p<0.05, **p<0.01, ***p<0.001, ****p<0.0001).

After revealing that murine BM-MSC can increase iAEC proliferation and reduce infection-associated apoptosis as well as number of virus-infected cells *in vitro*, it was necessary to understand how IT-delivered BM-MSC would interact with the infected lung epithelium *in vivo*. For this purpose, confluent BM-MSC labelled with Qtracker® TexasRed (625 nm) were IT-delivered to day 3 mock-(PBS) or PR8-infected (500 ffu) mice. BM-MSC were recovered 3 h, 6 h (Figure **IV-7**. A), 12 h and 24 h post-instillation with BM-MSC numbers being accessed by FACS (Figure **IV-7**. B) using the BM-MSC signature $CD45^-$ $Ter119^-$ $CD31^-$ $EpCAM^-$ and TexasRed live cell labelling. Flow cytometric analysis indicated that 6 h post-cell administration was the time point where it was possible to recover higher cell numbers (illustrative gating strategy in Figure **IV-7**. A), being the preferred period for BM-MSC recovery. From 250 000 TexasRed-BM-MSC delivered, 18.6% ±0.5 was retrieved from mock-infected lungs while 24.5% ±1.3 was obtained from PR8-infected lungs. For longer time points, a higher percentage of BM-MSC was recovered from PR8-infected lungs (13.9% ±0.6 for 12 h and 3.6% ±0.8 for 24 h). BM-MSC recovery 3 h after IT-injection resulted in higher cell numbers obtained from mock-infected lungs (16.5% ±0.4) compared to PR8-infected lungs (13.1% ±0.4).

Within the lung compartment, IT-instilled BM-MSC are thought to communicate directly with AEC via paracrine release or cell-to-cell contact. However, the distinct molecular mechanisms involved in BM-MSC/AEC communication are not yet fully understood. RNA-bulk sequencing was performed to determine the transcriptomic changes on both BM-MSC and AEC populations. Flow sorted BM-MSC and AEC from non-infected (mock, PBS) and infected (PR8) murine lungs were analyzed. The top 50 expressed genes for each cell population were presented in heatmaps (Figure **IV-8** and Figure **IV-10**), with a false-discovery-rate (fdr) lower than 0.05. Gene Set Enrichment (using KOBAS) graphs with fdr lower than 0.2 were developed from gene ontology (Figure **IV-9** and Figure **IV-11**) databases, with pvalue=0.05 represented by a dashed line.

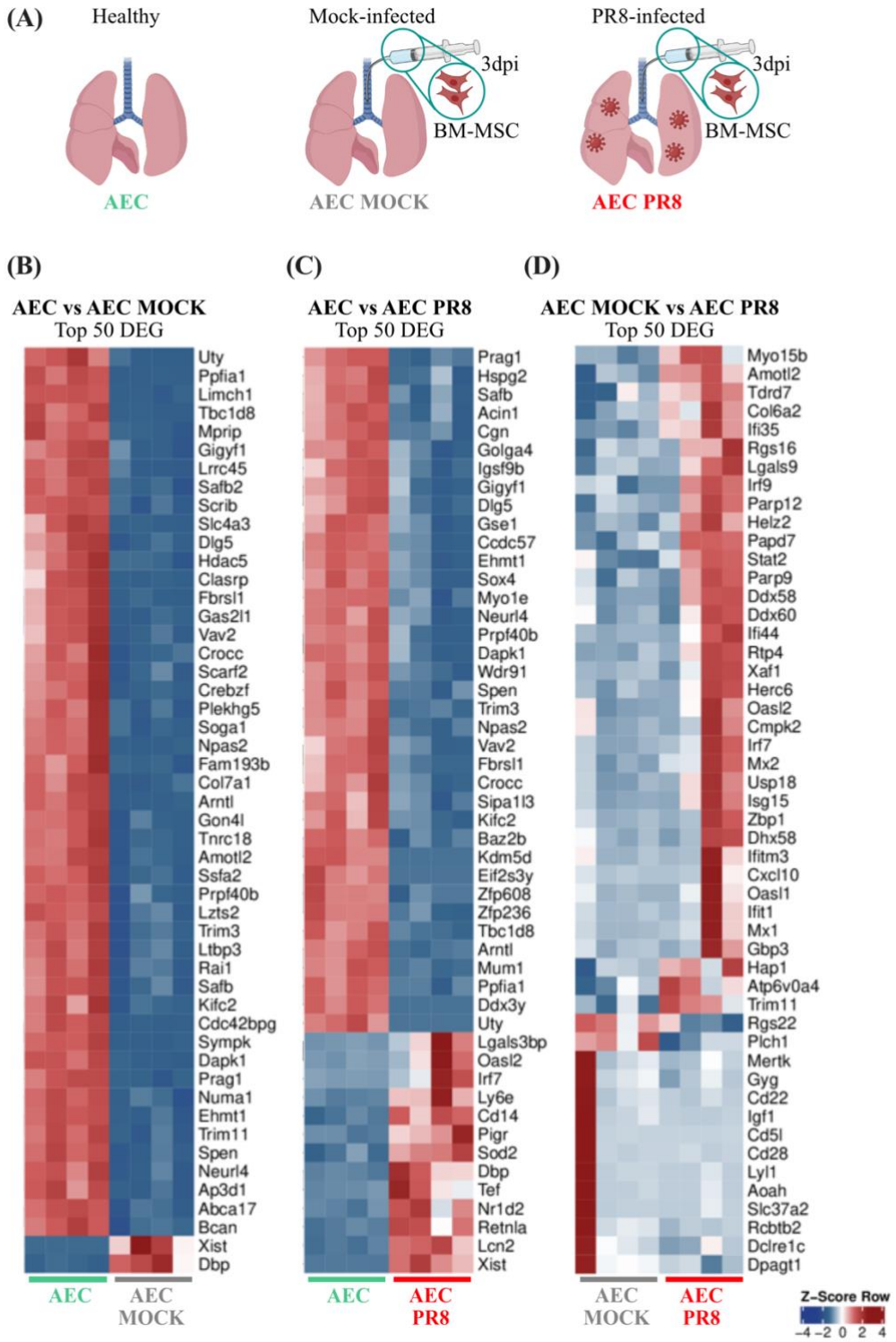

Figure IV-8. Heatmaps of top 50 expressed genes in AEC flow-sorted from healthy lungs, and from mock or PR8 infected lungs (3 dpi, 500 ffu) IT injected with BM-MSC (for 6 h). (A) Graphical representation of AEC isolation conditions. AEC (green) represent alveolar epithelial cells flow sorted from healthy lungs, AEC MOCK (grey) represents AEC flow sorted from mock-infected (PBS) lungs, treated with BM-MSC 3 days after mock infection, and AEC PR8 (red) represents AEC flow sorted from 500 ffu PR8-infected lungs, treated at 3 dpi with BM-MSC. **(B-D)** Heatmaps highlighting the **(B)** comparison between AEC and AEC MOCK, **(C)** comparison between AEC and AEC PR8 and **(D)** comparison between AEC MOCK and AEC PR8. In the heatmaps, Z-score Row are presented as red squares for the most upregulated genes and blue squares for most downregulated genes. N=4 biological replicates for all groups.

When in contact with BM-MSC, AEC significantly changed their transcriptomic profile (Figure **IV-8**). As expected, infected AEC upregulated genes related to virus response like innate immune response (*Cd14*, *Lcn2*), cellular response to interferon beta (*Irf7*) and negative regulation of viral genome replication (*Oasl2*, *Ly6e*) (Figure **IV-8**. C). Remarkably, BM-MSC's presence in the lung upregulated pathways related to AEC protection towards infection, such as negative regulation of viral genome replication and entry into host cell (*Oasl1*, *Oasl2*, *Isg15*, *Ifitm3*), positive regulation of type I interferon mediated signaling pathway (*Irf7*) and RIG-I like receptor signaling pathway (*Trim11*) (Figure **IV-8**. C and Figure **IV-9**).

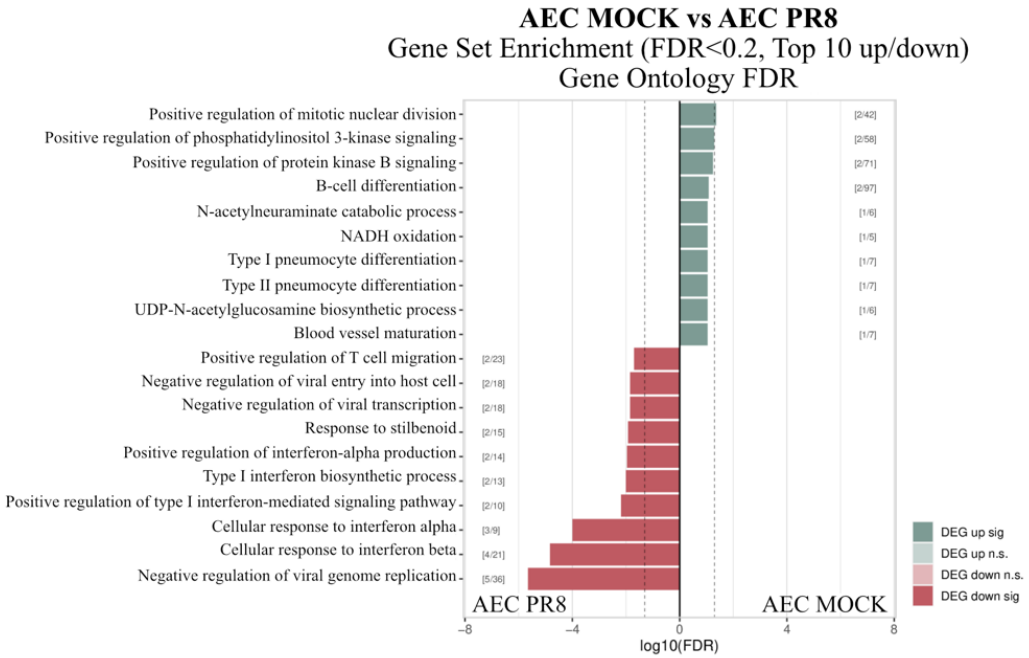

Figure IV-9. Gene set enrichment from flow-sorted AEC, isolated from 3 dpi mock (PBS) or PR8 infected (500 ffu) murine lungs, IT injected with BM-MSC (for 6 h). DEG up and down regulated genes after gene set enrichment using KOBAS, with graph representing the top 10 gene sets or pathways enriched from gene ontology database. Dashed line represents a pvalue=0.05. log10 FDR are represented as dark green for significantly upregulated in AEC MOCK, light green for not-significant up-regulation in AEC MOCK, dark red for significantly downregulated in AEC MOCK and light red for not-significant down-regulation in AEC MOCK. N=4 biological replicates for all groups.

IT-delivered (3 dpi) and FACS-recovered (6 hp-instillment) BM-MSC were also analyzed by RNA bulk-sequencing. Promptly, their transcriptomic profile was significantly changed upon being delivered in the lung compartment (Figure **IV-10**. B).

IT-delivered BM-MSC expressed *Sox9*, an important transcription factor for stem cell maintenance, not upregulated in BM-MSC isolated from the bone marrow (Figure **IV-10**. B).

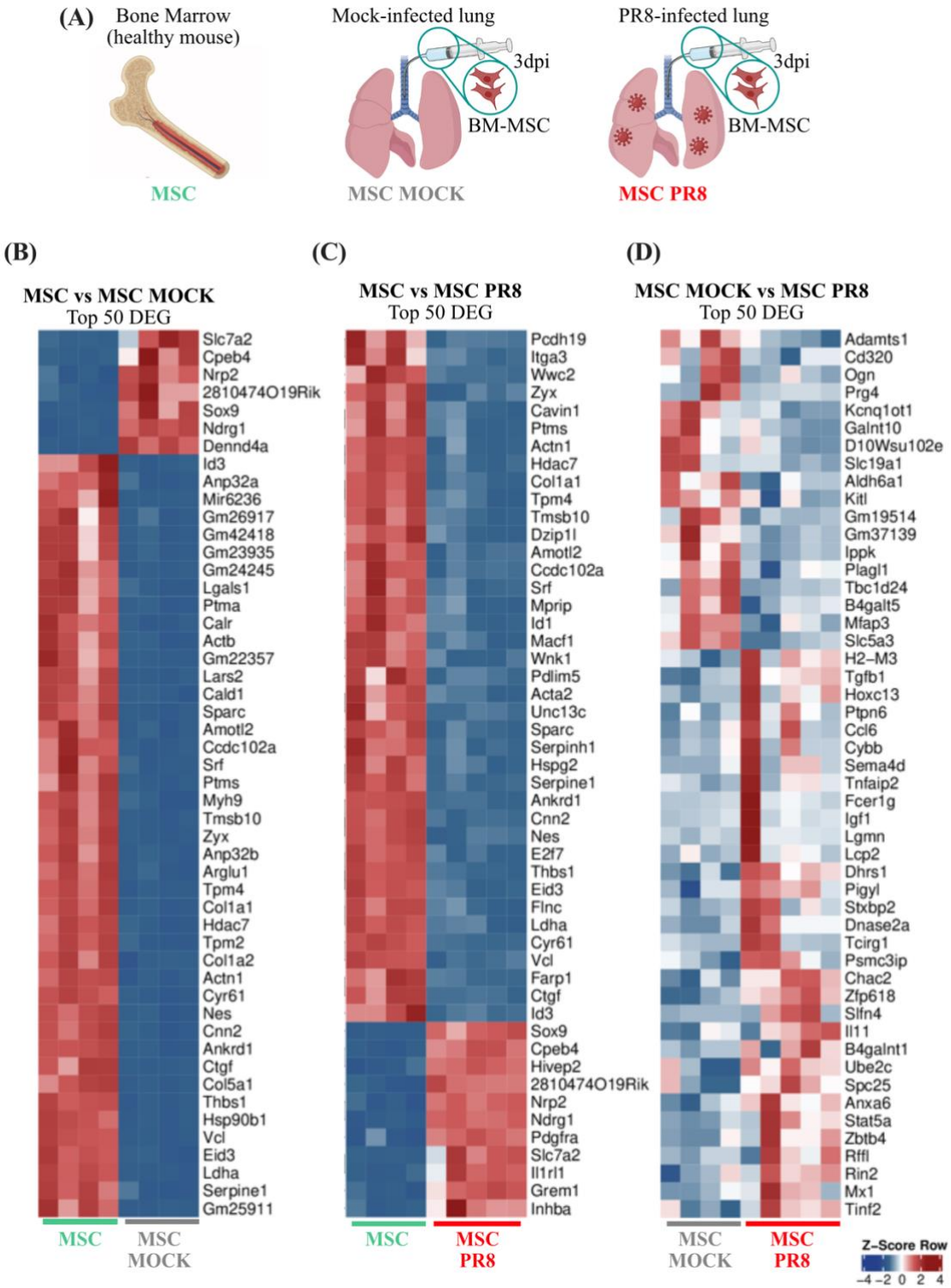

Figure IV-10. Heatmaps of top 50 expressed genes in BM-MSC isolated from bone marrow, and flow sorted back after 6 h post-injection in mock (PBS) and PR8 infected lungs (3 dpi, 500 ffu). (A) Graphical representation of BM-MSC isolation conditions. MSC (green) represent BM-MSC isolated from bone marrow of healthy animals, MSC MOCK (grey) represent BM-MSC flow sorted from mock-infected (PBS) lungs, delivered 3 days after PBS injection, and MSC PR8 (red) represent BM-MSC flow sorted from 3 days after PR8-infection (500 ffu). **(B-D)** Heatmaps highlighting the (**B**) comparison between MSC and MSC MOCK, **(C)** comparison between MSC and MSC PR8 and **(D)** comparison between MSC MOCK and MSC PR8. In the heatmaps, Z-score Row are presented as red squares for the most upregulated genes and blue squares for most downregulated genes. N=4 biological replicates in MSC and MSC MOCK and N=5 biological replicates for MSC PR8.

PR8 infection (Figure **IV-10**. C) lead to upregulation of vascular endothelial growth factor signaling pathway in BM-MSC (*Nrp2, Pdgfra, Grem1*). When comparing lung-delivered BM-MSC transcriptomic profile in mock or PR8-infected lungs, it is to note that infection cause the upregulation of genes involved in the positive regulation of inflammatory (*Stat5a*) and viral (*Mx1*) responses, as well as up-regulation of pathways promoting fibroblast proliferation, cellular response to interferon beta and gamma, and negative regulation of viral genome replication (Figure **IV-10**. D and Figure **IV-11**). Notably, IL-11 was the only cytokine upregulated in BM-MSC during infection.

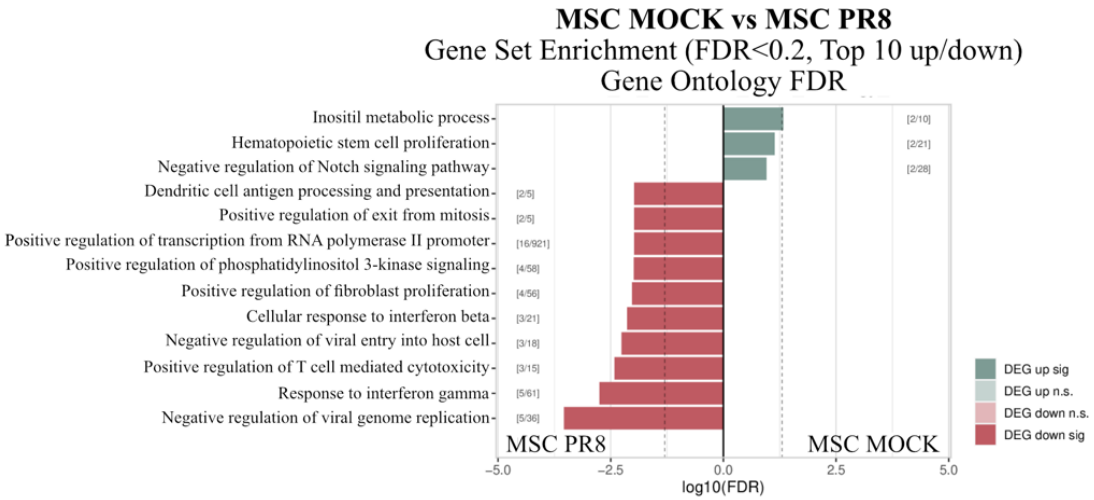

Figure IV-11. Gene set enrichment from flow-sorted IT injected BM-MSC (6 h), isolated from 3 dpi (500 ffu) mock (PBS) or PR8 infected murine lungs. DEG up and down regulated genes after gene set enrichment using KOBAS, with graph representing the top 10 gene sets or pathways enriched from gene ontology database. Dashed line represents a pvalue=0.05. log10 FDR are represented as dark green for significantly upregulated in MSC MOCK, light green for not-significant up-regulation in MSC MOCK, dark red for significantly downregulated in MSC MOCK and light red for not-significant down-regulation in MSC MOCK. N=4 biological replicates for all groups.

Previously described data suggested an important BM-MSC-derived proliferative, anti-apoptotic and anti-viral role towards the infected lung epithelium. However, the extent of BM-MSC contribution to lung (re)generation is still not clear. To test this contribution, a 3D bronchoalveolar lung organoid (BALO) model, established by Vazquez-Armendariz, A.I. *et al*., [33], was used. In the referenced model, BALO are generated by co-culture of FACS-sorted bronchoalveolar stem cells (BASCs, defined as EpCAM^{high} CD24^{low} Sca-1^{+} CC10^{+} SFTPC^{+}) and lung-MSC for 21 days. BALO exhibit branched 3D structures that mimic the cellular composition and organization of the bronchoalveolar compartment. Normally, the culture of BASCs with lung-MSC for 21 days results in a fully developed BALO, where alveolar-like structures can be observed (Figure **IV-12**). To address the contribution of BM-

MSC to BALO generation, the same model was applied using BM-MSC instead of lung-MSC. BM-MSC showed to be far less capable to support cyst development and BALO formation (Figure **IV-12**).

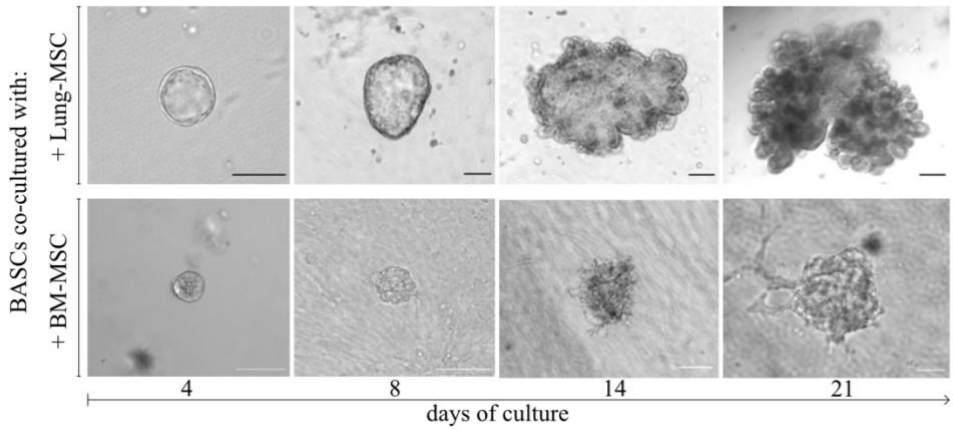

Figure IV-12. BALO development using lung-MSC or BM-MSC. Microscopic images of cysts and developed BALO through time (from day 4 to day 21). Lung-MSC **(upper row)** or naïve BM-MSC **(bottom row)** were co-cultured with BASCs for BALO development. Scale bars represent 180µm. Micrographs are representative of n=6 experiments.

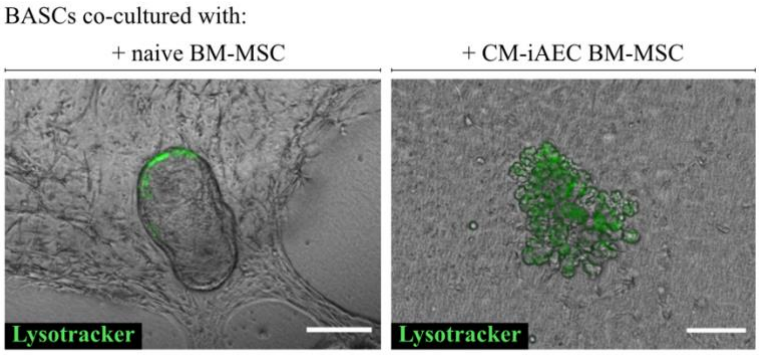

Figure IV-13. BALO development using naïve- or activated-BM-MSC. Microscopic images of BALO (day 21) stained with LysoTracker (green). Naïve BM-MSC **(left image)** or CM-iAEC (conditioned media from 48 hpi iAEC – PR8, MOI 0.1) activated-BM-MSC **(right image)** were co-cultured with BASCs for BALO generation. Scale bars represent 144µm. Micrographs are representative of n=6 experiments.

It was described that BM-MSC are efficiently protecting iAEC from virus-induced damage. It was then next hypothesized that only pre-exposed BM-MSC could act towards protecting iAEC, and thus possibly contribute to lung development (and regeneration). Accordingly, BM-MSC were activated (for 24 h) with conditioned media from 48 h iAEC (PR8, MOI 0.1). Pre-conditioned cells were then used to generate BALO and, strikingly, cell-priming significantly increased BM-MSC capacity to support BALO formation, with higher number of differentiated AEC2, when compared to naïve BM-MSC (Figure **IV-13**). AEC2 were

identified with LysoTracker staining (green) that allows the identification of lamellar bodies present in differentiated AEC2.

To further demonstrate that BM-MSC promote lung regeneration after viral injury, bronchoalveolar lavage (BALF) fluid from day 0 (mock), day 3 (peak of viral load) and day 7 (beginning of regeneration) PR8 infected mice were used as pre-conditioning media for naïve-BM-MSC (Figure **IV-14**). Naïve-BM-MSC, as observed previously, do not contribute to the formation of BALO's complex structure, with LysoTracker staining showing limited AEC2 differentiation (Figure **IV-14**. A) and with a colony formation efficiency of only 1.33 ±0.5 BALO/well and 7 ±0.4 alveolar-like structures per BALO (Figure **IV-14**. B-C). Similar results were obtained with BM-MSC pre-conditioned using BALF day 0 (0.5 ±0.2 BALO/well and 6.33 ±0.2 alveolar-like structures/BALO) and day 7 (0.7 ±0.3 BALO/well and 7 ±0.5 alveolar-like structures/BALO) (Figure **IV-14**. A-C). Notably, BM-MSC activation with CM from 48 h iAEC (4.5 ±0.5 BALO/well and 24.7 ±0.9 alveolar-like structures/BALO) or BALF day 3 (4 ±0.4 BALO/well and 27.7 ±1.6 alveolar-like structures/BALO) created fully differentiated BALO with distinguishable AEC2 differentiation. Therefore, to better mimic BM-MSC response to the lung microenvironment during IAV infection, BALF day 3 was selected to pre-condition BM-MSC in the following assays.

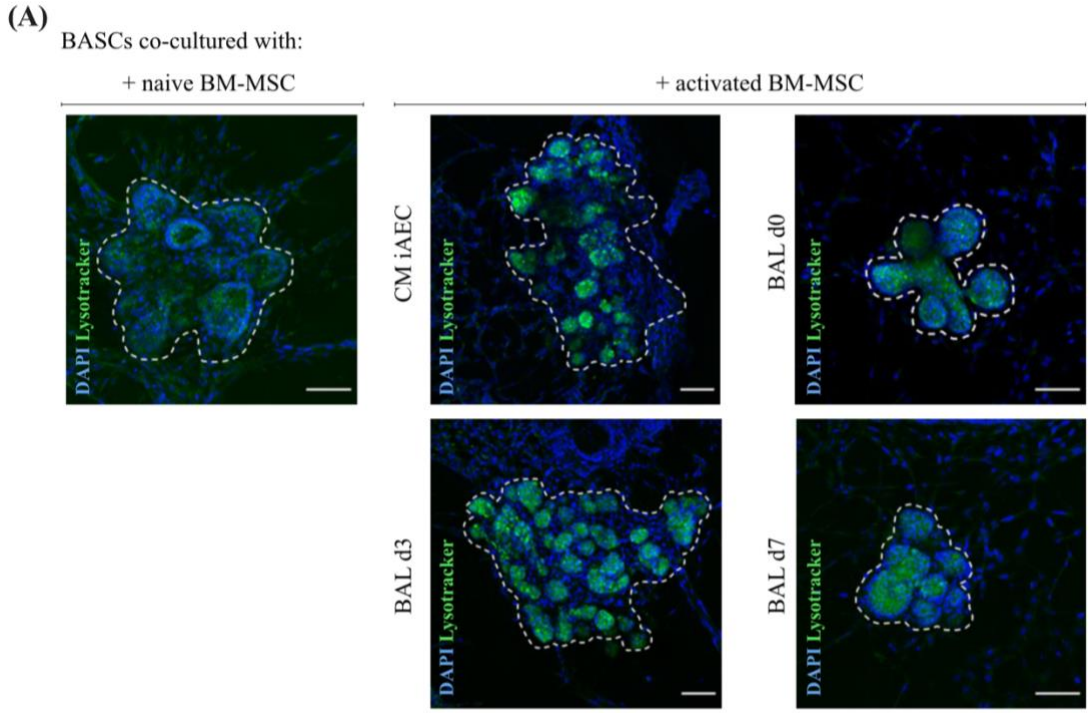

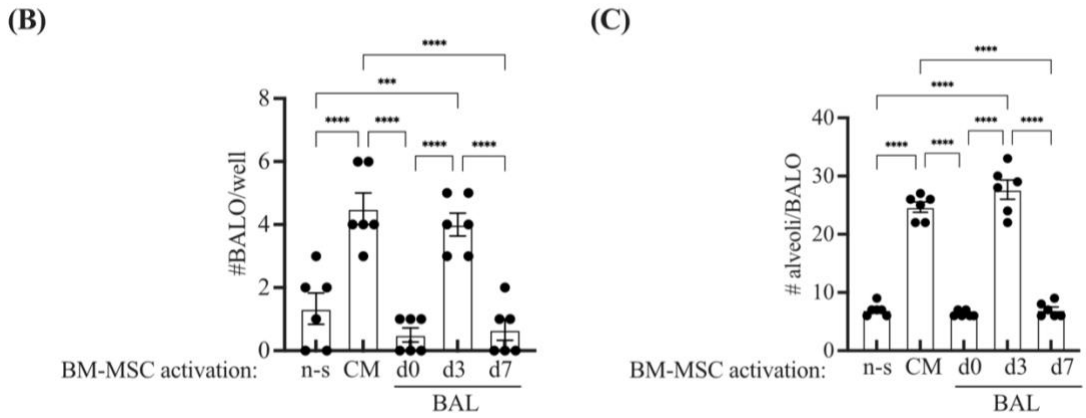

Figure IV-14. BALO development using differently activated BM-MSC. (A) Confocal microscopy images from naïve or differently activated BM-MSC (CM iAEC, conditioned media from iAEC (PR8, 48 h, MOI 0.1) or bronchoalveolar lavage fluid (BALF) from day 0, day 3 and day 7 infected murine lungs (PR8, 500 ffu)). Organoids stained with DAPI (nuclei, blue) and LysoTracker (AEC2, green). Scale bars represent 83µm. **(B)** BALO quantification and **(C)** BALO alveolarization of day 21 BALO using BM-MSC non-stimulated or stimulated with CM from iAEC (PR8, 48 h, MOI 0.1) and BALF from day 0, 3 or 7 infected mice (PR8, 500 ffu) (n=6 biological replicates). Bar charts presented as mean ± SEM and probability determined using one-way ANOVA (*p<0.05, **p<0.01, ***p<0.001, ****p<0.0001).

IV.4. Intra-tracheally delivered BM-MSC show protective effects towards AEC and anti-viral properties *in vivo*

In ARDS studies, BM-MSC have shown to support tissue repair, release anti-inflammatory cytokines, diminish lung endothelial and alveolar epithelial permeability, promote alveolar fluid clearance, and reduce cell apoptosis [122]. These therapeutic effects are thought not only to be exerted by released paracrine factors but also via cell-to-cell contact. Since pre-exposing naïve BM-MSC to infection increased their ability to promote BALO generation and differentiation, BM-MSC stimulated with BALF day 3 (BALFD3) were also used to test their protective capacity towards iAEC *in vitro*. After 24 or 48 hpi, iAEC proliferation, apoptosis, and viral load were assessed by flow cytometry, comparing both naïve- and BALFD3-stimulated BM-MSC (Figure **IV-15**).

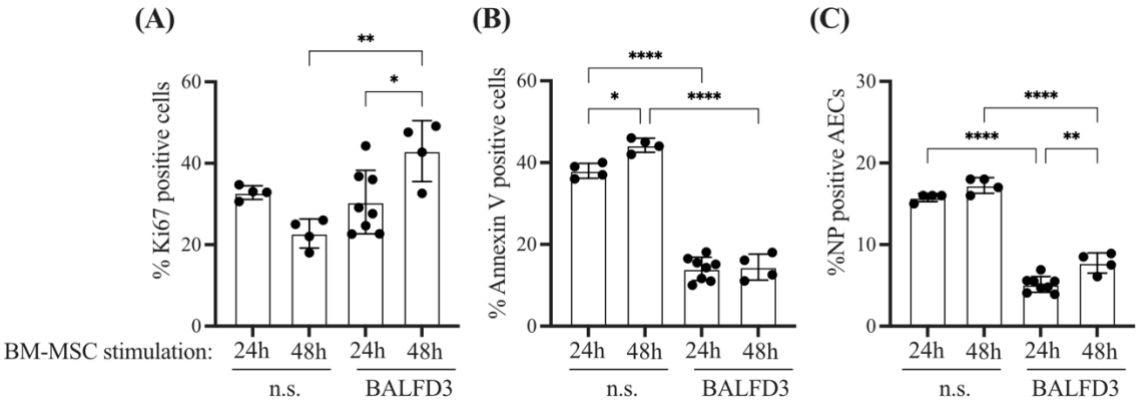

Figure IV-15. BALF day 3 activated BM-MSC have a proliferative, anti-apoptotic and anti-viral effect towards iAEC *in vitro*. (A) Proliferation, **(B)** apoptosis and **(C)** NP expression of infected AEC (MOI 0.1, PR8) co-cultured (24 hpi and 48 hpi) with non-stimulated (n.s.) or BALF day 3 (BALFD3) stimulated BM-MSC. N=4 for n.s. BM-MSC cultures and for 48 hpi BALFD3-BM-MSC cultures and N=8 for BALFD3-BM-MSC cultured for 24 hpi. Bar charts presented as mean ± SEM and probability determined using one-way ANOVA (*p<0.05, **p<0.01, ***p<0.001, ****p<0.0001).

After infection, iAEC cultured with naïve BM-MSC had 32.8% ±0.8 (24 hpi) and 22.7% ±1.7 (48 hpi) of $Ki67^+$ cells. Notably, BALFD3 stimulation significantly increased the percentage of $Ki67^+$ iAEC after 48 hpi (30.48% ±2.7 for 24 hpi and 43% ±3.7 for 48 hpi) (Figure **IV-15**. A). In addition, BALFD3 treatment reduce the percentage of $AnnexinV^+$ iAEC from 38% ±0.9 (naïve BM-MSC) to 14% ±1 after 24 hpi and from 44.2 ±0.8 (naïve BM-MSC) to 14.4% ±1.6 after 48 hpi (Figure **IV-15**. B). The percentage of IAV infected AEC was also decreased when using BALFD3 stimulation, both 24 hpi and 48 hpi, from 15.7% ±0.3 to 5.1% ±0.9 and from 17.3% ±0.5 to 7.8% ±0.6, respectively (Figure **IV-15**. C**)**. Overall, when compared to naïve BM-MSC, BALFD3 stimulation improved BM-MSC anti-apoptotic and anti-viral effects towards iAEC in co-cultures *in vitro*. After demonstrating that murine BM-MSC can increase proliferation and reduce apoptosis and virus detection in iAEC *in vitro*, BM-MSC-mediated protection of the damaged epithelium was tested *in vivo*. For this purpose, WT (C57Bl/6) mice were infected with 500 ffu (PR8) and IT-injected at 3 dpi with PBS, 3T3, BM-MSC or BALFD3-BM-MSC (Figure **IV-16**).

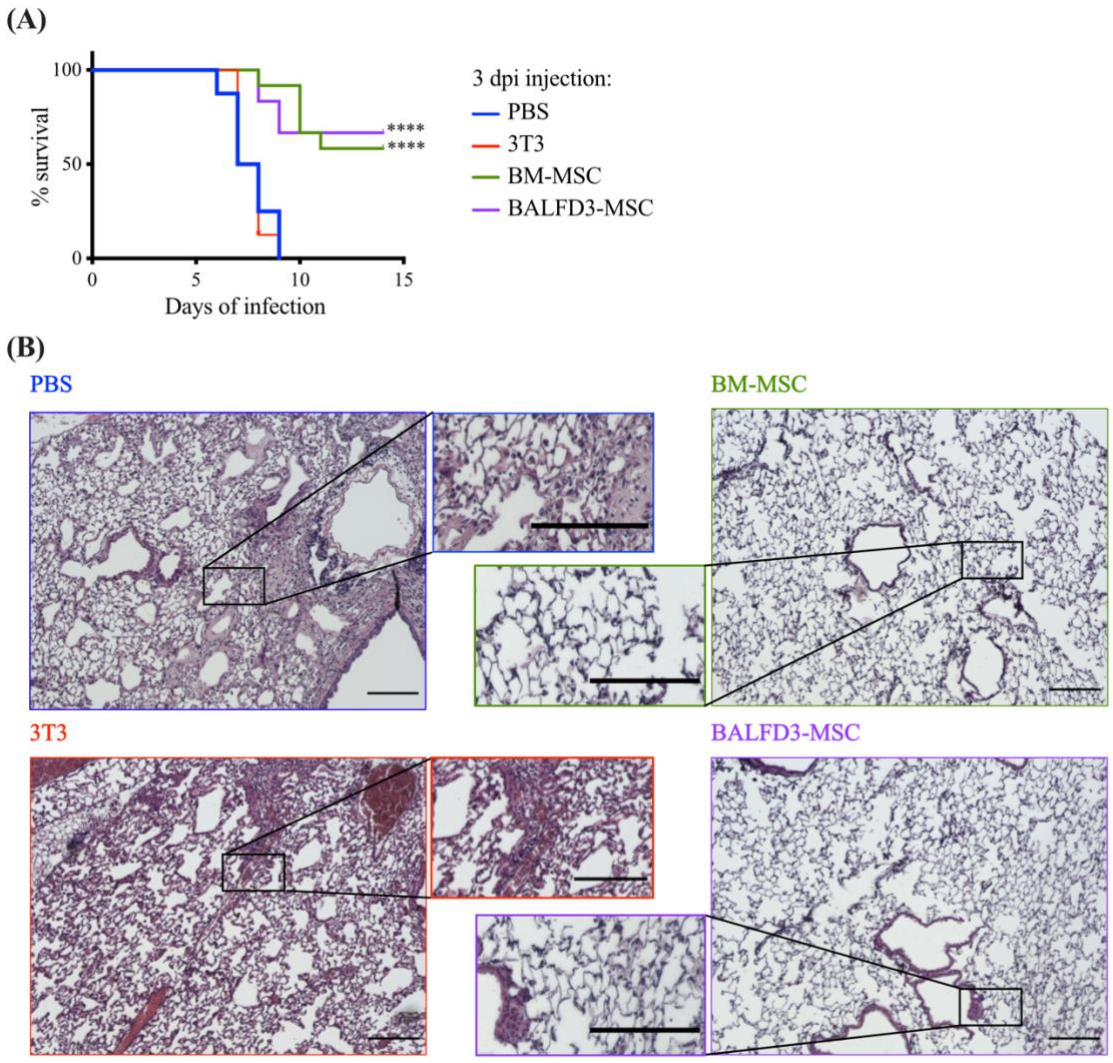

Figure IV-16. ***In vivo*** **experiment of infected (500 ffu, PR8) WT mice, treated at day 3pi with PBS, 3T3, BM-MSC or BALFD3-MSC. (A)** Kaplan-Maier curve of 500 ffu PR8-infected mice treated at day 3 post-infection with PBS (blue), 3T3 (red), naïve BM-MSC (green) or BALF day 3 stimulated-BM-MSC (purple). N=8 biological replicates per group. Probability determined using t-test (*p<0.05, **p<0.01, ***p<0.001, ****p<0.0001). **(B)** Histology of PFA/ paraffin-embedded murine lungs at day 7 post infection (500 ffu, PR8), treated at 3 dpi with PBS, 3T3, BM-MSC or BALFD3 stimulated-BM-MSC. Lung slides were stained with haematoxylin and eosin. Scale bars represent 240µm.

The experimental groups were followed for 14 days, with the PBS or 3T3 instillment being unable to help mice recover from influenza-induced lung damage (0% survival for both settings). On the other hand, BM-MSC (58.3% survival) and BALFD3-BM-MSC (66.7% survival) treatments improved the overall clinical outcome of the infected mice (Figure **IV-16**. A). Seven days post infection, lung paraffin slides were stained with hematoxylin and eosin to histologically evaluate lung injury (Figure **IV-16**. B). When PBS or 3T3 was IT-delivered, the lungs presented severe edema, accumulation of pro-inflammatory cells and damaged alveolar structure. On the other hand, lungs treated with either BM-MSC or BALFD3-BM-MSC showed only subtle histological irregularities, with the lung tissue being overall healthy.

Additionally, the therapeutic effects of IT-BM-MSC were assessed by measuring AEC proliferation, apoptosis, and NP expression by FACS (Figure **IV-17**).

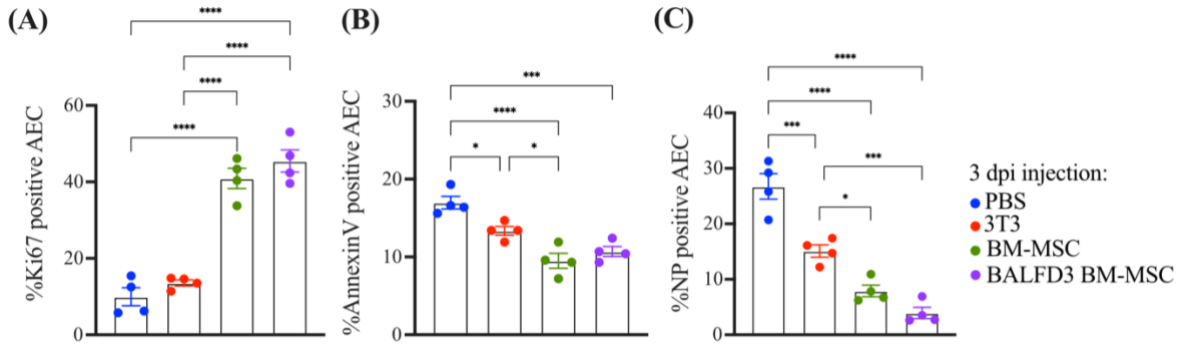

Figure IV-17. Naïve- and BALFD3 BM-MSC protective effects towards iAEC *in vivo*. (A) Proliferation, **(B)** apoptosis and **(C)** NP expression of the iAEC population recovered from 7 dpi (500ffu, PR8) mice treated with PBS (blue), 3T3 (red), BM-MSC (green) or BALFD3-BM-MSC (purple) (n=4 biological replicates). Bar charts presented as mean ± SEM and probability determined using one-way ANOVA (*p<0.05, **p<0.01, ***p<0.001, ****p<0.0001).

AEC isolated from day 7 PR8-infected lungs showed low proliferation capacity after PBS or 3T3 delivery (with 9.97% ±2.4 and 13.6% ±0.8 $Ki67^+$ iAEC, respectively). Contrarily, BM-MSC instillment significantly improved iAEC proliferation, with no significant differences between naïve or BALFD3- BM-MSC (40.9% ±2.6 and 45.5% ±2.9, respectively) (Figure **IV-17**. A). In the same line as previous results, infection-associated AEC apoptosis was proven to be reduced after BM-MSC treatment, with 9.5% ±0.9 of $AnnexinV^+$ iAEC after naïve-BM-MSC delivery and 10.7% ±0.6 of $AnnexinV^+$ iAEC after BALFD3-BM-MSC. Contrarily, PBS and 3T3 instillment showed 17% ±0.8 and 13.3% ±0.65 of $AnnexinV^+$ iAEC, respectively (Figure **IV-17**. B). NP expression in the iAEC population isolated from BM-MSC-treated lungs (7.9% ±1.1 for naïve and 3.9% ±1 for BALFD3) was significantly lower when compared to lungs where PBS (29.8% ±2.3) or 3T3 (15.1% ±1.1) was delivered. Interestingly, there was no significant difference in NP^+ iAEC between naïve BM-MSC and BALFD3-BM-MSC (Figure **IV-17**.C).

Overall, BALFD3 pre-treatment did not affect the outcome of the BM-MSC protective effects. The intra-tracheal application of the naïve BM-MSC in a day 3 infected lung is already a priming condition for these cells, mimicking the BM-MSC *ex vivo* BALFD3-stimulus. Nevertheless, delivered BM-MSC showed to be protective towards the infected and damaged epithelium, possibly supporting lung regeneration after severe injury.

IV.5. Type I interferon pathway plays a key role in BM-MSC anti-viral potential

Viral infection of the alveolar epithelium triggers the activation of intracellular pathways responsible for the production and release of type I and III interferons (IFNα/β and IFNλ) [43]. It has been questioned if and how BM-MSC are able to recognize and respond to virus-induced type I IFN signaling. Activation of BM-MSC by either conditioned media from iAEC or BALFD3 resulted in iAEC increased proliferation and reduced both viral-related apoptosis and NP expression. In order to determine if BM-MSC activation might be linked to high IFN concentrations, ELISA assays were performed to find the concentrations of IFNα, IFNβ and IFNγ. Interestingly, the condition media responsible for BM-MSC activation (CM iAEC and BALF d3) correlates with higher interferons concentrations, with IFNα being the highest cytokine detected (Figure **IV-18**).

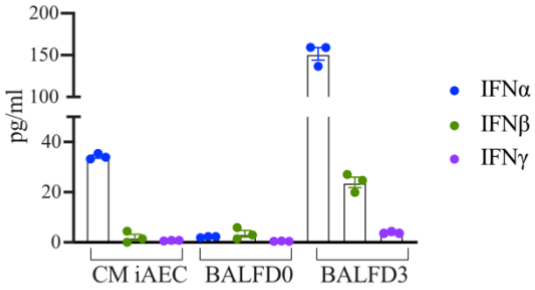

Figure IV-18. IFNs concentrations present in conditioned media used to stimulate BM-MSC. Analysis of mIFNα (blue), mIFNβ (green), and mIFNγ (purple) concentration in conditioned media used to stimulated naïve BM-MSC, performed by ELISA (n=3 biological replicates). CM iAEC, conditioned media from iAEC (MOI 0.1, 48 h, PR8) and BALF, bronchoalveolar lavage fluid from non-infected (BALFD0) or day 3 (BALFD3) infected mice (500ffu, PR8). Bar charts presented as mean ± SEM.

Next, it was hypothesized if type I IFNs alone (IFNα and IFNβ) could be enough to stimulate BM-MSC and mimic the results obtained after BALFD3 stimulation. For this purpose, non-stimulated- and IFNα- or IFNβ-stimulated BM-MSC were co-cultured with iAEC (MOI 0.1, PR8) for 24 h, with iAEC´s proliferation, apoptosis, and NP expression being measured by flow cytometry (Figure **IV-19**). BM-MSC were stimulated with either 150 pg/ml IFNα or 20 pg/ml IFNβ, referring to the concentrations found in BALF from day 3 infected mice (Figure **IV-18**). BM-MSC stimulation with type I interferons significantly increased iAEC proliferation, both with IFNα or IFNβ (83.6% ±1.8 and 75.3% ±2.4 $Ki67^+$ iAEC, respectively) (Figure **IV-19**. A). BM-MSC pre-treatment with IFNs did not alter the iAEC apoptotic levels (38% ±0.9 for non-stimulated BM-MSC, 41.3% ±1.7 for IFNα-BM-MSC and 39.3% ±1.9 for IFNβ-BM-MSC of $AnnexinV^+$ iAEC) (Figure **IV-19**. B). The treatment with IFNs had an impact on the percentage of NP^+ cells, with IFNα-stimulation reducing IAV infection from 15.9% ±0.3 (not-stimulated BM-MSC) to 7.6% ±0.7 (Figure **IV-19**. C).

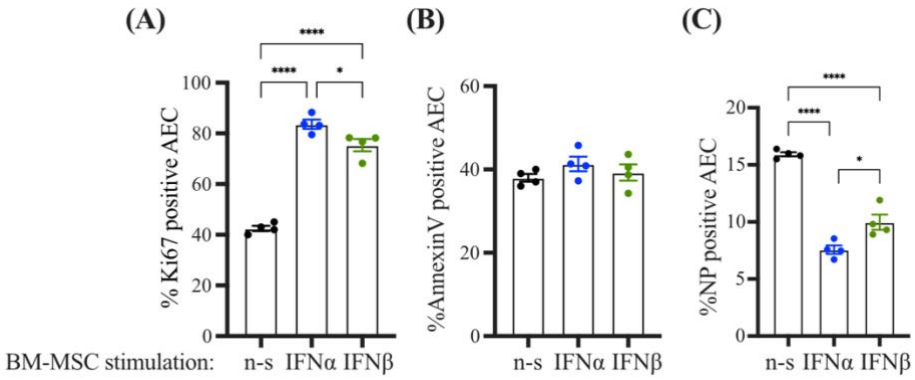

Figure IV-19. Effects of BM-MSC stimulation with mIFNα or mIFNβ on iAEC *in vitro*. (A) Proliferation, **(B)** apoptosis and **(C)** viral presence of iAEC (MOI 0.1, PR8) co-cultured with mIFNα (blue) or mIFNβ (green) stimulated BM-MSC, 24 hpi (n=4 biological replicates). Bar charts presented as mean ± SEM and probability determined using one-way ANOVA (*p<0.05, **p<0.01, ***p<0.001, ****p<0.0001).

Next, to corroborate that BM-MSC activation relies on the recognition of type I interferon via the IFNAR receptor, BM-MSC from IFNAR$^{-/-}$ mice [152] were isolated as previously described and used in co-culture with iAEC (Figure **IV-20**). Impairing the type I interferon signaling in BM-MSC resulted in the loss of the BM-MSC protective effects with decreased iAEC proliferation (from 46% ±2.4 to 32.5% ±1.4 Ki67^{+} iAEC) (Figure **IV-20**. A), and increased iAEC apoptosis and NP expression, from 38.2% ±0.6 to 60.8% ±1 AnnexinV^{+} iAEC and from 17.7% ±1.3 to 37.7% ±2.2 NP^{+} iAEC, respectively (Figure **IV-20**. B and C).

It was validated that the absence of the type I IFN receptor compromises the efficacy of BM-MSC *in vitro*. For *in vivo* confirmation, IFNAR$^{-/-}$ and WT mice were infected with 500 ffu (PR8) and IT-instilled at 3dpi with WT BM-MSC or IFNAR$^{-/-}$ BM-MSC (Figure **IV-21**). The experimental groups were followed for 14 days. Interestingly, mice treated with IFNAR$^{-/-}$ BM-MSC were not able to recover (0% survival for WT or IFNAR$^{-/-}$ mice), whereas IFNAR$^{-/-}$ mice treated with WT BM-MSC could significantly recover from infection-related lung damage, with 100% of mice surviving the infection (Figure **IV-21**. A). Histologically, WT mice that received IFNAR$^{-/-}$ BM-MSC showed severe edema, accumulation of inflammatory cells and damaged alveolar structure while IFNAR$^{-/-}$ mice treated with WT-BM-MSC displayed only subtle lung histological irregularities, with the tissue presenting intact alveolar structure (Figure **IV-21**. B).

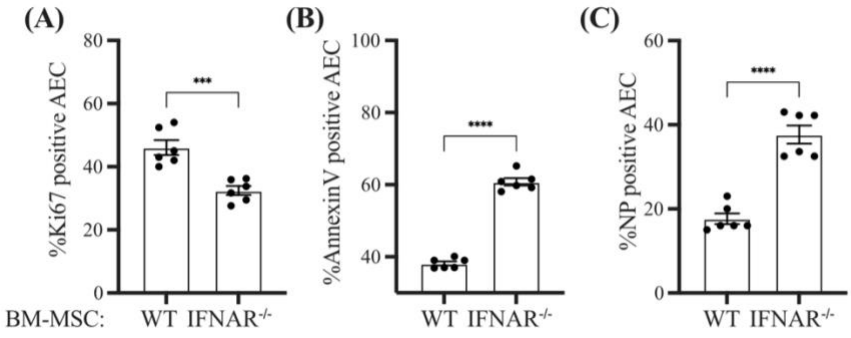

Figure IV-20. BM-MSC protective effects towards iAEC rely on IFN signaling *in vitro*. Proliferation **(A)**, apoptosis **(B)** and viral presence **(C)** of iAEC (MOI 0.1, PR8) co-cultured with either WT or IFNAR$^{-/-}$ BM-MSC 24hpi (n=6 biological replicates). Bar charts presented as mean ± SEM and probability determined using t-test (*p<0.05, **p<0.01, ***p<0.001, ****p<0.0001).

Additionally, the therapeutic effects of the WT or IFNAR$^{-/-}$ IT-delivered BM-MSC were accessed by measuring proliferation, apoptosis, and NP expression in AEC isolated from PR8-infected WT or IFNAR$^{-/-}$ mice 7 dpi (Figure **IV-22**). IFNAR$^{-/-}$ BM-MSC instillment in WT mice resulted in poor outcome and, in concordance, iAEC population showed a lower proliferation rate (14.60% ±1.2 Ki67^{+} iAEC), with high infection-related apoptosis (17.95% ±1 AnnexinV^{+} iAEC) and NP expression (23.65% ±1.5 NP^{+} iAEC) (Figure **IV-22**. A-C). Conversely, WT BM-MSC delivery into infected IFNAR$^{-/-}$ lungs revealed a higher rate of AEC proliferation (28.75% ±0.89 Ki67^{+} iAEC), with decreased apoptosis (13.48% ±1.5 AnnexinV^{+} iAEC) and viral detection (11.55% ±0.4 NP^{+} iAEC) (Figure **IV-22**. A-C).

Overall, the deletion of type I IFN signaling receptor was detrimental for BM-MSC therapeutic properties. Following AEC infection, released IFNs that signal viral-associated damage need to be recognized by BM-MSC in order to activate their response towards protecting iAEC. The use of IFNAR$^{-/-}$ mice did not affect the outcome of mice survival, suggesting that impaired IFNAR on the infected epithelium does not affect BM-MSC ability to recognize and act towards the infection.

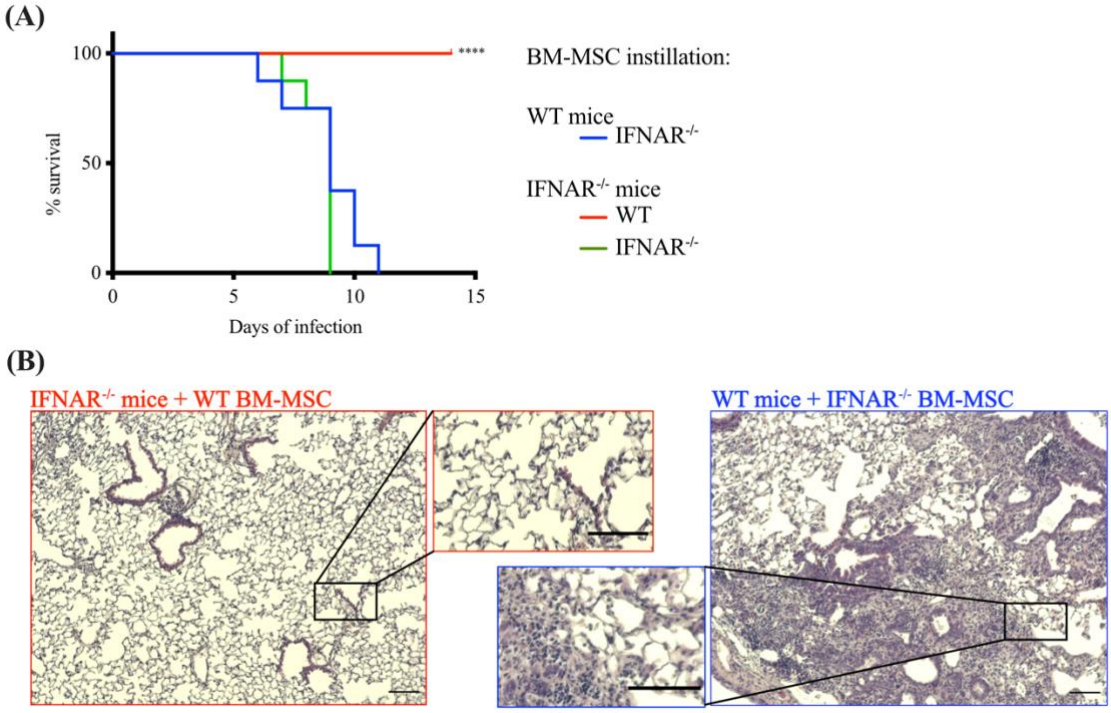

Figure IV-21. *In vivo* experiment of infected (500 ffu, PR8) WT and IFNAR$^{-/-}$ mice, treated at 3 dpi with WT- or IFNAR$^{-/-}$- BM-MSC. (A) Kaplan-Maier curve of 500 ffu PR8 infected WT mice treated at 3 dpi with IFNAR$^{-/-}$ BM-MSC (blue) and IFNAR$^{-/-}$ mice treated at 3 dpi with either WT BM-MSC (red) or IFNAR$^{-/-}$ BM-MSC (green). N=8 biological replicates and probability determined using t-test (*p<0.05, **p<0.01, ***p<0.001, ****p<0.0001). **(B)** Histology of PFA/paraffin-embedded WT or IFNAR$^{-/-}$ mice lungs at day 7 post infection (500 ffu, PR8), treated at 3 dpi with WT or IFNAR$^{-/-}$ BM-MSC. Lung slides were stained with haematoxylin and eosin. Scale bars represent 240µm.

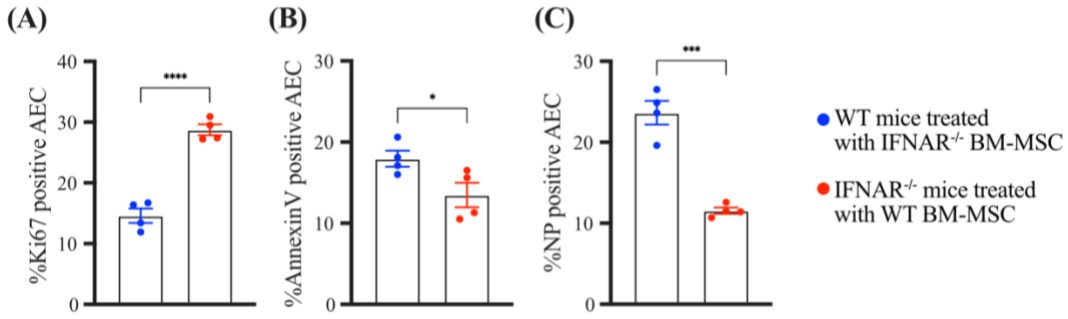

Figure IV-22. WT- and IFNAR$^{-/-}$-BM-MSC protective effects towards *in vivo* infected AEC. (A) Proliferation, **(B)** apoptosis and **(C)** NP expression of the AEC population recovered from 7-day infected WT or IFNAR$^{-/-}$ mice (500ffu, PR8) treated with WT- or IFNAR$^{-/-}$-BM-MSC (N=4 biological replicates). Bar charts presented as mean ± SEM and probability determined using t-test (*p<0.05, **p<0.01, ***p<0.001, ****p<0.0001).

So far, impairing type I IFN signaling has proven to revert the beneficial effects of BM-MSC on the infected epithelium, previously observed in both non-stimulated and BALFD3-stimulated cells. To better understand the degree of viral-associated damage after treatment with WT-, BALFD3-, and IFNAR$^{-/-}$- BM-MSC, an organoid model was used. BALO was

generated by culturing BASC with lung-MSC, as described before [33]. The use of mT/mG reporter mice for cell isolation, together with infection with a reporter IAV-Cre virus, allowed the direct visualization of infected/recovered cells [33]. Microinjection of WT, BALFD3-, or IFNAR$^{-/-}$- BM-MSC inside the BALO airways was performed 1 h after infection. Microscopically, the presence of GFP-marked iAEC showed that BALO infection was successful. After 24 hpi, the level of infection in BALO was analyzed through confocal microscopy and quantified using the macro described in Microscopy (Figure **IV-23**).

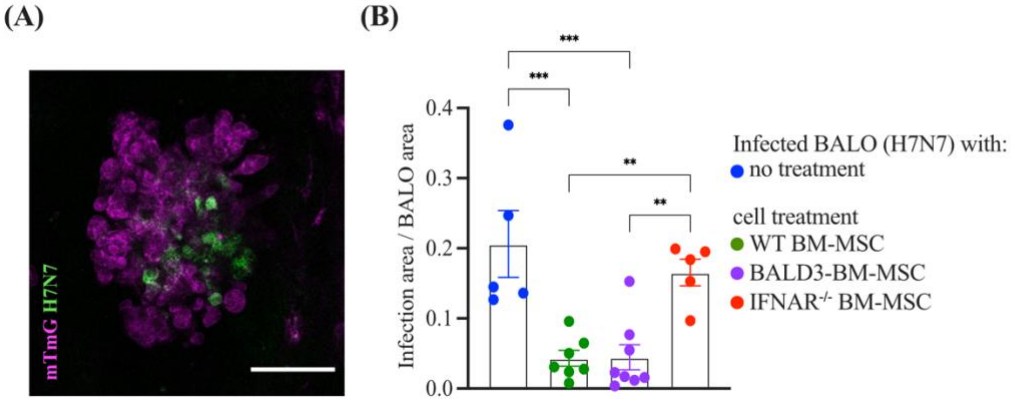

Figure IV-23. Infected BALO (Cre-H7N7) treated with WT-, BALFD3-, or BALFD3-IFNAR$^{-/-}$ BM-MSC. mT/mG BALO (magenta) were infected for 1 h with Cre-H7N7 (green) and fixed after 24 hpi. (A) Confocal image representing a IAV-Cre infected BALO, microinjected with BM-MSC. Scale-bar represent 121µm. **(B)** Infected area ratio, calculated from total BALO area divided by infected area, using data obtained by confocal microscopy. N=5 biological replicates for no treatment, N=7 biological replicates for WT BM-MSC, N=8 biological replicates for BALFD3 BM-MSC and N=5 biological replicates for BALFD3-IFNAR$^{-/-}$ BM-MSC. Bar charts presented as mean ± SEM and probability determined using one-way ANOVA (*p<0.05, **p<0.01, ***p<0.001, ****p<0.0001).

After 24 h of infection and cell injection, the biggest infection areas were detected in IAV-Cre infected BALO that had no cell treatment (0.2 ±0.05 ratio) or were injected with IFNAR$^{-/-}$ BM-MSC (0.17 ±0.02 ratio) (Figure **IV-23**. B), proving the inefficacy of these cells to reduce virus-infected cells in BALO. Microinjecting WT BM-MSC or BALFD3-BM-MSC in infected BALO resulted in a decrease of quantifiable infection-area of 0.04 ±0.01 and 0.04 ±0.02, respectively, suggesting that BM-MSC might play an important role in reducing cell susceptibility to viral infection (Figure **IV-23**. B).

IV.6. Activated BM-MSC release IL-11 and increase AEC resilience via a protective type I IFN/IL-11 signaling loop

In response to PR8 infection, the transcriptomic profile of IT-delivered BM-MSC revealed IL-11 as a highly expressed cytokine (Figure **IV-10**. C). IL-11 is known to be expressed in fibroblasts after TGF-β1 exposure and it is linked to a fibrotic response, with conflicting data on whether it might be pro- or anti-fibrotic [157]–[159]. Although being associated with bacterial pneumonia [160], the IL-11 specific role in viral infection and MSC treatment has not been yet described. To understand the crosstalk between type I IFN pathway and the release of IL-11 in the context of BM-MSC activation, an ELISA assay was performed to investigate if IL-11 is released by WT- or IFNAR$^{-/-}$- BM-MSC after treatment with either BALF, IFNα or IFNβ (Figure **IV-24**). 150 pg/ml of IFNα and 20 pg/ml of IFNβ were used to stimulate BM-MSC, to mimic the concentrations found in BALF from day 3 infected mice (Figure **IV-18**).

While IL-11 was not detectable in non-activated BM-MSC, all the treatments resulted in a high release of the cytokine, with IFNα and IFNβ stimulation inducing the highest response (5220.08 ±198.4 pg/ml and 5320.92 ±191.5 pg/ml, respectively). Interestingly, none of the treatments in IFNAR$^{-/-}$ BM-MSC caused IL-11 detection, hinting a possible direct correlation between type I IFN signalling activation and IL-11 release.

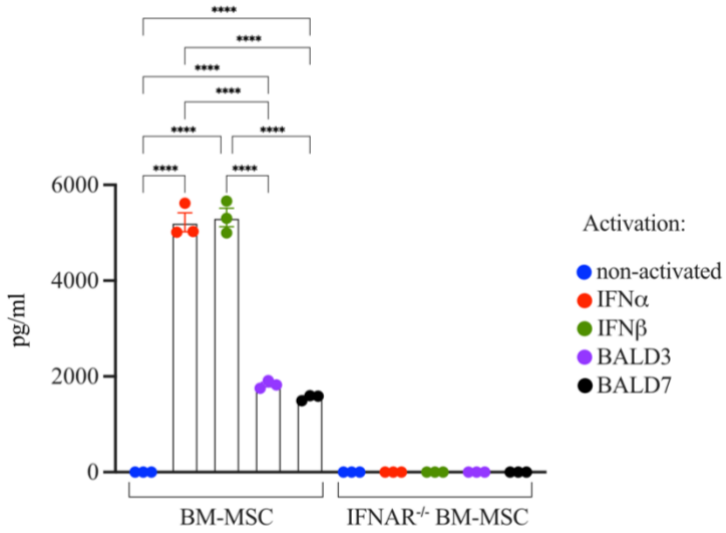

Figure IV-24. IL-11 concentration in stimulated WT- and IFNAR$^{-/-}$ BM-MSC. Analysis of IL-11 concentration (pg/ml) in supernatants after WT- or IFNAR$^{-/-}$- BM-MSC stimulation with IFNα, IFNβ and concentrated BALF from d3 and d7 infected (PR8, 500 ffu) mice. Performed by ELISA (n=3 biological replicates). Bar charts presented as mean ± SEM and probability determined using one-way ANOVA (*p<0.05, **p<0.01, ***p<0.001, ****p<0.0001).

The next line of investigation was to understand if IL-11 alone, without the need of BM-MSC presence, was enough to protect AEC from infection *in vitro*. Therefore, murine lung AEC were isolated, cultured, infected (MOI 0.1, PR8) for 1 h, and treated for 24 hpi with 50 ng/mL of recombinant mouse IL-11 (Figure **IV-25**). As control, un-infected and un-treated (n-t) AEC cultures were used.

IL-11 treatment significantly increased AEC proliferation, with no differences between the presence (39.78% ±3.1 Ki67$^+$ iAEC) or absence (41.47% ±1.6 Ki67$^+$ AEC) of virus (Figure **IV-25**. A). Equally, iAEC apoptosis was reduced with IL-11, with a decrease in the percentage of AnnexinV$^+$ iAEC from 80.7% ±3.6 to 36.9% ±1.7 (Figure **IV-25**. B).

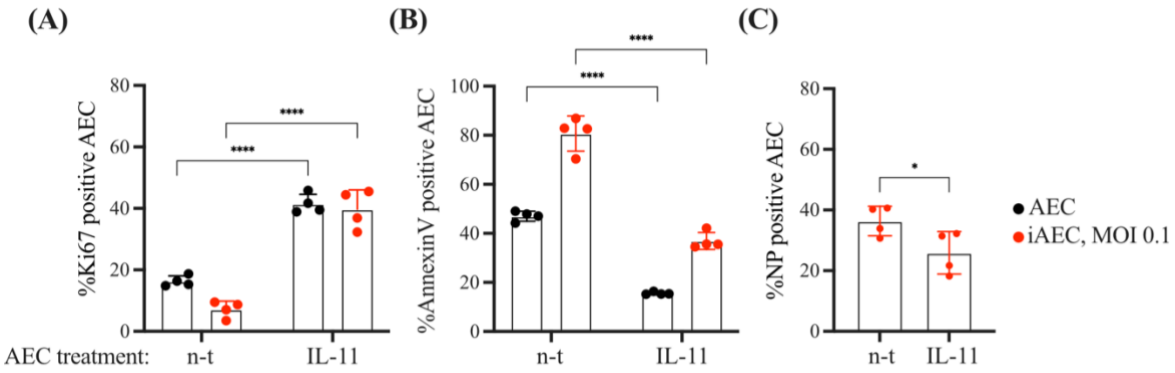

Figure IV-25. Recombinant mIL-11 treatment of *in vitro* iAEC. (A) Proliferation, **(B)** apoptosis and **(C)** NP expression of non-infected (AEC, black dots) and infected (iAEC, red dots, MOI 0.1, PR8) AEC treated with 50 ng/mL of mIL-11 for 24 hpi (n=4 biological replicates). n-t, no treatment. Bar charts presented as mean ± SEM and probability determined using two-way ANOVA (*p<0.05, **p<0.01, ***p<0.001, ****p<0.0001).

Finally, data suggests that IL-11 might also exhibit an anti-viral effect, with NP$^+$ iAEC decreasing from 36.3% ±2.4 to 25.87% ±3.5 after treatment (Figure **IV-25**. C). A foci formation assay was performed from the supernatants of cultures treated with 50 ng/mL and 100 ng/mL of IL-11, with possible IL-11 dose-dependent responses in viral presence between sample preparations (Figure **IV-26**).

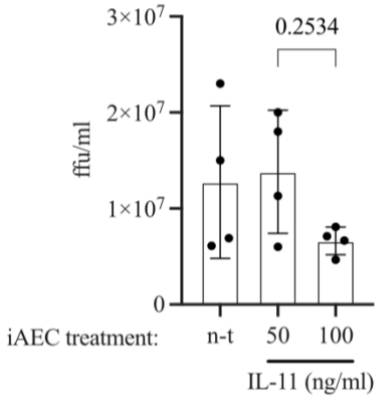

Figure IV-26. Foci assay from IL-11 treated iAEC. Foci assay on the supernatants of non-treated (n-t) and 24 h treated (50 ng/ml and 100 ng/ml) iAEC (MOI 0.1, PR8) (n=4 biological replicates). Bar charts presented as mean ± SD and probability determined using two-way ANOVA.

In summary, these results suggest that IL-11 increases iAEC proliferation to values comparable to the ones obtained when co-culturing iAEC with BM-MSC (Figure **IV-6**. A, 42.5 ±1% Ki67$^+$ iAEC) or with BALFD3-BM-MSC (Figure **IV-15**. A, 30.5 ±2.8% Ki67$^+$ iAEC). In line with these data, IL-11 treatment reproduces the anti-apoptotic effects towards

iAEC observed with BM-MSC (38± 0.9% AnnexinV$^+$ iAEC for WT – Figure **IV-6**. B – and 14 ±1% AnnexinV$^+$ iAEC for BALFD3-stimulated cells – Figure **IV-15**. B). IL-11 seems to exhibit a dose-dependent anti-viral effect (Figure **IV-26**, p=0.25).

Since IL-11 has an impact in iAEC proliferation and apoptosis, it was hypothesized that IL-11 secretion by BM-MSC might play an important role in the communication between these cells and the infected lung epithelium. To further test if the loss of IL-11 production/release would alter BM-MSC protective effects, an IL-11 knockdown BM-MSC was produced by transfection with Silencer® Select (siRNA) IL-11.

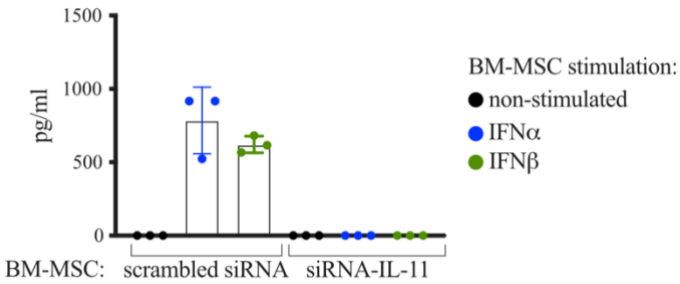

Figure IV-27. Silencing IL-11 in BM-MSC. Analysis of IL-11 concentration (pg/mL) in supernatants from scrambled or siIL-11 treated BM-MSC, not stimulated (black dots) and stimulated with mIFNα (blue) or mIFNβ (green), performed by ELISA (n=3 biological replicates). Bar charts presented as mean ± SEM.

IL-11 silencing efficacy was tested by measuring IL-11 concentration (using an ELISA assay) after type I IFNs (IFNα, 150 pg/mL and IFNβ, 20 pg/mL) stimulation (Figure **IV-27**). The undetectable concentration of IL-11 after siRNA transfection proved that the approach worked as expected, with no cytokine release, even after IFNα and IFNβ stimulation.

After obtaining siRNA-IL-11 BM-MSC, it was sought to determine what effects might BM-MSC have after IL-11 knockdown *in vivo*. Following the same procedures as previously described, siRNA-IL-11 BM-MSC (or scrambled siRNA control-treated BM-MSC) were IT-injected 3 dpi in 500 ffu infected (PR8) WT mice (Figure **IV-28**).

The outcome of the infected and treated mice was followed for 14 days. Mice that received siRNA-IL-11 BM-MSC presented a lower survival rate (33% survival) when compared with mice instilled with scrambled siRNA BM-MSC (66% survival) (Figure **IV-28**. A). Histologically, cell-treatment with IL-11 knockdown BM-MSC revealed discrete edema, with local accumulation of inflammatory cells, while control treatment showed minor histological changes (Figure **IV-28**. B), with normal alveolar structure. Therefore, knockdown of IL-11 in BM-MSC may represent crucial element for the communication between BM-MSC and the infected lung epithelium.

To access the alveolar damage arisen from IL-11 silencing in BM-MSC, the AEC population from infected and treated mice (as previously described) was isolated 7 dpi (Figure **IV-29**). IL-11 impairment in BM-MSC caused a decrease in iAEC proliferation (from 33.24% ±2 to 43.47% ±3.1 $Ki67^+$ iAEC, Figure **IV-29**. A).

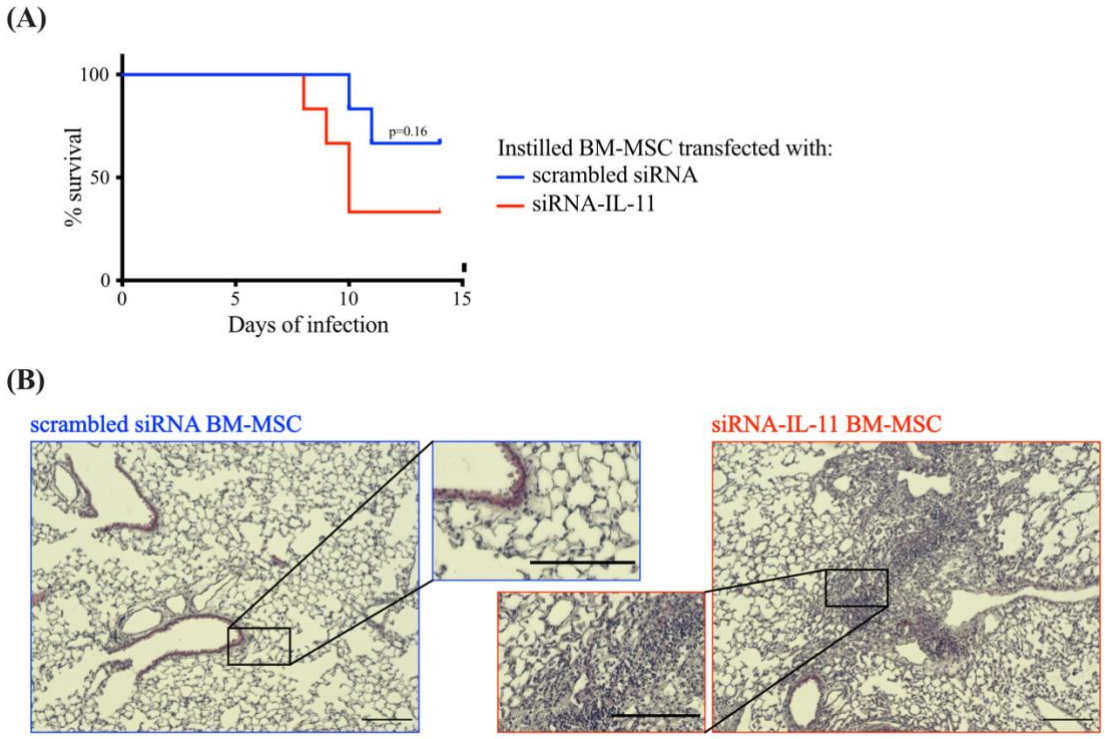

Figure IV-28. ***In vivo*** **experiment of infected (500 ffu, PR8) WT mice, treated at 3 dpi with scrambled siRNA BM-MSC or siRNA-IL-11 BM-MSC. (A)** Kaplan-Maier curve of 500 ffu PR8 infected WT mice treated at 3 dpi with scrambled siRNA BM-MSC (blue) or siRNA-IL-11 BM-MSC (red). N=6 biological replicates per group, points presented as mean ± SEM and probability determined using t-test (not significant, p=0.16). **(B)** Histology of PFA/paraffin-embedded WT lungs at day 7 post infection (500 ffu, PR8), treated at 3 dpi with scrambled siRNA BM-MSC (blue) or siRNA-IL-11 BM-MSC (red). Lung slides were stained with haematoxylin and eosin. Scale bars represent 240 µm.

In addition, siRNA-IL-11 BM-MSC were less able to protect iAEC from viral-induced apoptosis, with an increase of $AnnexinV^+$ iAEC from 9.79% ±2.79 to 14.91% ±3.4 (Figure **IV-29**. B). Nonetheless, after siIL-11 BM-MSC instillment, NP^+ iAEC show comparable values to scrambled siRNA BM-MSC (8.39% ±3.7 and 7.35% ±1.7, respectively, Figure **IV-29**. C). Taken together, these results indicate that knocking down IL-11 in BM-MSC negatively affects AEC proliferation and anti-apoptotic effects towards infected AEC, playing a limited role in viral protection.

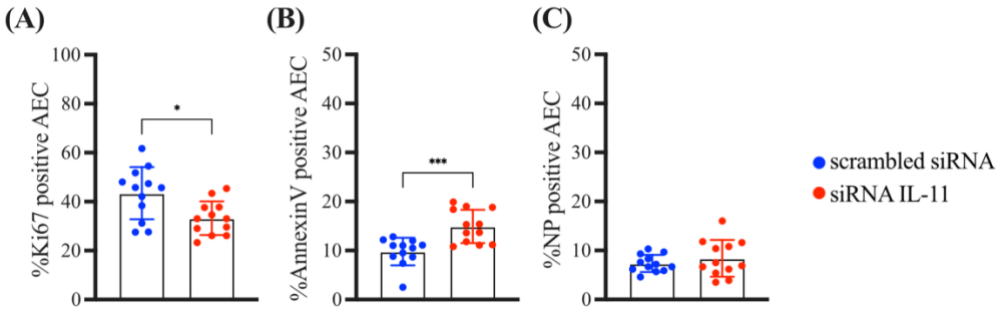

Figure IV-29. Scrambled siRNA control- and siIL-11 BM-MSC effects towards infected AEC *in vivo*. (A) Proliferation, **(B)** apoptosis and **(C)** NP expression of the iAEC population recovered from 7-day infected mice (500 ffu, PR8) treated with scrambled siRNA control-BM-MSC (blue) or siIL-11 BM-MSC (red) (n=12 biological replicates). Bar charts presented as mean ± SEM and probability determined using one-way ANOVA (*p<0.05, **p<0.01, ***p<0.001, ****p<0.0001).

The impact on IL-11 silencing in BM-MSC was also accessed in infected BALO. The quantification of viral-associated damaged of lung epithelium after cell treatment was determined using BALO obtained from mT/mG reporter mice and infected with IAV-Cre at day 21. Microinjection of scrambled siRNA or siRNA-IL-11 BM-MSC into BALO airways was performed 1 h after infection. Microscopically, the presence of GFP^+ AEC showed that BALO infection was successful. After 24 hpi, the level of infection in BALO was analyzed through confocal microscopy and quantified using the macro described in Microscopy (Figure **IV-30**).

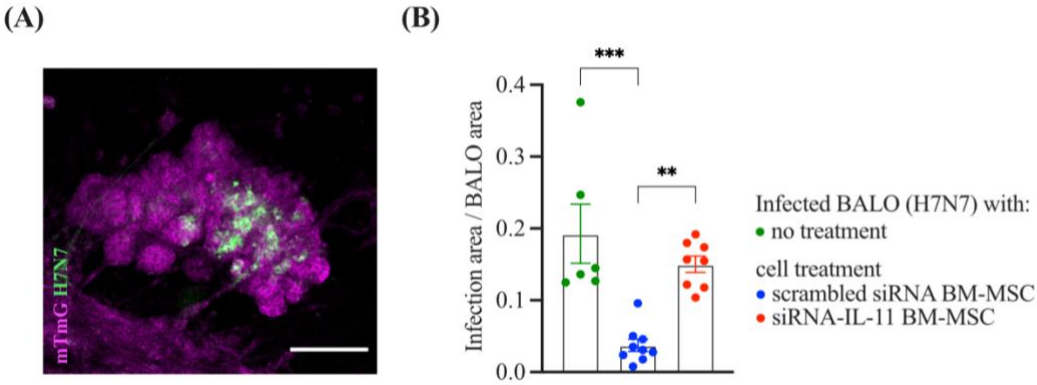

Figure IV-30. Infected BALO (Cre-H7N7) treated with scrambled- or si-IL11 BM-MSC. mT/mG BALO (magenta) were infected for 1 h with Cre-H7N7 (green) and fixed after 24 hpi. (A) Confocal image representing a H7N7-infected BALO, microinjected with siRNA IL-11 BM-MSC. Scale-bar represent 121µm. **(B)** Infected area ratio, calculated from total BALO area divided by infected area, using data obtained by confocal microscopy. BALO was infected, and not-treated (N=6 biological replicates) or injected with scrambled- (N=9 biological replicates) or siRNA IL-11 BM-MSC (N=8 biological replicates) and fixed after 24 h. Bar charts presented as mean ± SEM and probability determined using one-way ANOVA (*p<0.05, **p<0.01, ***p<0.001, ****p<0.0001).

Following IAV-Cre infection, microinjection of siRNA-IL-11 BM-MSC showed an infection area ratio similar to not treated BALO (0.15±0.01 and 0.19 ±0.04 ratio, respectively) (Figure **IV-30**. B). Treatment with scrambled siRNA BM-MSC reduced the infected BALO area (0.04±0.01 ratio), suggesting an active role of IL-11 in protecting epithelial cells from viral-associated damage. These data suggest that IL-11 knockdown negatively affects BM-MSC's epithelial-protective effects during viral injury, in all the models tested.

Altogether, after influenza infection targets the lung epithelium, the IFNs concentration in the alveoli drastically increases as an infection-associated response. Therapeutic intra-tracheal delivery of BM-MSC can improve the infection-associated epithelial damage. The shown data proves that the molecular response of BM-MSC is dependent on type I IFN signaling activation, with consequent release of IL-11. The loss of either type I IFN signaling activation or IL-11 release worsens the proliferative, anti-apoptotic and anti-viral effects of these cells towards the infected epithelium, highlighting the use of this signalling axis as a target for the development of future MSC therapies.

V. Discussion

MSC show promising therapeutic potential, but it is unclear how MSC identify injury during viral lung infections and how MSC react to protect the infected epithelium. This thesis sought to understand how intra-tracheally delivered BM-MSC can sense injury during influenza infection and how these cells can be primed to enhance epithelial regeneration. It was shown with an *in vitro* co-culture model that BM-MSC can protect PR8-infected AEC, with those effects being recapitulated *in vivo*, improving mice survival and remarkably reducing lung damage. The release of viral-associated factors by the infected epithelium, markedly type I IFN signalling molecules (IFNα and IFNβ), successfully activated BM-MSC, with IFNAR receptor impairment (and thus, type I interferon signalling) resulting in loss of BM-MSC anti-viral and anti-apoptotic properties. The communication between intra-tracheally delivered BM-MSC and the infected AEC was also shown to be dependent on the release of IL-11 by BM-MSC, significantly contributing to increase AEC resilience and strengthening the hypothesis of using type I IFN/IL-11 signalling axis as a target for the development of future MSC therapies.

Although the mesenchyme plays an important role in lung regeneration, not a lot in understood about the resident lung-MSC population [161]. Previous studies determine that lung-MSC can support proliferation and differentiation of airway and alveolar epithelial stem cells *in vitro* [162] and their therapeutic administration has been shown to alleviate emphysema and increase survival *in vivo* [163]. However, these studies do not fully investigate how and to which extent lung-MSC sense viral infections. This thesis was able to prove, thought RNA-bulk sequencing, that lung-MSC isolated from day 3 infected murine lungs can recognize and respond towards influenza infection by upregulation of genes involved in type I and II interferon signalling. This response also involved a notable increase in anti-viral activity, together with upregulation of stem cell self-renewal, proliferation, and pluripotency pathways. Notably, iAEC were protected from the consequences of viral infection when co-cultured with lung-MSC, with iAEC proliferation increasing, while apoptosis and virus-infected cells showed a significant reduction.

The lung mesenchyme undoubtedly presents itself protective against iAEC; however, it does not represent a viable approach for ARDS patients due to their low availability and expandability. To this regard, BM-MSC have been extensively proposed as a cell-based therapy [164]–[166]. Some of the challenges that BM-MSC present as a viable therapeutic

approach have to do with inherent factors like cell heterogeneity, potency, biodistribution and limited comprehension of mode of action [167]. Though being isolated from mice with the same genetic background, sex, similar age, and husbandry, the inherent heterogeneity of the population is to be noted. To overcome discrepancies, before and during manipulation, primary isolated murine BM-MSC ($CD45^-$ $Ter119^-$ $CD31^-$ $PDGFR\alpha^+$ $Sca\text{-}1^+$) were characterized routinely via flow cytometry or *in vitro* differentiation to show that they were able to retain their stem cell potential, according to ISCT criteria. Nevertheless, it is also known that donors age and sex can significantly affect the cell phenotypes, and it is highly recommended that BM-MSC trophic factors are extensively evaluated before clinical use [168]. To switch from primary cells to cell lines could be considered a more reliable method for population homogeneity but cell lines often do not mimic the native cell population in culture and are more prone to abnormal genetic modifications and contamination [169].

To date, no mechanism of direct interaction between BM-MSC and the alveolar epithelium have been proposed in virus-induced ARDS. Previous work focused on BM-MSC and A549 cells co-cultures revealed that after LPS stimulation, BM-MSC presence increased viability and decrease apoptosis in AEC via TLR4 activation [170]. The presented results suggest that IV-iAEC co-cultured with BM-MSC can tolerate viral-induced damage, with higher percentage of proliferating cells and reduced apoptotic levels, as well as lower viral detection when compared to controls. Usually, co-culture methods rely on the secretion of paracrine factors, dismissing the importance of direct cell-to-cell communication. This thesis focused on applying diverse methods to study cell interactions, like a state-of-the-art lung organoid model. The generation of the 3D lung structures was used as a technique to study the effects of BM-MSC on AEC regenerative capacities after organoid viral injury. Although cell differentiation capacity of BALO using BM-MSC was lower, when compared to resident lung-MSC [33], pre-conditioning of BM-MSC with soluble factors from iAEC or from BALF (from day 3 infected mice) significantly enhanced BALO growth and differentiation. Although BM-MSC have been cultured in 3D spheroid models to study bone, cartilage, heart, liver and kidney regeneration [171], there are currently no studies suggesting that activated BM-MSC, with *in vivo*-derived cytokines, contribute to lung development/repair.

Besides *in vitro* or *ex vivo* scenarios, this thesis also adds *in vivo* murine infection models to test the proposed hypothesis. Here, BM-MSC were delivered as a localized therapy via intra-tracheal injection. Systemically delivery is the most use route of administration of BM-MSC in clinical trials, however, intravenous injection limits MSC usage and has inherent challenges such as cell entrapment in the pulmonary vascular bed [172]. Still, although the cells might

not reach the desired inflammation location, BM-MSC are able to sense inflammatory environments and release soluble mediators [173]. In contrast, local administration allows direct cell-to-cell communication [174] and transfer of MSC cellular components to lung epithelial cells [175], or extracellular vesicles to macrophages [146]. Upon contact with lung infection, intra-tracheally delivered BM-MSC, recovered by FACS, showed an "activated-state", expressing stem cell markers (*Sox9* and *Ndrg1*) and genes related with the positive regulation of inflammatory and viral responses such as *Oasl1, Oasl2, Stat5, Isg15, Ifitm3, Mx1, Irf7* and *Trim11*. The different expression profiles, together with the increased mice survival and healthier lung histology, indicate a targeted response of BM-MSC towards the infected epithelium, suggesting their potential use for the amelioration of ARDS symptoms. While several investigations report the beneficial effects of MSC, most of them are either focused on the secreted molecules/vesicles or on the interaction between the injected cells and the immune system. This work is focused on the local interaction between the instilled BM-MSC and the lung infected epithelium. To this regard, FACS isolated non-infected AEC significantly changed their transcriptomic profile after contact with the IT-injected cells by upregulating *Xist* that promotes stem cell growth and gatekeeps epithelial homeostasis [176]. Concordantly, co-culturing non-infected AEC with BM-MSC significantly reduced AEC apoptosis, suggesting there are important signals being released by BM-MSC, even without a viral infection.

The presented data shows, for the first time, BM-MSC and AEC recovery after therapeutic intra-tracheal cell administration. Bulk-RNA sequencing of recovered AEC show that interferon-related genes were upregulated after infection. Type I IFNs have been shown to be important for host defence against viruses, therefore, high levels of IFN-related genes expression following IAV infection are expected. More specifically, IFNα and IFNβ are known to induce anti-viral responses via IFNAR receptor signalling axis [177]. In fact, our data showed that BM-MSC activation correlates with high IFNs concentration, present in BALFD3, and the use of IFNα and IFNβ as stimulating agents for BM-MSC resulted in more proliferative and viral infection-protected iAEC, with IFNα playing a more determinant role. More recently, type III IFNs have also been shown to present important anti-viral effects, with IFNλ being the prevalent cytokine induced by IAV infection in the upper respiratory tract [178]. Work done by Jewell N. *et al*. contradicted the dependency of murine IFNλ production via IFNAR, with the same level of type III IFN induction shown in both WT and IFNAR$^{-/-}$ mice [179]. In the same line, the work presented in this thesis shows that impaired IFNAR

function does not affect the lung epithelium (as a response to the viral infection), but it is essential for BM-MSC responsiveness and activation of protective pathways.

Bulk-RNA sequencing of IT-delivered BM-MSC highlighted the role of IL-11. Intriguingly, IL-11 has been described as both anti and pro-inflammatory, with reports proving both scenarios [180]. It is thought that the duality of IL-11 is linked to the cell type affected as well as to the challenge affecting it. In liver inflammation, it was described that epithelial and polarized cells were harmed when exposed to IL-11, while stromal cells became more active and resistant [181]. On the contrary, in a cardiac injury zebra-fish model, IL-11 signalling in endothelial cells limits tissue scarring and promotes cardiomyocyte repopulation, revealing a new possible target for regenerative therapies [182]. Accordingly, in this work, upon activation, BM-MSC can successfully communicate with iAEC by releasing IL-11, increasing iAEC resilience by keeping this cell population proliferative and thus less affected by virus-induced apoptosis. This strengthens the hypothesis of using type I IFN/IL-11 signalling axis as a target for the development of MSC therapies. Regarding the effects on MSC, there are reports suggesting that IL-11 promotes cell proliferation, migration, and reduced apoptosis in AD-MSC (through STAT3 signalling) [183] and it is expressed by BM-MSC upon poly(I:C) treatment [184] and pro-inflammatory cytokine priming [185]. So far, it is known that IL-11 activates STAT-1 and STAT-3, considered important signal mediators of type I IFN [186], [187]. High IL-11 expression has also been reported in viral airway disorders (caused by syncytial virus, rhinovirus, and parainfluenza) and chronic inflammatory airways diseases [188]. Taking all the conflicting data together, the IL-11 role in pulmonary diseases is not certain, leaving open questions regarding its biology and function in the lung. In the presented investigation, both *in vitro* and *in vivo*, silencing IL-11 in BM-MSC has proven to counteract the positive effects of these cells with reduced proliferation and increased apoptosis of infected AEC. Nevertheless, IL-11 anti-viral effects are likely dose dependent, with a consequent increase in iAEC resilience – their proliferative and apoptotic levels upon infection are similar to the ones without infection, suggesting a promising approach for future clinical ARDS scenarios. The presented work also addresses the gap in IT-delivered BM-MSC in murine influenza models, focusing on cell-to-cell contact between the therapeutic cells and the infected epithelium. Altogether, it is here described for the first time that pre-conditioning of BM-MSC with signals from infected lungs can reprogram them to act towards lung (re)generation. It is also noted that the activation of these cells is highly dependent on type I IFN signalling, with consequent release of IL-11. However, this crosstalk has only been studied in a murine model of H1N1 infection. When translating these findings to a clinical

scenario, allogenic BM-MSC could be pre-treated with patient-derived BALF (as an activation method) and be used as a localized cell treatment for me amelioration of symptoms. In the future, this investigation will be followed by human cell experiments, validating the use of type I IFN/IL-11 signalling axis as a therapeutic target.

Meanwhile, MSC are proposed to be effective against a wide range of viruses, including severe acute respiratory syndrome-coronavirus-2 (SARS-CoV-2). In 2021, over 70 clinical trials using MSC as a treatment for corona virus disease 2019 (COVID-19) have been reported, with the major sources being UC, BM, and AD [189]. Despite limited knowledge, MSC have been verified to be overall safe and contribute to significant decrease inflammatory cytokines, restore lymphocyte count after transplantation, improve general functional outcomes (lung CT) and reduce the recovery time of COVID-19 [190]–[193]. Understanding the molecular mechanisms behind the beneficial properties of BM-MSC is a necessary investigation for the future of these cell therapies in both influenza and SARS-CoV-2 infections. The proposed type I IFN/IL-11 axis between iAEC and BM-MSC represents a putative therapy against ARDS.

VI. Summary

Mesenchymal stem cells (MSC) show promising therapeutic potential in different forms of acute lung injury. However, it is not clear how MSC sense injury during viral lung infections. The aim of this study was to understand how the anti-viral and tissue-protective effects of bone marrow derived-MSC (BM-MSC) are mediated and can be applied in the context of influenza-virus (IV) infection. Using IV-infected alveolar epithelial cells (iAEC)/MSC co-culture systems together with the bronchoalveolar lung organoid (BALO) model, it was possible to compare the extent of epithelial cell survival, proliferation and differentiation supported by either lung resident MSC (lung-MSC) or BM-MSC. Strikingly, pre-conditioning with soluble factors derived from iAEC or from bronchoalveolar lavage fluid of infected animals significantly enhanced the capacity of BM-MSC to drive alveolarization in BALO. Despite lower cell differentiation capacity within BALO when BM-MSC were used, compared to lung-MSC, both cell types displayed similar anti-viral, pro-proliferative and anti-apoptotic effects when in co-culture with iAEC. BM-MSC protective properties and transcriptional changes were also evaluated *in vivo* by intra-tracheal (IT) cell application after 3 days of IV-infection in wild-type (WT) mice. The presence of BM-MSC led to the reduction of viral load and infection-associated AEC apoptosis, while significantly improving mice survival. Bulk-RNA sequencing of IT-delivered-BM-MSC flow sorted back from infected or mock-infected lungs revealed that interferon-related genes and the cytokine interleukin (IL)-11 were upregulated in iAEC and BM-MSC, respectively. Notably, data acquired from IFNAR$^{-/-}$ IV-infected mice revealed that the activation of type I interferon (IFN) signaling is essential for BM-MSC's anti-viral and anti-apoptotic effects. As a response to this activation, IL-11 release by BM-MSC was proven to significantly enhance iAEC resilience. In conclusion, the type I IFN/IL-11 signaling axis (Figure **VI-1**) could represent a promising target for the development of human MSC-based therapies.

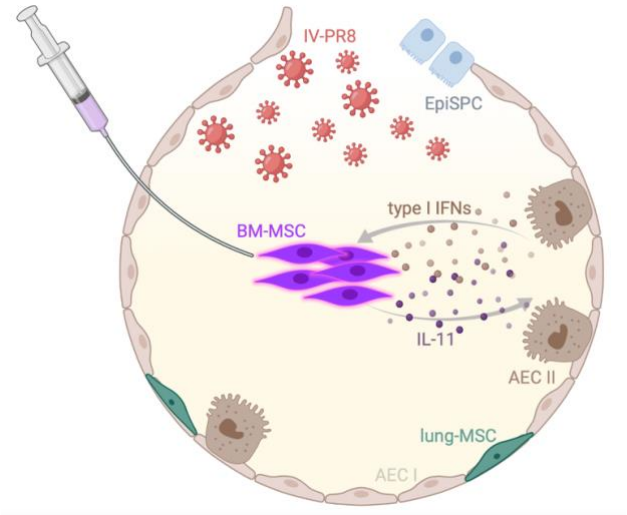

Figure VI-1. Schematic representation of type I IFN (iAEC) / IL-11 (BM-MSC) signaling axis. IT-applied BM-MSC (3 dpi, 500 ffu, IV-PR8) are activated with type I IFNs, released by iAEC. After activation, BM-MSC secrete IL-11 that ultimately improves iAEC resilience. IV, influenza virus; EpiSPC, epithelial progenitor cells; BM-MSC, bone marrow derived mesenchymal stem cells; IFNs, interferons; AEC, alveolar epithelial cells. Created using BioRender.

VII. Zusammenfassung

Bei der Entwicklung von Therapiemöglichkeiten für das akute Lungenversagen kommt mesenchymalen Stammzellen (MSC) aus dem Lungengewebe (lung-MSC) oder Knochenmark (BM-MSC) eine besondere Bedeutung zu. MSC zeigen ein vielversprechendes therapeutisches Potenzial. Der genaue Wirkmechanismus, d.h. wie MSC die lokale Gewebeschädigung im Rahmen einer viralen Lungeninfektionen wahrnehmen und daraufhin mit der Freisetzung von antiviralen und gewebeschützenden Substanzen reagieren, ist bisher noch unklar. Ziel dieser Studie war es, therapeutische Anwendungsmöglichkeiten von MSC im Rahmen einer Influenzavirus (IV)-Infektion im Mausmodell zu erproben und zu eruieren, wie die therapeutische Wirkung von MSC vermittelt wird. Unter Verwendung von *in vitro*-Kokultursystemen aus MSC mit IV-infizierten alveolären Epithelzellen (iAEC) oder bronchoalveolären Lungenorganoiden (BALO) war es uns möglich, die Wirkung von lung-MSC und BM-MSC auf das Überleben, die Proliferation und die Differenzierung von Alveolarepithelzellen (AEC) vergleichend zu untersuchen. Hierbei ist besonders hervorzuheben, dass sich die Fähigkeit von BM-MSC die Alveolarisierung von Lungenorganoiden (BALO) voranzutreiben durch die Vorkonditionierung der BM-MSC mit löslichen Faktoren aus iAEC oder aus der bronchoalveolären Lavageflüssigkeit von infizierten Mäusen signifikant erhöht. Im Bereich der Differenzierungskapazität stehen die BM-MSC dagegen hinter den lung-MSC zurück. Beide Zelltypen zeigten jedoch *in vitro* vergleichbare antivirale, proproliferative und antiapoptotische Wirkungen in Kokultur mit iAEC. Die schützenden Eigenschaften sowie Änderungen im Transkriptom von BM-MSC wurden auch im *in vivo*-Mausinfektionsmodell untersucht. Dazu wurden BM-MSC drei Tage nach IV-Infektion intratracheal in Wildtyp-Mäuse appliziert. Die Präsenz der BM-MSC führte zu einer Reduktion der Viruslast und der infektionsassoziierten AEC-Apoptose. Zudem konnte das Überleben der Mäuse im Infektionsversuch signifikant verbessert werden. Mittels Fluorescence Activated Cell Sorting (FACS), einer Methode der Durchflusszytometrie, konnten die, in IV-infizierte Mäuse applizierten BM-MSC, zurückgewonnen werden. Änderungen im Transkriptom dieser Zellen im Vergleich zu rückgewonnen BM-MSC aus nicht infizierten Mäusen wurden mit Hilfe der Bulk-RNA-Sequenzierung analysiert. Dabei zeigte sich, dass Interferon-assoziierte Gene sowie das Zytokin Interleukin 11 (IL-11) in BM-MSC, isoliert aus infizierten Mäusen, besonders hochreguliert waren. Durch Gabe von BM-MSC in Interferon-defiziente ($IFNAR^{-/-}$), IV-infizierte Mäusen konnten wir bestätigen, dass die Aktivierung des Typ I-Interferon (IFN)-Signalweges für die antivirale und

antiapoptotische Wirkung der BM-MSC unerlässlich ist. Als Antwort auf die Aktivierung des IFN-Signalwegs setzen BM-MSC IL-11 frei. Wir konnten zeigen, dass diese Freisetzung von IL-11 an der protektiven Wirkung von BM-MSC auf iAEC beteiligt ist.

Zusammenfassend ist zu sagen, dass die Identifizierung des Typ I-IFN/IL-11 Signalweges ein vielversprechendes Ziel für die Entwicklung von MSC-basierten Therapien des akuten Lungenversagens im humanen System darstellt.

VIII. References

[1] M. C. Basil *et al.*, "The Cellular and Physiological Basis for Lung Repair and Regeneration: Past, Present, and Future," *Cell Stem Cell*, vol. 26, no. 4. Cell Press, pp. 482–502, Apr. 02, 2020. doi: 10.1016/j.stem.2020.03.009.

[2] E. E. Morrisey and B. L. M. Hogan, "Preparing for the First Breath: Genetic and Cellular Mechanisms in Lung Development," *Developmental Cell*, vol. 18, no. 1. Cell Press, pp. 8–23, Jan. 19, 2010. doi: 10.1016/j.devcel.2009.12.010.

[3] A. Patwa and A. Shah, "Anatomy and physiology of respiratory system relevant to anaesthesia," *Indian Journal of Anaesthesia*, vol. 59, no. 9. Indian Society of Anaesthetists, pp. 533–541, Sep. 01, 2015. doi: 10.4103/0019-5049.165849.

[4] R. R. Mercer, M. L. Russell, and J. D. Crapo, "Alveolar septal structure in different species," *J Appl Physiol*, vol. 77, no. 3, pp. 1060–1066, 1994, doi: 10.1152/jappl.1994.77.3.1060.

[5] L. B. Ware, "Modeling human lung disease in animals," *American Journal of Physiology-Lung Cellular and Molecular Physiology*, vol. 294, no. 2, pp. L149–L150, Feb. 2008, doi: 10.1152/ajplung.00472.2007.

[6] H. Pan, G. H. Deutsch, and S. E. Wert, "Comprehensive anatomic ontologies for lung development: A comparison of alveolar formation and maturation within mouse and human lung," *J Biomed Semantics*, vol. 10, no. 1, p. 18, Oct. 2019, doi: 10.1186/s13326-019-0209-1.

[7] M. F. Beers and E. E. Morrisey, "The three R's of lung health and disease: Repair, remodeling, and regeneration," *Journal of Clinical Investigation*, vol. 121, no. 6. American Society for Clinical Investigation, pp. 2065–2073, Jun. 01, 2011. doi: 10.1172/JCI45961.

[8] T. J. Desai, D. G. Brownfield, and M. A. Krasnow, "Alveolar progenitor and stem cells in lung development, renewal and cancer," *Nature*, vol. 507, no. 7491, pp. 190–194, 2014, doi: 10.1038/nature12930.

[9] C. E. Barkauskas *et al.*, "Type 2 alveolar cells are stem cells in adult lung," *Journal of Clinical Investigation*, vol. 123, no. 7, pp. 3025–3036, Jul. 2013, doi: 10.1172/JCI68782.

[10] W. J. Zacharias *et al.*, "Regeneration of the lung alveolus by an evolutionarily conserved epithelial progenitor," *Nature*, vol. 555, no. 7695, pp. 251–255, Mar. 2018, doi: 10.1038/nature25786.

[11] H. A. Chapman *et al.*, “Integrin α6β4 identifies an adult distal lung epithelial population with regenerative potential in mice,” *Journal of Clinical Investigation*, vol. 121, no. 7, pp. 2855–2862, Jul. 2011, doi: 10.1172/JCI57673.

[12] J. J. Kathiriya, A. N. Brumwell, J. R. Jackson, X. Tang, and H. A. Chapman, “Distinct Airway Epithelial Stem Cells Hide among Club Cells but Mobilize to Promote Alveolar Regeneration,” *Cell Stem Cell*, vol. 26, no. 3, pp. 346-358.e4, Mar. 2020, doi: 10.1016/j.stem.2019.12.014.

[13] A. Giangreco, E. N. Arwert, I. R. Rosewell, J. Snyder, F. M. Watt, and B. R. Stripp, “Stem cells are dispensable for lung homeostasis but restore airways after injury,” *Proc Natl Acad Sci U S A*, vol. 106, no. 23, pp. 9286–9291, Jun. 2009, doi: 10.1073/pnas.0900668106.

[14] A. Guha, A. Deshpande, A. Jain, P. Sebastiani, and W. v. Cardoso, “Uroplakin 3a+ Cells Are a Distinctive Population of Epithelial Progenitors that Contribute to Airway Maintenance and Post-injury Repair,” *Cell Rep*, vol. 19, no. 2, pp. 246–254, Apr. 2017, doi: 10.1016/j.celrep.2017.03.051.

[15] E. L. Jackson *et al.*, “Analysis of lung tumor initiation and progression using conditional expression of oncogenic K-ras,” *Genes Dev*, vol. 15, no. 24, pp. 3243–3248, Dec. 2001, doi: 10.1101/GAD.943001.

[16] C. F. Bender Kim *et al.*, “Identification of bronchioalveolar stem cells in normal lung and lung cancer,” *Cell*, vol. 121, no. 6, pp. 823–835, Jun. 2005, doi: 10.1016/J.CELL.2005.03.032/ATTACHMENT/32890980-3109-4052-B4F3-F3C387FDC2A9/MMC1.PDF.

[17] I. Salwig *et al.*, “Bronchioalveolar stem cells are a main source for regeneration of distal lung epithelia *in vivo*,” *EMBO J*, vol. 38, no. 12, Jun. 2019, doi: 10.15252/embj.2019102099.

[18] D. M. Raiser and C. F. Kim, “Commentary: Sca-1 and Cells of the Lung: A matter of Different Sorts,” *Stem Cells*, vol. 27, no. 3, pp. 606–611, Mar. 2009, doi: 10.1002/stem.10.

[19] A. E. Vaughan *et al.*, “Lineage-negative progenitors mobilize to regenerate lung epithelium after major injury,” *Nature*, vol. 517, no. 7536, pp. 621–625, Jan. 2015, doi: 10.1038/nature14112.

[20] Y. Xi *et al.*, “Local lung hypoxia determines epithelial fate decisions during alveolar regeneration,” *Nat Cell Biol*, vol. 19, no. 8, pp. 904–914, Aug. 2017, doi: 10.1038/ncb3580.

[21] Y. Yang *et al.*, “Spatial-Temporal Lineage Restrictions of Embryonic p63+ Progenitors Establish Distinct Stem Cell Pools in Adult Airways,” *Dev Cell*, vol. 44, no. 6, pp. 752-761.e4, Mar. 2018, doi: 10.1016/j.devcel.2018.03.001.

[22] H. Danahay, A. D. Pessotti, M. Hild, and A. B. Jaffe, “Notch2 Is Required for Inflammatory Cytokine-Driven Goblet Cell Metaplasia in the Lung,” *Cell Rep*, vol. 10, pp. 239–252, 2015, doi: 10.1016/j.celrep.2014.12.017.

[23] H. Katsura, Y. Kobayashi, P. Rao Tata, and B. L. M. Hogan, “Stem Cell Reports Report IL-1 and TNFa Contribute to the Inflammatory Niche to Enhance Alveolar Regeneration,” *Stem Cell Reports*, vol. 12, pp. 657–666, 2019, doi: 10.1016/j.stemcr.2019.02.013.

[24] A. v. Misharin *et al.*, “Monocyte-derived alveolar macrophages drive lung fibrosis and persist in the lung over the life span,” *Journal of Experimental Medicine*, vol. 214, no. 8, pp. 2387–2404, Aug. 2017, doi: 10.1084/jem.20162152.

[25] A. J. Lechner *et al.*, “Recruited Monocytes and Type 2 Immunity Promote Lung Regeneration following Pneumonectomy,” *Cell Stem Cell*, vol. 21, no. 1, pp. 120-134.e7, Jul. 2017, doi: 10.1016/j.stem.2017.03.024.

[26] F. E. Sirianni, F. S. F. Chu, and D. C. Walker, “Human Alveolar Wall Fibroblasts Directly Link Epithelial Type 2 Cells to Capillary Endothelium,” *Am J Respir Crit Care Med*, vol. 168, no. 12, pp. 1532–1537, Dec. 2003, doi: 10.1164/rccm.200303-371OC.

[27] J. A. Zepp *et al.*, “Distinct Mesenchymal Lineages and Niches Promote Epithelial Self-Renewal and Myofibrogenesis in the Lung,” *Cell*, vol. 170, no. 6, pp. 1134-1148.e10, Sep. 2017, doi: 10.1016/j.cell.2017.07.034.

[28] J. H. Lee *et al.*, “Anatomically and Functionally Distinct Lung Mesenchymal Populations Marked by Lgr5 and Lgr6,” *Cell*, vol. 170, no. 6, pp. 1149-1163.e12, Sep. 2017, doi: 10.1016/j.cell.2017.07.028.

[29] D. Konar, M. Devarasetty, D. v. Yildiz, A. Atala, and S. v. Murphy, “Lung-On-A-Chip Technologies for Disease Modeling and Drug Development,” *Biomed Eng Comput Biol*, vol. 7s1, no. Suppl 1, p. BECB.S34252, Jan. 2016, doi: 10.4137/becb.s34252.

[30] J. Choi, E. Iich, and J. H. Lee, “Organogenesis of adult lung in a dish: Differentiation, disease and therapy,” *Developmental Biology*, vol. 420, no. 2.

Academic Press Inc., pp. 278–286, Dec. 15, 2016. doi: 10.1016/j.ydbio.2016.10.002.

[31] M. Huch, J. A. Knoblich, M. P. Lutolf, and A. Martinez-Arias, “The hope and the hype of organoid research,” *Development (Cambridge)*, vol. 144, no. 6, pp. 938–941, Mar. 2017, doi: 10.1242/dev.150201.

[32] A. E. Hegab *et al.*, “Mimicking the niche of lung epithelial stem cells and characterization of several effectors of their in vitro behavior,” *Stem Cell Res*, vol. 15, no. 1, pp. 109–121, Jul. 2015, doi: 10.1016/j.scr.2015.05.005.

[33] A. I. Vazquez-Armendariz *et al.*, “Multilineage murine stem cells generate complex organoids to model distal lung development and disease,” *EMBO J*, vol. 39, no. 21, Nov. 2020, doi: 10.15252/embj.2019103476.

[34] J. Choi, E. Iich, and J. H. Lee, “Organogenesis of adult lung in a dish: Differentiation, disease and therapy,” *Dev Biol*, vol. 420, no. 2, pp. 278–286, Dec. 2016, doi: 10.1016/J.YDBIO.2016.10.002.

[35] J. van der Vaart and H. Clevers, “Airway organoids as models of human disease,” *J Intern Med*, vol. 289, no. 5, pp. 604–613, May 2021, doi: 10.1111/JOIM.13075.

[36] M. A. Matthay *et al.*, “Acute respiratory distress syndrome,” *Nat Rev Dis Primers*, vol. 5, no. 1, pp. 1–22, Mar. 2018, doi: 10.1038/s41572-019-0069-0.

[37] D. G. Ashbaugh, D. B. Bigelow, T. L. Petty, and B. E. Levine, “Acute respiratory distress in adults.,” *Lancet*, vol. 2, no. 7511, pp. 319–323, 1967, doi: 10.1016/s0140-6736(67)90168-7.

[38] E. D. Riviello *et al.*, “Hospital incidence and outcomes of the acute respiratory distress syndrome using the Kigali modification of the Berlin definition,” *Am J Respir Crit Care Med*, vol. 193, no. 1, pp. 52–59, Jan. 2016, doi: 10.1164/rccm.201503-0584OC.

[39] V. M. Ranieri *et al.*, “Acute respiratory distress syndrome: The Berlin definition,” *JAMA - Journal of the American Medical Association*, vol. 307, no. 23, pp. 2526–2533, Jun. 2012, doi: 10.1001/jama.2012.5669.

[40] M. A. Matthay, B. T. Thompson, and L. B. Ware, “The Berlin definition of acute respiratory distress syndrome: should patients receiving high-flow nasal oxygen be included?,” *Lancet Respir Med*, vol. 9, no. 8, p. 933, Aug. 2021, doi: 10.1016/S2213-2600(21)00105-3.

[41] C. Peteranderl, S. Herold, and C. Schmoldt, “Respiratory Viral Infections: Human Influenza Virus Infections,” *Semin Respir Crit Care Med*, vol. 37, no. 4, p. 487, Aug. 2016, doi: 10.1055/S-0036-1584801.

[42] F. Krammer *et al.*, “Influenza,” *Nature Reviews Disease Primers*, vol. 4, no. 1. Nature Publishing Group, pp. 1–21, Dec. 01, 2018. doi: 10.1038/s41572-018-0002-y.

[43] S. Herold, C. Becker, K. M. Ridge, and G. R. S. Budinger, “Influenza virus-induced lung injury: Pathogenesis and implications for treatment,” *European Respiratory Journal*, vol. 45, no. 5, pp. 1463–1478, May 2015, doi: 10.1183/09031936.00186214.

[44] K. R. Short, E. J. B. V. Kroeze, R. A. M. Fouchier, and T. Kuiken, “Pathogenesis of influenza-induced acute respiratory distress syndrome,” *Lancet Infect Dis*, vol. 14, no. 1, pp. 57–69, Jan. 2014, doi: 10.1016/S1473-3099(13)70286-X.

[45] A. C. Kalil and P. G. Thomas, “Influenza virus-related critical illness: Pathophysiology and epidemiology,” *Crit Care*, vol. 23, no. 1, pp. 1–7, Jul. 2019, doi: 10.1186/S13054-019-2539-X/TABLES/2.

[46] S. K. Leaver and T. W. Evans, “Acute respiratory distress syndrome,” *BMJ : British Medical Journal*, vol. 335, no. 7616, p. 389, Aug. 2007, doi: 10.1136/BMJ.39293.624699.AD.

[47] M. A. Matthay, L. B. Ware, and G. A. Zimmerman, “The acute respiratory distress syndrome,” *Journal of Clinical Investigation*, vol. 122, no. 8. J Clin Invest, pp. 2731–2740, Aug. 01, 2012. doi: 10.1172/JCI60331.

[48] K. Högner *et al.*, “Macrophage-expressed IFN-β Contributes to Apoptotic Alveolar Epithelial Cell Injury in Severe Influenza Virus Pneumonia,” *PLoS Pathog*, vol. 9, no. 2, Feb. 2013, doi: 10.1371/journal.ppat.1003188.

[49] L. B. Ware and M. A. Matthay, “Alveolar fluid clearance is impaired in the majority of patients with acute lung injury and the acute respiratory distress syndrome,” *Am J Respir Crit Care Med*, vol. 163, no. 6, pp. 1376–1383, 2001, doi: 10.1164/ajrccm.163.6.2004035.

[50] W. J. Zacharias *et al.*, “Regeneration of the lung alveolus by an evolutionarily conserved epithelial progenitor,” *Nature 2018 555:7695*, vol. 555, no. 7695, pp. 251–255, Feb. 2018, doi: 10.1038/nature25786.

[51] A. N. Nabhan, D. G. Brownfield, P. B. Harbury, M. A. Krasnow, and T. J. Desai, “Single-cell Wnt signaling niches maintain stemness of alveolar type 2 cells,”

Science (1979), vol. 359, no. 6380, pp. 1118–1123, Mar. 2018, doi: 10.1126/SCIENCE.AAM6603/SUPPL_FILE/AAM6603-NABHAN-SM.PDF.

[52] R. L. Zemans *et al.*, "Neutrophil transmigration triggers repair of the lung epithelium via β-catenin signaling," *Proc Natl Acad Sci U S A*, vol. 108, no. 38, pp. 15990–15995, Oct. 2011, doi: 10.1073/pnas.1110144108.

[53] J. Quantius *et al.*, "Influenza Virus Infects Epithelial Stem/Progenitor Cells of the Distal Lung: Impact on Fgfr2b-Driven Epithelial Repair," *PLoS Pathog*, vol. 12, no. 6, Jun. 2016, doi: 10.1371/journal.ppat.1005544.

[54] N. M. Nikolaidis *et al.*, "Mitogenic stimulation accelerates influenza-induced mortality by increasing susceptibility of alveolar type II cells to infection," *Proc Natl Acad Sci U S A*, vol. 114, no. 32, pp. E6613–E6622, Aug. 2017, doi: 10.1073/pnas.1621172114.

[55] R. K. Albert, "The role of ventilation-induced surfactant dysfunction and atelectasis in causing acute respiratory distress syndrome," *American Journal of Respiratory and Critical Care Medicine*, vol. 185, no. 7. Am J Respir Crit Care Med, pp. 702–708, Apr. 01, 2012. doi: 10.1164/rccm.201109-1667PP.

[56] E. Fuchs and J. A. Segre, "Stem Cells: A New Lease on Life," *Cell*, vol. 100, no. 1, pp. 143–155, Jan. 2000, doi: 10.1016/S0092-8674(00)81691-8.

[57] W. Zakrzewski, M. Dobrzyński, M. Szymonowicz, and Z. Rybak, "Stem cells: Past, present, and future," *Stem Cell Res Ther*, vol. 10, no. 1, pp. 1–22, Feb. 2019, doi: 10.1186/S13287-019-1165-5/FIGURES/8.

[58] T. Ma, "Mesenchymal stem cells: From bench to bedside," *World J Stem Cells*, vol. 2, no. 2, p. 13, 2010, doi: 10.4252/wjsc.v2.i2.13.

[59] B. E. Tuch, "Stem cells A clinical update," *Aust Fam Physician*, vol. 35, no. 9, pp. 719–721, 2006.

[60] Q. Zhao, H. Ren, and Z. Han, "Mesenchymal stem cells: Immunomodulatory capability and clinical potential in immune diseases," *Journal of Cellular Immunotherapy*, vol. 2, no. 1. Shanghai Hengrun Biomedical Technology Research Institute, pp. 3–20, Mar. 01, 2016. doi: 10.1016/j.jocit.2014.12.001.

[61] Y. Han, X. Li, Y. Zhang, Y. Han, F. Chang, and J. Ding, "Mesenchymal Stem Cells for Regenerative Medicine," *Cells*, vol. 8, no. 8, p. 886, Aug. 2019, doi: 10.3390/cells8080886.

[62] J. Kobolak, A. Dinnyes, A. Memic, A. Khademhosseini, and A. Mobasheri, "Mesenchymal stem cells: Identification, phenotypic characterization,

biological properties and potential for regenerative medicine through biomaterial micro-engineering of their niche," *Methods*, vol. 99. Academic Press Inc., pp. 62–68, Apr. 15, 2016. doi: 10.1016/j.ymeth.2015.09.016.

[63] M. MK, T. MA, M. JD, M. M, and G. SL, "Phenotypic and Functional Comparison of Cultures of Marrow-Derived Mesenchymal Stem Cells (MSCs) and Stromal Cells," *J Cell Physiol*, vol. 176, no. 1, 1998, doi: 10.1002/(SICI)1097-4652(199807)176:1<57::AID-JCP7>3.0.CO;2-7.

[64] D. Noel, "Short-Term BMP-2 Expression Is Sufficient for In Vivo Osteochondral Differentiation of Mesenchymal Stem Cells," *Stem Cells*, vol. 22, no. 1, pp. 74–85, Jan. 2004, doi: 10.1634/stemcells.22-1-74.

[65] H. K. Lee, B. H. Lee, S. A. Park, and C. W. Kim, "The proteomic analysis of an adipocyte differentiated from human mesenchymal stem cells using two-dimensional gel electrophoresis," *Proteomics*, vol. 6, no. 4, pp. 1223–1229, Feb. 2006, doi: 10.1002/pmic.200500385.

[66] M. Krampera, G. Pizzolo, G. Aprili, and M. Franchini, "Mesenchymal stem cells for bone, cartilage, tendon and skeletal muscle repair," *Bone*, vol. 39, no. 4. Bone, pp. 678–683, Oct. 2006. doi: 10.1016/j.bone.2006.04.020.

[67] V. Labovsky *et al.*, "Cardiomyogenic differentiation of human bone marrow mesenchymal cells: Role of cardiac extract from neonatal rat cardiomyocytes," *Differentiation*, vol. 79, no. 2, pp. 93–101, Feb. 2010, doi: 10.1016/j.diff.2009.10.001.

[68] S. B. Zhou, J. Wang, C. A. Chiang, L. L. Sheng, and Q. F. Li, "Mechanical stretch upregulates SDF-1α in skin tissue and induces migration of circulating bone marrow-derived stem cells into the expanded skin," *Stem Cells*, vol. 31, no. 12, pp. 2703–2713, Dec. 2013, doi: 10.1002/stem.1479.

[69] C. S. Padovan *et al.*, "Expression of Neuronal Markers in Differentiated Marrow Stromal Cells and CD133+ Stem-Like Cells," *Cell Transplant*, vol. 12, no. 8, pp. 839–848, 2004, doi: 10.3727/000000003771000183.

[70] D. N. Kotton *et al.*, "Bone marrow-derived cells as progenitors of lung alveolar epithelium," *Development*, vol. 128, no. 24, pp. 5181 LP – 5188, Dec. 2001, [Online]. Available: http://dev.biologists.org/content/128/24/5181.abstract

[71] Q. Zhao *et al.*, "Differentiation of human umbilical cord mesenchymal stromal cells into low immunogenic hepatocyte-like cells," *Cytotherapy*, vol. 11, no. 4, pp. 414–426, 2009, doi: 10.1080/14653240902849754.

[72] E. Karaoz, A. Okcu, Z. S. Ünal, C. Subasi, O. Saglam, and G. Duruksu, "Adipose tissue-derived mesenchymal stromal cells efficiently differentiate into insulin-producing cells in pancreatic islet microenvironment both in vitro and in vivo," *Cytotherapy*, vol. 15, no. 5, pp. 557–570, May 2013, doi: 10.1016/j.jcyt.2013.01.005.

[73] E. Bell *et al.*, "Dermal stem cells can differentiate down an endothelial lineage," *Stem Cells Dev*, vol. 21, no. 16, pp. 3019–3030, Nov. 2012, doi: 10.1089/scd.2011.0694.

[74] E. M. Horwitz *et al.*, "Clarification of the nomenclature for MSC: The International Society for Cellular Therapy position statement," *Cytotherapy*, vol. 7, no. 5, pp. 393–395, Jan. 2005, doi: 10.1080/14653240500319234.

[75] M. Dominici *et al.*, "Minimal criteria for defining multipotent mesenchymal stromal cells. The International Society for Cellular Therapy position statement," *Cytotherapy*, vol. 8, no. 4, pp. 315–317, Aug. 2006, doi: 10.1080/14653240600855905.

[76] R. E. B. Fitzsimmons, M. S. Mazurek, A. Soos, and C. A. Simmons, "Mesenchymal Stromal/Stem Cells in Regenerative Medicine and Tissue Engineering," *Stem Cells Int*, vol. 2018, 2018, doi: 10.1155/2018/8031718.

[77] G. Chamberlain, J. Fox, B. Ashton, and J. Middleton, "Concise Review: Mesenchymal Stem Cells: Their Phenotype, Differentiation Capacity, Immunological Features, and Potential for Homing," *Stem Cells*, vol. 25, no. 11, pp. 2739–2749, Nov. 2007, doi: 10.1634/stemcells.2007-0197.

[78] S. Viswanathan *et al.*, "Mesenchymal stem versus stromal cells: International Society for Cell & Gene Therapy (ISCT®) Mesenchymal Stromal Cell committee position statement on nomenclature," *Cytotherapy*, vol. 21, no. 10, pp. 1019–1024, Oct. 2019, doi: 10.1016/j.jcyt.2019.08.002.

[79] W. Wagner *et al.*, "Comparative characteristics of mesenchymal stem cells from human bone marrow, adipose tissue, and umbilical cord blood," *Exp Hematol*, vol. 33, no. 11, pp. 1402–1416, Nov. 2005, doi: 10.1016/j.exphem.2005.07.003.

[80] R. Hass, C. Kasper, S. Böhm, and R. Jacobs, "Different populations and sources of human mesenchymal stem cells (MSC): A comparison of adult and neonatal tissue-derived MSC," *Cell Communication and Signaling*, vol. 9, no. 1. BioMed Central, pp. 1–14, May 14, 2011. doi: 10.1186/1478-811X-9-12.

[81] E. Jones and R. Schäfer, “Where is the common ground between bone marrow mesenchymal stem/stromal cells from different donors and species?,” *Stem Cell Res Ther*, vol. 6, no. 1, Aug. 2015, doi: 10.1186/S13287-015-0144-8.

[82] J. Kobolak, A. Dinnyes, A. Memic, A. Khademhosseini, and A. Mobasheri, “Mesenchymal stem cells: Identification, phenotypic characterization, biological properties and potential for regenerative medicine through biomaterial micro-engineering of their niche,” *Methods*, vol. 99. Academic Press Inc., pp. 62–68, Apr. 15, 2016. doi: 10.1016/j.ymeth.2015.09.016.

[83] Y. Hu *et al.*, “Comparative Study on In Vitro Culture of Mouse Bone Marrow Mesenchymal Stem Cells,” *Stem Cells Int*, vol. 2018, 2018, doi: 10.1155/2018/6704583.

[84] D. D. Houlihan *et al.*, “Isolation of mouse mesenchymal stem cells on the basis of expression of Sca-1 and PDGFR-α,” *Nat Protoc*, vol. 7, no. 12, pp. 2103–2111, 2012, doi: 10.1038/nprot.2012.125.

[85] S. Morikawa *et al.*, “Prospective identification, isolation, and systemic transplantation of multipotent mesenchymal stem cells in murine bone marrow,” *Journal of Experimental Medicine*, vol. 206, no. 11, pp. 2483–2496, Oct. 2009, doi: 10.1084/jem.20091046.

[86] S. Morikawa *et al.*, “Development of mesenchymal stem cells partially originate from the neural crest,” *Biochem Biophys Res Commun*, vol. 379, no. 4, pp. 1114–1119, Feb. 2009, doi: 10.1016/j.bbrc.2009.01.031.

[87] Y. Koide *et al.*, “Two Distinct Stem Cell Lineages in Murine Bone Marrow,” *Stem Cells*, vol. 25, no. 5, pp. 1213–1221, May 2007, doi: 10.1634/stemcells.2006-0325.

[88] J. Cai, M. L. Weiss, and M. S. Rao, “In search of ‘stemness,’” *Experimental Hematology*, vol. 32, no. 7. Elsevier, pp. 585–598, Jul. 01, 2004. doi: 10.1016/j.exphem.2004.03.013.

[89] J. de Boer, H. J. Wang, and C. van Blitterswijk, “Effects of Wnt Signaling on Proliferation and Differentiation of Human Mesenchymal Stem Cells,” in *Tissue Engineering*, Mar. 2004, vol. 10, no. 3–4, pp. 393–401. doi: 10.1089/107632704323061753.

[90] J. C. Estrada *et al.*, “Culture of human mesenchymal stem cells at low oxygen tension improves growth and genetic stability by activating glycolysis,” *Cell Death Differ*, vol. 19, no. 5, pp. 743–755, May 2012, doi: 10.1038/cdd.2011.172.

[91] G. Chamberlain, J. Fox, B. Ashton, and J. Middleton, “Concise Review: Mesenchymal Stem Cells: Their Phenotype, Differentiation Capacity, Immunological Features, and Potential for Homing,” *Stem Cells*, vol. 25, no. 11, pp. 2739–2749, Nov. 2007, doi: 10.1634/stemcells.2007-0197.

[92] J. L. Ramírez-Zacarías, F. Castro-Muñozledo, and W. Kuri-Harcuch, “Quantitation of adipose conversion and triglycerides by staining intracytoplasmic lipids with Oil red O,” *Histochemistry*, vol. 97, no. 6, pp. 493–497, Jul. 1992, doi: 10.1007/BF00316069.

[93] B. Johnstone, T. M. Hering, A. I. Caplan, V. M. Goldberg, and J. U. Yoo, “In vitro chondrogenesis of bone marrow-derived mesenchymal progenitor cells,” *Exp Cell Res*, vol. 238, no. 1, pp. 265–272, Jan. 1998, doi: 10.1006/EXCR.1997.3858.

[94] S. Boeuf and W. Richter, “Chondrogenesis of mesenchymal stem cells: Role of tissue source and inducing factors,” *Stem Cell Res Ther*, vol. 1, no. 4, pp. 1–9, Oct. 2010, doi: 10.1186/SCRT31/TABLES/2.

[95] P. Whiteman, “The quantitative measurement of Alcian Blue–glycosaminoglycan complexes,” *Biochemical Journal*, vol. 131, no. 2, pp. 343–350, Feb. 1973, doi: 10.1042/BJ1310343.

[96] D. E. Terry, R. K. Chopra, J. Ovenden, and T. P. Anastassiades, “Differential Use of Alcian Blue and Toluidine Blue Dyes for the Quantification and Isolation of Anionic Glycoconjugates from Cell Cultures: Application to Proteoglycans and a High-Molecular-Weight Glycoprotein Synthesized by Articular Chondrocytes,” *Anal Biochem*, vol. 285, no. 2, pp. 211–219, Oct. 2000, doi: 10.1006/ABIO.2000.4761.

[97] P. Garg, M. M. Mazur, A. C. Buck, M. E. Wandtke, J. Liu, and N. A. Ebraheim, “Prospective Review of Mesenchymal Stem Cells Differentiation into Osteoblasts,” *Orthop Surg*, vol. 9, no. 1, pp. 13–19, Feb. 2017, doi: 10.1111/OS.12304.

[98] M. S. Friedman, M. W. Lone, and K. D. Hankenson, “Osteogenic differentiation of human mesenchymal stem cells is regulated by bone morphogenetic protein-6,” *J Cell Biochem*, vol. 98, no. 3, pp. 538–554, Jun. 2006, doi: 10.1002/JCB.20719.

[99] A. Greenbaum *et al.*, "CXCL12 in early mesenchymal progenitors is required for haematopoietic stem-cell maintenance," *Nature*, vol. 495, no. 7440, pp. 227–230, Mar. 2013, doi: 10.1038/nature11926.

[100] H. R. Hofer and R. S. Tuan, "Secreted trophic factors of mesenchymal stem cells support neurovascular and musculoskeletal therapies," *Stem Cell Research and Therapy*, vol. 7, no. 1. BioMed Central Ltd., p. 131, Sep. 09, 2016. doi: 10.1186/s13287-016-0394-0.

[101] T. Stessuk, M. A. Ruiz, O. T. Greco, A. Bilaqui, M. J. de O. Ribeiro-Paes, and J. T. Ribeiro-Paes, "Phase I clinical trial of cell therapy in patients with advanced chronic obstructive pulmonary disease: Follow-up of up to 3 years," *Rev Bras Hematol Hemoter*, vol. 35, no. 5, pp. 352–357, 2013, doi: 10.5581/1516-8484.20130113.

[102] F. Nitzsche, C. Müller, B. Lukomska, J. Jolkkonen, A. Deten, and J. Boltze, "Concise Review: MSC Adhesion Cascade—Insights into Homing and Transendothelial Migration," *Stem Cells*, vol. 35, no. 6. Wiley-Blackwell, pp. 1446–1460, Jun. 01, 2017. doi: 10.1002/stem.2614.

[103] B. Argibay *et al.*, "Intraarterial route increases the risk of cerebral lesions after mesenchymal cell administration in animal model of ischemia," *Sci Rep*, vol. 7, no. 1, pp. 1–17, Jan. 2017, doi: 10.1038/srep40758.

[104] A. Naji, M. Eitoku, B. Favier, F. Deschaseaux, N. Rouas-Freiss, and N. Suganuma, "Biological functions of mesenchymal stem cells and clinical implications," *Cellular and Molecular Life Sciences*, vol. 76, no. 17, pp. 3323–3348, Sep. 2019, doi: 10.1007/s00018-019-03125-1.

[105] T. J. Kean, P. Lin, A. I. Caplan, and J. E. Dennis, "MSCs: Delivery routes and engraftment, cell-targeting strategies, and immune modulation," *Stem Cells Int*, 2013, doi: 10.1155/2013/732742.

[106] D. A. de Ugarte *et al.*, "Differential expression of stem cell mobilization-associated molecules on multi-lineage cells from adipose tissue and bone marrow," *Immunol Lett*, vol. 89, no. 2–3, pp. 267–270, Oct. 2003, doi: 10.1016/S0165-2478(03)00108-1.

[107] Y. Shi, J. Su, A. I. Roberts, P. Shou, A. B. Rabson, and G. Ren, "How mesenchymal stem cells interact with tissue immune responses," *Trends in Immunology*, vol. 33, no. 3. Elsevier, pp. 136–143, Mar. 01, 2012. doi: 10.1016/j.it.2011.11.004.

[108] S. L. Tomchuck, K. J. Zwezdaryk, S. B. Coffelt, R. S. Waterman, E. S. Danka, and A. B. Scandurro, “Toll-Like Receptors on Human Mesenchymal Stem Cells Drive Their Migration and Immunomodulating Responses,” *Stem Cells*, vol. 26, no. 1, pp. 99–107, Jan. 2008, doi: 10.1634/stemcells.2007-0563.

[109] R. S. Waterman, S. L. Tomchuck, S. L. Henkle, and A. M. Betancourt, “A new mesenchymal stem cell (MSC) paradigm: Polarization into a pro-inflammatory MSC1 or an immunosuppressive MSC2 phenotype,” *PLoS One*, vol. 5, no. 4, 2010, doi: 10.1371/journal.pone.0010088.

[110] Y. Wang, X. Chen, W. Cao, and Y. Shi, “Plasticity of mesenchymal stem cells in immunomodulation: Pathological and therapeutic implications,” *Nature Immunology*, vol. 15, no. 11. Nature Publishing Group, pp. 1009–1016, Oct. 25, 2014. doi: 10.1038/ni.3002.

[111] G. Ren *et al.*, “Mesenchymal Stem Cell-Mediated Immunosuppression Occurs via Concerted Action of Chemokines and Nitric Oxide,” *Cell Stem Cell*, vol. 2, no. 2, pp. 141–150, Feb. 2008, doi: 10.1016/j.stem.2007.11.014.

[112] M. E. Bernardo and W. E. Fibbe, “Mesenchymal stromal cells: Sensors and switchers of inflammation,” *Cell Stem Cell*, vol. 13, no. 4. Cell Press, pp. 392–402, Oct. 03, 2013. doi: 10.1016/j.stem.2013.09.006.

[113] W. Jiang and J. Xu, “Immune modulation by mesenchymal stem cells,” *Cell Prolif*, vol. 53, no. 1, Jan. 2020, doi: 10.1111/cpr.12712.

[114] A. J. Nauta and W. E. Fibbe, “Immunomodulatory properties of mesenchymal stromal cells,” *Blood*, vol. 110, no. 10. Blood, pp. 3499–3506, Nov. 15, 2007. doi: 10.1182/blood-2007-02-069716.

[115] P. A. Sotiropoulou, S. A. Perez, A. D. Gritzapis, C. N. Baxevanis, and M. Papamichail, “Interactions Between Human Mesenchymal Stem Cells and Natural Killer Cells,” *Stem Cells*, vol. 24, no. 1, pp. 74–85, Jan. 2006, doi: 10.1634/stemcells.2004-0359.

[116] S. Rutella, S. Danese, and G. Leone, “Tolerogenic dendritic cells: Cytokine modulation comes of age,” *Blood*, vol. 108, no. 5. American Society of Hematology, pp. 1435–1440, Sep. 01, 2006. doi: 10.1182/blood-2006-03-006403.

[117] A. Corcione *et al.*, “Human mesenchymal stem cells modulate B-cell functions,” *Blood*, vol. 107, no. 1, pp. 367–372, Jan. 2006, doi: 10.1182/blood-2005-07-2657.

[118] J. Hou *et al.*, “Mesenchymal stem cells promote endothelial progenitor cell proliferation by secreting insulin-like growth factor-1,” *Mol Med Rep*, vol. 16, no. 2, pp. 1502–1508, Aug. 2017, doi: 10.3892/MMR.2017.6741/HTML.

[119] K. M. Akram, S. Samad, M. A. Spiteri, and N. R. Forsyth, “Mesenchymal stem cells promote alveolar epithelial cell wound repair in vitro through distinct migratory and paracrine mechanisms,” *Respir Res*, vol. 14, no. 1, pp. 1–16, Jan. 2013, doi: 10.1186/1465-9921-14-9/TABLES/1.

[120] S. Ma, N. Xie, W. Li, B. Yuan, Y. Shi, and Y. Wang, “Immunobiology of mesenchymal stem cells,” *Cell Death and Differentiation*, vol. 21, no. 2. Cell Death Differ, pp. 216–225, Feb. 2014. doi: 10.1038/cdd.2013.158.

[121] B. Parekkadan and J. M. Milwid, “Mesenchymal stem cells as therapeutics,” *Annual Review of Biomedical Engineering*, vol. 12. NIH Public Access, pp. 87–117, Aug. 15, 2010. doi: 10.1146/annurev-bioeng-070909-105309.

[122] L. A. Huppert, K. D. Liu, and M. A. Matthay, “Therapeutic potential of mesenchymal stromal cells in the treatment of ARDS,” *Transfusion (Paris)*, vol. 59, no. S1, pp. 869–875, Feb. 2019, doi: 10.1111/trf.14835.

[123] A. Naji, M. Eitoku, B. Favier, F. Deschaseaux, N. Rouas-Freiss, and N. Suganuma, “Biological functions of mesenchymal stem cells and clinical implications,” *Cellular and Molecular Life Sciences*, vol. 76, no. 17. Birkhauser Verlag AG, pp. 3323–3348, Sep. 01, 2019. doi: 10.1007/s00018-019-03125-1.

[124] M. Kabat, I. Bobkov, S. Kumar, and M. Grumet, “Trends in mesenchymal stem cell clinical trials 2004-2018: Is efficacy optimal in a narrow dose range?,” *Stem Cells Transl Med*, vol. 9, no. 1, pp. 17–27, Jan. 2020, doi: 10.1002/sctm.19-0202.

[125] M. A. Matthay, S. Pati, and J. W. Lee, “Concise Review: Mesenchymal Stem (Stromal) Cells: Biology and Preclinical Evidence for Therapeutic Potential for Organ Dysfunction Following Trauma or Sepsis,” *Stem Cells*, vol. 35, no. 2, pp. 316–324, Feb. 2017, doi: 10.1002/stem.2551.

[126] R. H. Lee *et al.*, “Intravenous hMSCs Improve Myocardial Infarction in Mice because Cells Embolized in Lung Are Activated to Secrete the Anti-inflammatory Protein TSG-6,” *Cell Stem Cell*, vol. 5, no. 1, pp. 54–63, Jul. 2009, doi: 10.1016/j.stem.2009.05.003.

[127] M. A. Canham, J. D. M. Campbell, and J. C. Mountford, “The use of mesenchymal stromal cells in the treatment of coronavirus disease 2019,”

Journal of Translational Medicine 2020 18:1, vol. 18, no. 1, pp. 1–15, Sep. 2020, doi: 10.1186/S12967-020-02532-4.

[128] D. K. Sung, Y. S. Chang, S. I. Sung, H. S. Yoo, S. Y. Ahn, and W. S. Park, "Antibacterial effect of mesenchymal stem cells against Escherichia coli is mediated by secretion of beta- defensin- 2 via toll- like receptor 4 signalling," *Cell Microbiol*, vol. 18, no. 3, pp. 424–436, Mar. 2016, doi: 10.1111/CMI.12522.

[129] M. Khatri, L. A. Richardson, and T. Meulia, "Mesenchymal stem cell-derived extracellular vesicles attenuate influenza virus-induced acute lung injury in a pig model," *Stem Cell Res Ther*, vol. 9, no. 1, Jan. 2018, doi: 10.1186/S13287-018-0774-8.

[130] N. Gupta, X. Su, B. Popov, J. W. Lee, V. Serikov, and M. A. Matthay, "Intrapulmonary Delivery of Bone Marrow-Derived Mesenchymal Stem Cells Improves Survival and Attenuates Endotoxin-Induced Acute Lung Injury in Mice," *The Journal of Immunology*, vol. 179, no. 3, pp. 1855–1863, Aug. 2007, doi: 10.4049/jimmunol.179.3.1855.

[131] J. W. Lee, A. Krasnodembskaya, D. H. McKenna, Y. Song, J. Abbott, and M. A. Matthay, "Therapeutic effects of human mesenchymal stem cells in ex vivo human lungs injured with live bacteria," *Am J Respir Crit Care Med*, vol. 187, no. 7, pp. 751–760, Apr. 2013, doi: 10.1164/rccm.201206-0990OC.

[132] L. Raffaghello *et al.*, "Human Mesenchymal Stem Cells Inhibit Neutrophil Apoptosis: A Model for Neutrophil Preservation in the Bone Marrow Niche," *Stem Cells*, vol. 26, no. 1, pp. 151–162, Jan. 2008, doi: 10.1634/stemcells.2007-0416.

[133] M. v. Jackson *et al.*, "Mitochondrial Transfer via Tunneling Nanotubes is an Important Mechanism by Which Mesenchymal Stem Cells Enhance Macrophage Phagocytosis in the In Vitro and In Vivo Models of ARDS," *Stem Cells*, vol. 34, no. 8, pp. 2210–2223, Aug. 2016, doi: 10.1002/STEM.2372.

[134] J. W. Lee, X. Fang, N. Gupta, V. Serikov, and M. A. Matthay, "Allogeneic human mesenchymal stem cells for treatment of E. coli endotoxin-induced acute lung injury in the ex vivo perfused human lung," *Proc Natl Acad Sci U S A*, vol. 106, no. 38, pp. 16357–16362, Sep. 2009, doi: 10.1073/pnas.0907996106.

[135] A. M. Foskett, N. Bazhanov, X. Ti, A. Tiblow, T. J. Bartosh, and D. J. Prockop, "Phase-directed therapy: TSG-6 targeted to early inflammation improves

bleomycin-injured lungs," *Am J Physiol Lung Cell Mol Physiol*, vol. 306, no. 2, Jan. 2014, doi: 10.1152/ajplung.00240.2013.

[136] L. Ionescu *et al.*, "Stem cell conditioned medium improves acute lung injury in mice: In vivo evidence for stem cell paracrine action," *Am J Physiol Lung Cell Mol Physiol*, vol. 303, no. 11, 2012, doi: 10.1152/ajplung.00144.2011.

[137] X. Fang *et al.*, " Human Mesenchymal Stem (Stromal) Cells Promote the Resolution of Acute Lung Injury in Part through Lipoxin A 4 ," *The Journal of Immunology*, vol. 195, no. 3, pp. 875–881, Aug. 2015, doi: 10.4049/jimmunol.1500244.

[138] C. Li *et al.*, "Mesenchymal stem cells and their mitochondrial transfer: a double-edged sword," *Biosci Rep*, vol. 39, no. 5, May 2019, doi: 10.1042/BSR20182417.

[139] S. C. Abreu, D. J. Weiss, and P. R. M. Rocco, "Extracellular vesicles derived from mesenchymal stromal cells: A therapeutic option in respiratory diseases?," *Stem Cell Res Ther*, vol. 7, no. 1, pp. 1–10, Apr. 2016, doi: 10.1186/s13287-016-0317-0.

[140] X. L. Fan, Y. Zhang, X. Li, and Q. L. Fu, "Mechanisms underlying the protective effects of mesenchymal stem cell-based therapy," *Cellular and Molecular Life Sciences*, vol. 77, no. 14, pp. 2771–2794, Jul. 2020, doi: 10.1007/s00018-020-03454-6.

[141] X. Fang, A. P. Neyrinck, M. A. Matthay, and J. W. Lee, "Allogeneic human mesenchymal stem cells restore epithelial protein permeability in cultured human alveolar type II cells by secretion of angiopoietin-1," *Journal of Biological Chemistry*, vol. 285, no. 34, pp. 26211–26222, Aug. 2010, doi: 10.1074/jbc.M110.119917.

[142] A. Goolaerts *et al.*, "Conditioned media from mesenchymal stromal cells restore sodium transport and preserve epithelial permeability in an in vitro model of acute alveolar injury," *Am J Physiol Lung Cell Mol Physiol*, vol. 306, no. 11, Jun. 2014, doi: 10.1152/ajplung.00242.2013.

[143] L. da Silva Meirelles, A. M. Fontes, D. T. Covas, and A. I. Caplan, "Mechanisms involved in the therapeutic properties of mesenchymal stem cells," *Cytokine Growth Factor Rev*, vol. 20, no. 5–6, pp. 419–427, Oct. 2009, doi: 10.1016/J.CYTOGFR.2009.10.002.

[144] D. G. Phinney *et al.*, “Mesenchymal stem cells use extracellular vesicles to outsource mitophagy and shuttle microRNAs,” *Nat Commun*, vol. 6, Oct. 2015, doi: 10.1038/ncomms9472.

[145] M. N. Islam *et al.*, “Mitochondrial transfer from bone-marrow-derived stromal cells to pulmonary alveoli protects against acute lung injury,” *Nat Med*, vol. 18, no. 5, pp. 759–765, May 2012, doi: 10.1038/nm.2736.

[146] M. v. Jackson *et al.*, “Mitochondrial Transfer via Tunneling Nanotubes is an Important Mechanism by Which Mesenchymal Stem Cells Enhance Macrophage Phagocytosis in the In Vitro and In Vivo Models of ARDS,” *Stem Cells*, vol. 34, no. 8, pp. 2210–2223, Aug. 2016, doi: 10.1002/stem.2372.

[147] J. Joshi, M. D. Abnavi, and C. R. Kothapalli, “Synthesis and secretome release by human bone marrow mesenchymal stem cell spheroids within three-dimensional collagen hydrogels: Integrating experiments and modelling,” *J Tissue Eng Regen Med*, vol. 13, no. 10, pp. 1923–1937, Oct. 2019, doi: 10.1002/TERM.2943.

[148] F. Sottile, F. Aulicino, I. Theka, and M. P. Cosma, “Mesenchymal stem cells generate distinct functional hybrids in vitro via cell fusion or entosis,” *Sci Rep*, vol. 6, Nov. 2016, doi: 10.1038/SREP36863.

[149] Y. G. Zhu *et al.*, “Human mesenchymal stem cell microvesicles for treatment of Escherichia coli endotoxin-induced acute lung injury in mice,” *Stem Cells*, vol. 32, no. 1, pp. 116–125, Jan. 2014, doi: 10.1002/stem.1504.

[150] T. J. Morrison *et al.*, “Mesenchymal stromal cells modulate macrophages in clinically relevant lung injury models by extracellular vesicle mitochondrial transfer,” *Am J Respir Crit Care Med*, vol. 196, no. 10, pp. 1275–1286, Nov. 2017, doi: 10.1164/rccm.201701-0170OC.

[151] J. Park *et al.*, “Therapeutic effects of human mesenchymal stem cell microvesicles in an ex vivo perfused human lung injured with severe E. coli pneumonia,” *Thorax*, vol. 74, no. 1, pp. 43–50, Jan. 2019, doi: 10.1136/thoraxjnl-2018-211576.

[152] U. Müller *et al.*, “Functional role of type I and type II interferons in antiviral defense,” *Science (1979)*, vol. 264, no. 5167, pp. 1918–1921, 1994, doi: 10.1126/science.8009221.

[153] P. Reuther, K. Göpfert, A. H. Dudek, M. Heiner, S. Herold, and M. Schwemmle, “Generation of a variety of stable Influenza A reporter viruses by genetic

engineering of the NS gene segment," *Sci Rep*, vol. 5, no. 1, pp. 1–17, Jun. 2015, doi: 10.1038/srep11346.

[154] M. Corti, A. R. Brody, and J. H. Harrison, "Isolation and primary culture of murine alveolar type II cells.," *Am J Respir Cell Mol Biol*, vol. 14, no. 4, pp. 309–315, Apr. 1996, doi: 10.1165/ajrcmb.14.4.8600933.

[155] S. Herold *et al.*, "Alveolar Epithelial Cells Direct Monocyte Transepithelial Migration upon Influenza Virus Infection: Impact of Chemokines and Adhesion Molecules," *The Journal of Immunology*, vol. 177, no. 3, pp. 1817–1824, Aug. 2006, doi: 10.4049/jimmunol.177.3.1817.

[156] J. Schindelin *et al.*, "Fiji: An open-source platform for biological-image analysis," *Nature Methods*, vol. 9, no. 7. Nature Publishing Group, pp. 676–682, Jun. 28, 2012. doi: 10.1038/nmeth.2019.

[157] B. C. Sheridan, C. A. Dinarello, D. R. Meldrum, D. A. Fullerton, C. H. Selzman, and R. C. Mcintyre, "Interleukin-11 attenuates pulmonary inflammation and vasomotor dysfunction in endotoxin-induced lung injury," *Am J Physiol Lung Cell Mol Physiol*, vol. 277, no. 5 21-5, 1999, doi: 10.1152/AJPLUNG.1999.277.5.L861/ASSET/IMAGES/LARGE/ALUN61023006X.JPEG.

[158] B. Ng *et al.*, "Interleukin-11 is a therapeutic target in idiopathic pulmonary fibrosis," *Sci Transl Med*, vol. 11, no. 511, Sep. 2019, doi: 10.1126/SCITRANSLMED.AAW1237/SUPPL_FILE/AAW1237_SM.PDF.

[159] S. Schafer *et al.*, "IL-11 is a crucial determinant of cardiovascular fibrosis," *Nature 2017 552:7683*, vol. 552, no. 7683, pp. 110–115, Nov. 2017, doi: 10.1038/nature24676.

[160] K. E. Traber *et al.*, "Roles of interleukin-11 during acute bacterial pneumonia," *PLoS One*, vol. 14, no. 8, p. e0221029, Aug. 2019, doi: 10.1371/JOURNAL.PONE.0221029.

[161] K. M. Akram, N. Patel, M. A. Spiteri, and N. R. Forsyth, "Lung Regeneration: Endogenous and Exogenous Stem Cell Mediated Therapeutic Approaches," *International Journal of Molecular Sciences 2016, Vol. 17, Page 128*, vol. 17, no. 1, p. 128, Jan. 2016, doi: 10.3390/IJMS17010128.

[162] J. L. McQualter, K. Yuen, B. Williams, and I. Bertoncello, "Evidence of an epithelial stem/progenitor cell hierarchy in the adult mouse lung," *Proc Natl*

Acad Sci U S A, vol. 107, no. 4, pp. 1414–1419, Jan. 2010, doi: 10.1073/PNAS.0909207107.

[163] A. M. Hoffman *et al.*, "Lung-derived mesenchymal stromal cell post-transplantation survival, persistence, paracrine expression, and repair of elastase-injured lung," *Stem Cells Dev*, vol. 20, no. 10, pp. 1779–1792, Oct. 2011, doi: 10.1089/SCD.2011.0105.

[164] M. A. Matthay, "Therapeutic potential of mesenchymal stromal cells for acute respiratory distress syndrome," *Ann Am Thorac Soc*, vol. 12, no. Suppl 1, pp. S54–S57, Mar. 2015, doi: 10.1513/ANNALSATS.201406-254MG/SUPPL_FILE/DISCLOSURES.PDF.

[165] S. Moradinasab, A. Pourbagheri-Sigaroodi, P. Zafari, S. H. Ghaffari, and D. Bashash, "Mesenchymal stromal/stem cells (MSCs) and MSC-derived extracellular vesicles in COVID-19-induced ARDS: Mechanisms of action, research progress, challenges, and opportunities," *Int Immunopharmacol*, vol. 97, p. 107694, Aug. 2021, doi: 10.1016/J.INTIMP.2021.107694.

[166] W. Wang *et al.*, "Therapeutic mechanisms of mesenchymal stem cells in acute respiratory distress syndrome reveal potentials for Covid-19 treatment," *Journal of Translational Medicine 2021 19:1*, vol. 19, no. 1, pp. 1–13, May 2021, doi: 10.1186/S12967-021-02862-X.

[167] O. Levy *et al.*, "Shattering barriers toward clinically meaningful MSC therapies," *Sci Adv*, vol. 6, no. 30, Jul. 2020, doi: 10.1126/SCIADV.ABA6884.

[168] G. Siegel, T. Kluba, U. Hermanutz-Klein, K. Bieback, H. Northoff, and R. Schäfer, "Phenotype, donor age and gender affect function of human bone marrow-derived mesenchymal stromal cells," *BMC Med*, vol. 11, no. 1, p. 146, Jun. 2013, doi: 10.1186/1741-7015-11-146.

[169] G. Kaur and J. M. Dufour, "Cell lines: Valuable tools or useless artifacts," *Spermatogenesis*, vol. 2, no. 1, p. 1, Jan. 2012, doi: 10.4161/SPMG.19885.

[170] X. X. Chen, L. Tang, Z. H. Han, W. J. Wang, and J. G. Meng, "Coculture with bone marrow-derived mesenchymal stem cells attenuates inflammation and apoptosis in lipopolysaccharide-stimulated alveolar epithelial cells via enhanced secretion of keratinocyte growth factor and angiopoietin-1 modulating the Toll-like receptor-4 signal pathway," *Mol Med Rep*, vol. 19, no. 3, pp. 1891–1902, Mar. 2019, doi: 10.3892/MMR.2019.9836.

[171] A. Jauković *et al.*, "Specificity of 3D MSC Spheroids Microenvironment: Impact on MSC Behavior and Properties," *Stem Cell Reviews and Reports 2020 16:5*, vol. 16, no. 5, pp. 853–875, Jul. 2020, doi: 10.1007/S12015-020-10006-9.

[172] C. H. Masterson *et al.*, "Intra-vital imaging of mesenchymal stromal cell kinetics in the pulmonary vasculature during infection," *Sci Rep*, vol. 11, no. 1, Dec. 2021, doi: 10.1038/S41598-021-83894-7.

[173] C. H. Masterson *et al.*, "Mesenchymal stem/stromal cell-based therapies for severe viral pneumonia: therapeutic potential and challenges," *Intensive Care Medicine Experimental* , vol. 9, no. 1, pp. 1–21, Dec. 2021, doi: 10.1186/S40635-021-00424-5/TABLES/4.

[174] M. Lopes-Pacheco, C. Robba, P. R. M. Rocco, and P. Pelosi, "Current understanding of the therapeutic benefits of mesenchymal stem cells in acute respiratory distress syndrome," *Cell Biol Toxicol*, vol. 36, no. 1, pp. 83–102, Feb. 2020, doi: 10.1007/S10565-019-09493-5/TABLES/4.

[175] M. N. Islam *et al.*, "Mitochondrial transfer from bone-marrow-derived stromal cells to pulmonary alveoli protects against acute lung injury," *Nat Med*, vol. 18, no. 5, pp. 759–765, May 2012, doi: 10.1038/NM.2736.

[176] L. Richart *et al.*, "XIST loss impairs mammary stem cell differentiation and increases tumorigenicity through Mediator hyperactivation," *Cell*, vol. 185, no. 12, pp. 2164-2183.e25, Jun. 2022, doi: 10.1016/J.CELL.2022.04.034.

[177] F. McNab, K. Mayer-Barber, A. Sher, A. Wack, and A. O'Garra, "Type I interferons in infectious disease," *Nat Rev Immunol*, vol. 15, no. 2, p. 87, Feb. 2015, doi: 10.1038/NRI3787.

[178] S. v. Kotenko, A. Rivera, D. Parker, and J. E. Durbin, "Type III IFNs: Beyond antiviral protection," *Semin Immunol*, vol. 43, p. 101303, Jun. 2019, doi: 10.1016/J.SMIM.2019.101303.

[179] N. A. Jewell *et al.*, "Lambda Interferon Is the Predominant Interferon Induced by Influenza A Virus Infection In Vivo," *J Virol*, vol. 84, no. 21, p. 11515, Nov. 2010, doi: 10.1128/JVI.01703-09.

[180] S. A. Cook and S. Schafer, "Hiding in Plain Sight: Interleukin-11 Emerges as a Master Regulator of Fibrosis, Tissue Integrity, and Stromal Inflammation," *https://doi.org/10.1146/annurev-med-041818-011649*, vol. 71, pp. 263–276, Jan. 2020, doi: 10.1146/ANNUREV-MED-041818-011649.

[181] A. A. Widjaja *et al.*, “Inhibiting Interleukin 11 Signaling Reduces Hepatocyte Death and Liver Fibrosis, Inflammation, and Steatosis in Mouse Models of Nonalcoholic Steatohepatitis,” *Gastroenterology*, vol. 157, no. 3, pp. 777-792.e14, Sep. 2019, doi: 10.1053/J.GASTRO.2019.05.002.

[182] S. Allanki *et al.*, “Interleukin-11 signaling promotes cellular reprogramming and limits fibrotic scarring during tissue regeneration,” *Sci Adv*, vol. 7, no. 37, Sep. 2021, doi: 10.1126/SCIADV.ABG6497/SUPPL_FILE/SCIADV.ABG6497_TABLES_S1_TO_S6.ZIP.

[183] W. Yang *et al.*, “Interleukin-11 regulates the fate of adipose-derived mesenchymal stem cells via STAT3 signalling pathways,” *Cell Prolif*, vol. 53, no. 5, May 2020, doi: 10.1111/CPR.12771.

[184] M. Mastri *et al.*, “Activation of toll-like receptor 3 amplifies mesenchymal stem cell trophic factors and enhances therapeutic potency,” *Am J Physiol Cell Physiol*, vol. 303, no. 10, Nov. 2012, doi: 10.1152/AJPCELL.00191.2012/ASSET/IMAGES/LARGE/ZH002112706500 10.JPEG.

[185] M. Najar *et al.*, “Empowering the immune fate of bone marrow mesenchymal stromal cells: gene and protein changes,” *Inflammation Research*, vol. 68, no. 2, pp. 167–176, Feb. 2019, doi: 10.1007/S00011-018-1198-8.

[186] M. H. Tsai, L. M. Pai, and C. K. Lee, “Fine-tuning of type I interferon response by STAT3,” *Front Immunol*, vol. 10, no. JUN, p. 1448, Jun. 2019, doi: 10.3389/FIMMU.2019.01448/BIBTEX.

[187] K. Mahboubi *et al.*, “Interleukin-11 Up-Regulates Survivin Expression in Endothelial Cells through a Signal Transducer and Activator of Transcription-3 Pathway,” *Laboratory Investigation 2001 81:3*, vol. 81, no. 3, pp. 327–334, Mar. 2001, doi: 10.1038/labinvest.3780241.

[188] B. Ng, S. A. Cook, and S. Schafer, “Interleukin-11 signaling underlies fibrosis, parenchymal dysfunction, and chronic inflammation of the airway,” *Experimental & Molecular Medicine 2020 52:12*, vol. 52, no. 12, pp. 1871–1878, Dec. 2020, doi: 10.1038/s12276-020-00531-5.

[189] L. Chen *et al.*, “Mesenchymal stem cell-based treatments for COVID-19: status and future perspectives for clinical applications,” *Cellular and Molecular Life*

Sciences, vol. 79, no. 3, pp. 1–33, Mar. 2022, doi: 10.1007/S00018-021-04096-Y/FIGURES/4.

[190] S. M. R. Hashemian *et al.*, "Mesenchymal stem cells derived from perinatal tissues for treatment of critically ill COVID-19-induced ARDS patients: a case series," *Stem Cell Res Ther*, vol. 12, no. 1, Dec. 2021, doi: 10.1186/S13287-021-02165-4.

[191] Y. Feng *et al.*, "Safety and feasibility of umbilical cord mesenchymal stem cells in patients with COVID-19 pneumonia: A pilot study," *Cell Prolif*, vol. 53, no. 12, Dec. 2020, doi: 10.1111/CPR.12947.

[192] G. Lanzoni *et al.*, "Umbilical cord mesenchymal stem cells for COVID-19 acute respiratory distress syndrome: A double-blind, phase 1/2a, randomized controlled trial," *Stem Cells Transl Med*, vol. 10, no. 5, pp. 660–673, May 2021, doi: 10.1002/SCTM.20-0472.

[193] Z. Leng *et al.*, "Transplantation of ACE2 - Mesenchymal Stem Cells Improves the Outcome of Patients with COVID-19 Pneumonia," *Aging Dis*, vol. 11, no. 2, pp. 216–228, 2020, doi: 10.14336/AD.2020.0228.

IX. Supplements

IX.1. Chemicals and Consumables

Chemicals/Consumables	Manufacturer
αMEM	Gibco
0.5 mm iSpacers IS008	SunJin Lab Co
1.5 mL vials	Eppendorf
100 µm, 40 µm and 20 µm cell filters	Sarstedt
12 mm cell culture inserts	Merck
145 µm Cell Imaging Dishes	Eppendorf
15 mL polypropylene tubes	Corning
15 mL polystyrene tubes	Corning
6, 12, 24, 48 and 96 tissue culture well-plates	Greiner
Acetic acid	Merck
Agarose	Roth
Alcian Blue	Sigma-Aldrich
Alizarin Red S	Merck
Amphotericin B	Sigma-Aldrich
AnnexinV buffer	Biolegend
ATCC-DMEM	ATCC
Avicel®	FCM
Biotin-linked magnetic beads	Life Technologies
Bovine calf serum	ATCC
BSA	Sigma-Aldrich
DEAE-Dextran	Thermo Fisher Scientific
dH2O	Braun
Dispase	Corning Life Science
DMEM	Gibco
DMSO	PAN
DNAse I	Serva
eBioscience™ Foxp3/Transcription Factor Staining Buffer Set	Thermo Fisher Scientific
EDTA	Roth
Eosin	Merck
EtOH	Merck
FBS	Life Technologies
Formalin	Sigma-Aldrich
HCL	Merck
Hematoxylin	Merck
Heparin	StemCell Technologies
HEPES	Merck
Horse serum	Sigma-Aldrich
Insulin	Biozym Scientific

Isoflurane	Baxter
Isopropanol	Merck
KPL TrueBlue™ Substract	Seracare
L-Glutamine	StemCell Technologies
Lipofectamine™ RNAiMAX transfection reagent	Thermo Fisher Scientific
LysoTracker™ Green DND-26	Thermo Fisher Scientific
MACS C-tubes	Milteny Biotec
MACS dissociator	Milteny Biotec
Matrigel®	Corning
MEM	Gibco
MesenCult™ Adipogenic Stimulatory Kit Mouse: MesenCult™ MSC Basal Media Mouse and MesenCult™ Adipogenic Differentiation 10X Supplement Mouse	StemCell Technologies
MesenCult™ Expansion Kit Mouse: MesenCult™ Basal Medium Mouse and MesenCult™ 10X Supplement Mouse	StemCell Technologies
MesenCult™ Osteogenic Stimulatory Kit Mouse: MesenCult™ MSC Basal Media Mouse and MesenCult™ Osteogenic Stimulatory Supplement Mouse	StemCell Technologies
MesenCult™-ACF Chondrogenic Differentiation Kit: MesenCult™-ACF Chondrogenic Differentiation Basal Medium and MesenCult™-ACF Chondrogenic Differentiation 20X Supplement	StemCell Technologies
Methanol	Merck
Mouse IFNα ELISA Kit	R&D Systems
Mouse IFNβ ELISA Kit	R&D Systems
Mouse IFNγ Quantikine ELISA Kit	R&D Systems
Mouse IL-11 DuoSet ELISA	R&D Systems
NucBlue ® Fixed/Live Cell Stain ReadyProbes™ reagent Dapi Special Formulation	Thermo Fisher Scientific
Oil Red O	Sigma-Aldrich
Opti-MEM	Gibco
Paraffin	Sigma-Aldrich
PBS	Life Technologies
Pen/Strep	Gibco
Pen/Strep/L-Glu	Gibco
PFA	Merck
PVP	Sigma-Aldrich
Qtracker® Cell Labelling Kit 625	Thermo Fisher Scientific
RLT buffer	Qiagen
RNeasy Micro Kit	Qiagen
Saccomano Fixation Solution	Morphisto
Sandoglobulin	Novartis
Silencer® Select IL-11	Thermo Fisher Scientific

Sodium bicarbonate	Sigma-Aldrich
Stem-Pro® Accutase®	Thermo Fischer Scientific
Thermo Scientific™ Pierce™ Protein Concentrators PES	Thermo Fisher Scientific
Transwells (12 well-plates)	Costar
Triton X-100	Sigma-Aldrich
Trypsin	Worthington Biochemical
Trypsin-EDTA	PAN
Tween-20	Sigma-Aldrich
Ultra-low melting agarose	Roth
Xylol (Neo-Clear)	Sigma-Aldrich

IX.2. List of Abbreviations

2D, 3D	Two dimensional and three dimensional
AEC, AEC1, AEC2	Alveolar epithelial cells (type 1 or type 2)
AEnC	Alveolar endothelial cells
ALI	Acute lung injury
Ang-1	Angiopoietin 1
ARDS	Acute respiratory distress syndrome
AT	Adipose tissue
BALF	Bronchoalveolar lavage fluid
BALO	Bronchoalveolar lung organoid
BASC	Bronchoalveolar stem cells
BM	Bone marrow
BM-MSC	Bone Marrow derived mensenchymal stem cells
BMP	Bone morphogenetic protein
BSA	Bovine serum albumine
CCL	C-C motif ligand
cm^2	Centimeters square
CO_2	Carbon dioxide
COPD	Chronic obstructive pulmonary disease
COVID-19	Corona virus disease 2019
CXCL	C-X-C motif chemokine ligand
DCs	Dendritic cells
DEAE	Diethylaminoethyl
dH_2O	Distilled water
DMEM	Dulbecco's Modified Eagle's Medium
DMSO	Dimethylsulfoxid
DNA	Deoxyribonucleic acid
dpi	Days post infection
E.coli	*Escherichia coli*
EDTA	Ethylenediamine tetraacetic acid
EGF	Epidermal growth factor
ELISA	Enzyme-linked immunosorbent assay
ENaCs	Epithelial sodium channels
EtOH	Ethanol
EVs	Extracelular vesicles
FACS	Flow activated cell sorting
FBS	Fetal bovine serum
ffu	Foci forming units
FGF	Fibroblast growth factor
FiO_2	Fraction of inspired oxygen
g	Grams
GM-CSF	Granulocyte-macrophage colony-stimulating factor
h	Hour

H&E	Hematoxylin/eosin
HA	Hemagglutinin
HBSS	Hank's balanced salt solution
HEPES	N-(2-Hydroxyethyl)piperazine-N′-(2-ethanesulfonic acid)
HGF	Hepatocyte growth factor
hpi	Hours post infection
IAV	Influenza A virus
ICAM-1	Intercellular adhesion molecule 1
IDO	Indoleamine 2,3 dioxygenase
IFN	Interferon
IFNAR	Type I IFN receptor
IGF	Insulin-like growth factor 1
IL	Interleukin
IL1-ra	Interleukin 1 receptor antagonist
iNOS	Inducible nitric oxide synthase
ISCT	International Society for Cellular Therapy
IT	Intra-tracheal
KGF	Keratinocyte growth factor
Krt5	Keratin 5
LH	Lung homogenate
LNEPs	Lineage-negative epithelial progenitors
LPS	Lipopolysaccharide
m^2	Meters square
MAVS	Mitochondria associated antiviral signaling
MDCK II	Madin-Darby canine kidney II
MEM	Minimum Essential Media
MHC	Major histocompatibility complex
min	Minutes
MIP	Macrophage inflammatory protein
miRNA	Micro ribonucleic acid
ml	Milliliters
mm	Millimeters
mM	Millimolar
MOI	Multiplicity of infection
mRNA	Messenger ribonucleic acid
MSC	Mesenchymal Stem Cells
mT/mG	B6.129(Cg)-Gt(ROSA)26Sor$^{tm4(ACTB-tdTomato,-EGFP)Luo}$/J
NA	Neuraminidase
NK cell	Natural killer cell
nm	Nanometers
NP	Viral nucleoprotein
PaO_2	Partial pressure of arterial oxygen
PBS	Phosphate buffer saline

PD-L	Programmed cell death ligands
PDGF	Platelet-derived growth factor
PDGFRα or CD140a	Platelet-derived growth factor receptor alpha
Pen/Strep	Penicillin/streptomycin
Pen/Strep/L-Glu	Penicillin/streptomycin/L-glutamine
PFA	Paraformaldehyde
PGE2	Prostaglandin E_2
PR8	A/Puerto Rico/8/1934 H1N1
PVP	Polyvinylpyrrolidone
QC	Quality control
RIG-1	Retinoic acid inducible gene 1
RNA	Ribonucleic acid
RNAseq	RNA sequencing
ROS	Reactive oxygen species
RT	Room temperature
SARS-Cov-2	Severe acute respiratory syndrome-coronavirus-2
Sca-1	Stem cell antigen 1
SCGB1A1	Secretoglobulin family 1A member 1
SEM	Standard error of mean
SFTPC	Pro-surfactant protein C
siRNA	Silencing RNA
Sox	Sex determining region Y-box transcription factor
SpO_2	Peripheral capillary oxygen saturation
TGF-β	Transforming growth factor beta
TLR	Toll-like receptor
TNF	Tumor necrosis factor
Trp63	Transformation related protein 63
TSG-6	Tumor necrosis factor-inducible gene 6 protein
UC	Umbilical cord
v-club cells	Variant club/secretory cells
VCAM-1	Vascular cell adhesion molecule 1
VE-cadherin	Vascular endothelial cadherin
VEGF, VEGFR	Vascular endothelial growth factor and receptor
WT	Wildtype
xg	Relative centrifugal force
µl	Microliters
µm	Micrometers
^oC	Celsius

IX.3. List of Figures

Figure I-1. Lung cell lineages involved in lung repair and regeneration. In both human and mouse, the lung architecture and cell lineages are similar, with both species having alveolar type 1 and alveolar type 2 epithelial cells, as well as secretory cells, multi-ciliated cells, and various mesenchymal lineages (mesenchymal support cell, $Axin2^{+}$ myogenic precursor and mesenchymal alveolar niche cells). However, humans have a pseudostratified epithelium in the intermediate airways (containing secretory, goblet and ciliated cells) while mice do not have respiratory bronchioles and the intermediate airways exhibit a pseudostratified nature without basal cells. The murine distal region contains a population of bronchoalveolar stem cell (BASC). Adapted from M.C. Basil et al., 2020 [1]. Created using BioRender.com. 5

Figure I-2. Mechanisms of injury and repair in the alveolus after IAV-infection. (Left side) Injured alveolus after IAV-infection. Released pro-inflammatory cytokines activate inflammation, leading to epithelial injury and neutrophil migration. The epithelial-endothelial barrier integrity is lost, with cell death, disruption of gap junctions and impaired fluid clearance. **(Right side)** Repaired alveolus after IAV-infection. The release of factors contributes to AEC2 proliferation and differentiation into AEC1, indispensable for the restitution of the epithelial barrier. Pro-resolving macrophages eliminate dead cells and debris, helping in restoring endothelial integrity and fluid clearance. AEC1 alveolar epithelial cell type 1, AEC2 alveolar epithelial cell type 2, BASC bronchoalveolar stem cell. Adapted from M.A. Matthay *et al,* 2019 [36]. Created using BioRender.com. 10

Figure I-3. Immune modulators and immune suppressive potential of MSC. MSC express immune modulators both in quiescent and activated states. Some modulators are expressed in basal concentrations on the quiescent state but are upregulated upon activation – iNOS or IDO, TGF-β, IL-10, PGE2, HGF and CCL2. PD-L1 and PD-L2 are only expressed in the activated state. All modulators are upregulated by pro-inflammatory factors in the concentration-dependent manner. In the activated state, MSC have immunosuppressive potential, that can directly impact the proliferation and inhibition of T-cells, NK-cells, and DC, among others. The soluble factors released by MSC that play a key role in these effects are IDO, PGE2, IL-10 and IL-6, PD-1 and -2, TGF-β and HGF. CCL2 C-C motif chemokine ligand 2, DC dendritic cells, HGF hepatocyte growth factor, IDO indoleamine 2,3-dioxygenase, IL-10 interleukin-10, IL-6 interleukin-6, iNOS inducible nitric oxide synthase, MSC mesenchymal stem cells, NK-cell natural killer cell, PD-L1 and PD-L2 programmed cell death ligands 1 and 2, PGE2 prostaglandin E2, TGF-β transforming growth factor beta.

Adapted from W. Jiang et al. 2019 [113], Q.Zhao *et al.* 2016 [60] and F. van den Akker *et al.* 2013 [105]. Created using BioRender.com. 15

Figure I-4. MSC therapeutic potential in ARDS. The beneficial effects of MSC in the context of ARDS include their production of paracrine factors, mitochondrial transfer, release of extracellular vesicles, cell-to-cell contact, and integration with the damages tissue. The secretion of Ang-1, IL1-ra and PGE2 by MSC can decrease epithelial and endothelial cell permeability, while release of TSG-6, IGF-1 and Lipoxin A4 (and IL1-ra) reduces inflammation. Monocyte and macrophage phagocytosis is increased by MSC production of IL-6 and FGF-7 (also contributes for improving alveolar fluid clearance). Extracellular vesicles from MSC containing genetic information (mRNA and miRNA), soluble factors and proteins also contribute to tissue repair. Mitochondria are efficiently transfer from MSC to alveolar and bronchial epithelium, airway smooth muscle cells and alveolar macrophages by overexpression of Miro1. Lastly, MSC can physically communicate with the damaged tissue, differentiate, and effectively integrate in the host. Ang-1 angiopoietin 1, FGF-7 fibroblast growth factor 7, IGF-1 insulin-like growth factor 1, IL1-ra interleukin 1 receptor antagonist, IL-6 interleukin 6, mRNA messenger ribonucleic acid, miRNA micro ribonucleic acid, MSC mesenchymal stem cells, PGE2 prostaglandin E_2, TSG-6 tumor necrosis factor-inducible gene 6 protein. Adapted from C. Li *et al.,* 2019 [138], L.A. Huppert *et al.,* 2019 [122], S.C. Abreu *et al.,* 2016 [139] and X.L Fan *et al.,* 2020 [140]. Created using BioRender.com. 17

Figure IV-1. Lung-MSC isolation from adult murine lungs. Gating strategy for cell sorting of lung-MSC after lung homogenization. After leukocyte, endothelial and epithelial exclusion, the cell suspension was subjected to doublet discrimination and live-cell selection ($SYTOX^+$), with the mesenchymal population being sorted based on the $CD45^-$ $CD31^-$ $EpCAM^-$ $PDGFR\alpha^+$ $Sca\text{-}1^+$ expression signature. 34

Figure IV-2. Heatmap and Gene Set Enrichment for mock (PBS) or PR8 isolated lung-MSC. (A) Heatmap of top 50 differently expressed genes (DEG) from lung-MSC recovered from mock (PBS) or 3 dpi PR8 infected mice. Red squares represent upregulated genes and blue squares represent downregulated genes, with Z-score from -2 to 2. N=3 biological replicates. **(B-C)** DEG up and down regulated after gene set enrichment using KOBAS, with each graph representing the top 10 gene sets or pathways enriched from **(B)** gene ontology or **(C)** PANTHER databases. Dashed line represents a p-value=0.05. log10 FDR are represented as dark green for significantly upregulated in PR8, light green for not-significant up-regulation in PR8, dark red for significantly downregulated in PR8 and light red for not-significant down-regulation in PR8. 35

Figure IV-3. Lung-MSC protective effects towards iAEC *in vitro*. (A) Proliferation, **(B)** apoptosis and **(C)** NP expression of mock (black) and infected (MOI 0.1, PR8) (red) AEC co-cultured with and without lung-MSC after 24 and 48 hpi (N=4 biological replicates). AEC alveolar epithelial cells, hpi hours post infection, iAEC infected alveolar epithelial cells, MSC mesenchymal stem cells, MOI multiplicity of infection. Bar charts presented as mean ± SEM and probability determined using one-way ANOVA (*p<0.05, **p<0.01, ***p<0.001, ****p<0.0001). 37

Figure IV-4. BM-MSC isolation from healthy adult murine bone marrow. Gating strategy for cell sorting of BM-MSC after bone flushing. The cell population was subjected to doublet discrimination and live-cell selection ($SYTOX^+$), with sorted mesenchymal population having a $CD45^-$ $Ter119^-$ $CD31^-$ $PDGFR\alpha^+$ $Sca\text{-}1^+$ signature. 38

Figure IV-5. BM-MSC characterization. (A) Flow cytometric histograms of surface expression in BM-MSC of negative (CD11b, CD45, CD31, CD19 and CD34) and positive (Sca-1, PDGFRα, CD105, CD44 and CD117) markers after 15 passages. Red histograms represent isotype control and blue histograms represent stained sample. **(B)** Microscopic images of BM-MSC 7 days after flow cytometric isolation and after 15 passages. **(C)** Microscopic images of BM-MSC differentiation into adipocytes, chondrocytes, and osteocytes after 15 passages. Arrows represent (a) nuclei staining in blue using hematoxylin, (b) lipid droplets stained with Oil Red O, (c) acidic polysaccharides present in cartilage spheroids stained with Alcian Blue and (d) extracellular calcium deposits produced by osteocytes stained with Alizarin Red. Scale bars represent 144 µm. 39

Figure IV-6. BM-MSC proliferative, anti-apoptotic and anti-viral effects towards iAEC *in vitro*. (A) Proliferation, **(B)** apoptosis and **(C)** NP expression of mock (black dots) and infected (MOI 0.1, PR8) (red dots) AEC co-cultured with and without BM-MSC for 24 hpi and 48 hpi (N=4 biological replicates). AEC alveolar epithelial cells, hpi hours post infection, iAEC infected alveolar epithelial cells, BM-MSC bone marrow-derived mesenchymal stem cells, MOI multiplicity of infection. Bar charts presented as mean ± SEM and probability determined using one-way ANOVA (*p<0.05, **p<0.01, ***p<0.001, ****p<0.0001). 40

Figure IV-7. Recovery of TexasRed-BM-MSC from adult 3-day mock- or PR8- infected murine lung homogenate. (A) Example of gating strategy (6 h after cell instillation) used in FACS to recover TexasRed-BM-MSC delivered 3 dpi from mock (PBS) or PR8 infected (500 ffu) murine lungs. The cell population was subjected to doublet exclusion and live-cell selection ($SYTOX^+$), with the sorted mesenchymal population being $CD45^-$ $Ter119^-$ $CD31^-$ $EpCAM^-$ $TexasRed^+$. **(B)** Percentage of FACS recovered TexasRed-BM-MSC after 3 h, 6 h,

12 h or 24 h post-instillation. Cells were intra-tracheally delivered 3 days after mock-PBS (black) or PR8 (red) infection. N=4 biological replicates. Bar charts presented as mean ± SEM and probability determined using two-way ANOVA (*p<0.05, **p<0.01, ***p<0.001, ****p<0.0001). 42

Figure IV-8. Heatmaps of top 50 expressed genes in AEC flow-sorted from healthy lungs, and from mock or PR8 infected lungs (3 dpi, 500 ffu) IT injected with BM-MSC (for 6 h). (A) Graphical representation of AEC isolation conditions. AEC (green) represent alveolar epithelial cells flow sorted from healthy lungs, AEC MOCK (grey) represents AEC flow sorted from mock-infected (PBS) lungs, treated with BM-MSC 3 days after mock infection, and AEC PR8 (red) represents AEC flow sorted from 500 ffu PR8-infected lungs, treated at 3 dpi with BM-MSC. **(B-D)** Heatmaps highlighting the **(B)** comparison between AEC and AEC MOCK, **(C)** comparison between AEC and AEC PR8 and **(D)** comparison between AEC MOCK and AEC PR8. In the heatmaps, Z-score Row are presented as red squares for the most upregulated genes and blue squares for most downregulated genes. N=4 biological replicates for all groups. 44

Figure IV-9. Gene set enrichment from flow-sorted AEC, isolated from 3 dpi mock (PBS) or PR8 infected (500 ffu) murine lungs, IT injected with BM-MSC (for 6 h). DEG up and down regulated genes after gene set enrichment using KOBAS, with graph representing the top 10 gene sets or pathways enriched from gene ontology database. Dashed line represents a pvalue=0.05. log10 FDR are represented as dark green for significantly upregulated in AEC MOCK, light green for not-significant up-regulation in AEC MOCK, dark red for significantly downregulated in AEC MOCK and light red for not-significant down-regulation in AEC MOCK. N=4 biological replicates for all groups. 45

Figure IV-10. Heatmaps of top 50 expressed genes in BM-MSC isolated from bone marrow, and flow sorted back after 6 h post-injection in mock (PBS) and PR8 infected lungs (3 dpi, 500 ffu). (A) Graphical representation of BM-MSC isolation conditions. MSC (green) represent BM-MSC isolated from bone marrow of healthy animals, MSC MOCK (grey) represent BM-MSC flow sorted from mock-infected (PBS) lungs, delivered 3 days after PBS injection, and MSC PR8 (red) represent BM-MSC flow sorted from 3 days after PR8-infection (500 ffu). **(B-D)** Heatmaps highlighting the (**B)** comparison between MSC and MSC MOCK, **(C)** comparison between MSC and MSC PR8 and **(D)** comparison between MSC MOCK and MSC PR8. In the heatmaps, Z-score Row are presented as red squares for the most upregulated genes and blue squares for most downregulated genes. N=4 biological replicates in MSC and MSC MOCK and N=5 biological replicates for MSC PR8. 46

Figure IV-11. Gene set enrichment from flow-sorted IT injected BM-MSC (6 h), isolated from 3 dpi (500 ffu) mock (PBS) or PR8 infected murine lungs. DEG up and down regulated genes after gene set enrichment using KOBAS, with graph representing the top 10 gene sets or pathways enriched from gene ontology database. Dashed line represents a pvalue=0.05. log10 FDR are represented as dark green for significantly upregulated in MSC MOCK, light green for not-significant up-regulation in MSC MOCK, dark red for significantly downregulated in MSC MOCK and light red for not-significant down-regulation in MSC MOCK. N=4 biological replicates for all groups. 47
Figure IV-12. BALO development using lung-MSC or BM-MSC. Microscopic images of cysts and developed BALO through time (from day 4 to day 21). Lung-MSC **(upper row)** or naïve BM-MSC **(bottom row)** were co-cultured with BASCs for BALO development. Scale bars represent 180µm. Micrographs are representative of n=6 experiments. 48
Figure IV-13. BALO development using naïve- or activated-BM-MSC. Microscopic images of BALO (day 21) stained with LysoTracker (green). Naïve BM-MSC **(left image)** or CM-iAEC (conditioned media from 48 hpi iAEC – PR8, MOI 0.1) activated-BM-MSC **(right image)** were co-cultured with BASCs for BALO generation. Scale bars represent 144µm. Micrographs are representative of n=6 experiments. 48
Figure IV-14. BALO development using differently activated BM-MSC. (A) Confocal microscopy images from naïve or differently activated BM-MSC (CM iAEC, conditioned media from iAEC (PR8, 48 h, MOI 0.1) or bronchoalveolar lavage fluid (BALF) from day 0, day 3 and day 7 infected murine lungs (PR8, 500 ffu)). Organoids stained with DAPI (nuclei, blue) and LysoTracker (AEC2, green). Scale bars represent 83µm. **(B)** BALO quantification and **(C)** BALO alveolarization of day 21 BALO using BM-MSC non-stimulated or stimulated with CM from iAEC (PR8, 48 h, MOI 0.1) and BALF from day 0, 3 or 7 infected mice (PR8, 500 ffu) (n=6 biological replicates). Bar charts presented as mean ± SEM and probability determined using one-way ANOVA (*p<0.05, **p<0.01, ***p<0.001, ****p<0.0001). 50
Figure IV-15. BALF day 3 activated BM-MSC have a proliferative, anti-apoptotic and anti-viral effect towards iAEC *in vitro*. (A) Proliferation, **(B)** apoptosis and **(C)** NP expression of infected AEC (MOI 0.1, PR8) co-cultured (24 hpi and 48 hpi) with non-stimulated (n.s.) or BALF day 3 (BALFD3) stimulated BM-MSC. N=4 for n.s. BM-MSC cultures and for 48 hpi BALFD3-BM-MSC cultures and N=8 for BALFD3-BM-MSC cultured for 24 hpi. Bar charts presented as mean ± SEM and probability determined using one-way ANOVA (*p<0.05, **p<0.01, ***p<0.001, ****p<0.0001). 51

Figure IV-16. *In vivo* experiment of infected (500 ffu, PR8) WT mice, treated at day 3pi with PBS, 3T3, BM-MSC or BALFD3-MSC. (A) Kaplan-Maier curve of 500 ffu PR8-infected mice treated at day 3 post-infection with PBS (blue), 3T3 (red), naïve BM-MSC (green) or BALF day 3 stimulated-BM-MSC (purple). N=8 biological replicates per group. Probability determined using t-test (*p<0.05, **p<0.01, ***p<0.001, ****p<0.0001). **(B)** Histology of PFA/ paraffin-embedded murine lungs at day 7 post infection (500 ffu, PR8), treated at 3 dpi with PBS, 3T3, BM-MSC or BALFD3 stimulated-BM-MSC. Lung slides were stained with haematoxylin and eosin. Scale bars represent 240µm. 52

Figure IV-17. Naïve- and BALFD3 BM-MSC protective effects towards iAEC *in vivo*. (A) Proliferation, **(B)** apoptosis and **(C)** NP expression of the iAEC population recovered from 7 dpi (500ffu, PR8) mice treated with PBS (blue), 3T3 (red), BM-MSC (green) or BALFD3-BM-MSC (purple) (n=4 biological replicates). Bar charts presented as mean ± SEM and probability determined using one-way ANOVA (*p<0.05, **p<0.01, ***p<0.001, ****p<0.0001). 53

Figure IV-18. IFNs concentrations present in conditioned media used to stimulate BM-MSC. Analysis of mIFNα (blue), mIFNβ (green), and mIFNγ (purple) concentration in conditioned media used to stimulated naïve BM-MSC, performed by ELISA (n=3 biological replicates). CM iAEC, conditioned media from iAEC (MOI 0.1, 48 h, PR8) and BALF, bronchoalveolar lavage fluid from non-infected (BALFD0) or day 3 (BALFD3) infected mice (500ffu, PR8). Bar charts presented as mean ± SEM. 54

Figure IV-19. Effects of BM-MSC stimulation with mIFNα or mIFNβ on iAEC *in vitro*. (A) Proliferation, **(B)** apoptosis and **(C)** viral presence of iAEC (MOI 0.1, PR8) co-cultured with mIFNα (blue) or mIFNβ (green) stimulated BM-MSC, 24 hpi (n=4 biological replicates). Bar charts presented as mean ± SEM and probability determined using one-way ANOVA (*p<0.05, **p<0.01, ***p<0.001, ****p<0.0001). 55

Figure IV-20. BM-MSC protective effects towards iAEC rely on IFN signaling *in vitro*. Proliferation **(A)**, apoptosis **(B)** and viral presence **(C)** of iAEC (MOI 0.1, PR8) co-cultured with either WT or IFNAR$^{-/-}$ BM-MSC 24hpi (n=6 biological replicates). Bar charts presented as mean ± SEM and probability determined using t-test (*p<0.05, **p<0.01, ***p<0.001, ****p<0.0001). 56

Figure IV-21. *In vivo* experiment of infected (500 ffu, PR8) WT and IFNAR$^{-/-}$ mice, treated at 3 dpi with WT- or IFNAR$^{-/-}$- BM-MSC. (A) Kaplan-Maier curve of 500 ffu PR8 infected WT mice treated at 3 dpi with IFNAR$^{-/-}$ BM-MSC (blue) and IFNAR$^{-/-}$ mice treated at 3 dpi with either WT BM-MSC (red) or IFNAR$^{-/-}$ BM-MSC (green). N=8 biological

replicates and probability determined using t-test (*p<0.05, **p<0.01, ***p<0.001, ****p<0.0001). **(B)** Histology of PFA/paraffin-embedded WT or IFNAR$^{-/-}$ mice lungs at day 7 post infection (500 ffu, PR8), treated at 3 dpi with WT or IFNAR$^{-/-}$ BM-MSC. Lung slides were stained with haematoxylin and eosin. Scale bars represent 240µm. 57

Figure IV-22. WT- and IFNAR$^{-/-}$-BM-MSC protective effects towards *in vivo* infected AEC. **(A)** Proliferation, **(B)** apoptosis and **(C)** NP expression of the AEC population recovered from 7-day infected WT or IFNAR$^{-/-}$ mice (500ffu, PR8) treated with WT- or IFNAR$^{-/-}$-BM-MSC (N=4 biological replicates). Bar charts presented as mean ± SEM and probability determined using t-test (*p<0.05, **p<0.01, ***p<0.001, ****p<0.0001)..... 57

Figure IV-23. Infected BALO (Cre-H7N7) treated with WT-, BALFD3-, or BALFD3-IFNAR$^{-/-}$ BM-MSC. mT/mG BALO (magenta) were infected for 1 h with Cre-H7N7 (green) and fixed after 24 hpi. (A) Confocal image representing a IAV-Cre infected BALO, microinjected with BM-MSC. Scale-bar represent 121µm. **(B)** Infected area ratio, calculated from total BALO area divided by infected area, using data obtained by confocal microscopy. N=5 biological replicates for no treatment, N=7 biological replicates for WT BM-MSC, N=8 biological replicates for BALFD3 BM-MSC and N=5 biological replicates for BALFD3-IFNAR$^{-/-}$ BM-MSC. Bar charts presented as mean ± SEM and probability determined using one-way ANOVA (*p<0.05, **p<0.01, ***p<0.001, ****p<0.0001)..... 58

Figure IV-24. IL-11 concentration in stimulated WT- and IFNAR$^{-/-}$ BM-MSC. Analysis of IL-11 concentration (pg/ml) in supernatants after WT- or IFNAR$^{-/-}$- BM-MSC stimulation with IFNα, IFNβ and concentrated BALF from d3 and d7 infected (PR8, 500 ffu) mice. Performed by ELISA (n=3 biological replicates). Bar charts presented as mean ± SEM and probability determined using one-way ANOVA (*p<0.05, **p<0.01, ***p<0.001, ****p<0.0001). 59

Figure IV-25. Recombinant mIL-11 treatment of *in vitro* iAEC. (A) Proliferation, **(B)** apoptosis and **(C)** NP expression of non-infected (AEC, black dots) and infected (iAEC, red dots, MOI 0.1, PR8) AEC treated with 50 ng/mL of mIL-11 for 24 hpi (n=4 biological replicates). n-t, no treatment. Bar charts presented as mean ± SEM and probability determined using two-way ANOVA (*p<0.05, **p<0.01, ***p<0.001, ****p<0.0001). 60

Figure IV-26. Foci assay from IL-11 treated iAEC. Foci assay on the supernatants of non-treated (n-t) and 24 h treated (50 ng/ml and 100 ng/ml) iAEC (MOI 0.1, PR8) (n=4 biological replicates). Bar charts presented as mean ± SD and probability determined using two-way ANOVA. 60

Figure IV-27. Silencing IL-11 in BM- MSC. Analysis of IL-11 concentration (pg/mL) in supernatants from scrambled or siIL-11 treated BM-MSC, not stimulated (black dots) and stimulated with mIFNα (blue) or mIFNβ (green), performed by ELISA (n=3 biological replicates). Bar charts presented as mean ± SEM. 61
Figure IV-28. *In vivo* experiment of infected (500 ffu, PR8) WT mice, treated at 3 dpi with scrambled siRNA BM-MSC or siRNA-IL-11 BM-MSC. (A) Kaplan-Maier curve of 500 ffu PR8 infected WT mice treated at 3 dpi with scrambled siRNA BM-MSC (blue) or siRNA-IL-11 BM-MSC (red). N=6 biological replicates per group, points presented as mean ± SEM and probability determined using t-test (not significant, p=0.16). **(B)** Histology of PFA/paraffin-embedded WT lungs at day 7 post infection (500 ffu, PR8), treated at 3 dpi with scrambled siRNA BM-MSC (blue) or siRNA-IL-11 BM-MSC (red). Lung slides were stained with haematoxylin and eosin. Scale bars represent 240 µm. 62
Figure IV-29. Scrambled siRNA control- and siIL-11 BM-MSC effects towards infected AEC *in vivo*. (A) Proliferation, **(B)** apoptosis and **(C)** NP expression of the iAEC population recovered from 7-day infected mice (500 ffu, PR8) treated with scrambled siRNA control-BM-MSC (blue) or siIL-11 BM-MSC (red) (n=12 biological replicates). Bar charts presented as mean ± SEM and probability determined using one-way ANOVA (*p<0.05, **p<0.01, ***p<0.001, ****p<0.0001). 63
Figure IV-30. Infected BALO (Cre-H7N7) treated with scrambled- or si-IL11 BM-MSC. mT/mG BALO (magenta) were infected for 1 h with Cre-H7N7 (green) and fixed after 24 hpi. (A) Confocal image representing a H7N7-infected BALO, microinjected with siRNA IL-11 BM-MSC. Scale-bar represent 121µm. **(B)** Infected area ratio, calculated from total BALO area divided by infected area, using data obtained by confocal microscopy. BALO was infected, and not-treated (N=6 biological replicates) or injected with scrambled- (N=9 biological replicates) or siRNA IL-11 BM-MSC (N=8 biological replicates) and fixed after 24 h. Bar charts presented as mean ± SEM and probability determined using one-way ANOVA (*p<0.05, **p<0.01, ***p<0.001, ****p<0.0001). 63
Figure VI-1. Schematic representation of type I IFN (iAEC) / IL-11 (BM-MSC) signaling axis. IT-applied BM-MSC (3 dpi, 500 ffu, IV-PR8) are activated with type I IFNs, released by iAEC. After activation, BM-MSC secrete IL-11 that ultimately improves iAEC resilience. IV, influenza virus; EpiSPC, epithelial progenitor cells; BM-MSC, bone marrow derived mesenchymal stem cells; IFNs, interferons; AEC, alveolar epithelial cells. Created using BioRender. 70

IX.4. List of Tables

Table III-1. Scoring criteria approved for *in vivo* experiments. 20
Table III-2. Antibodies, media volume and biotinylated beads calculations for AEC isolation. 22
Table III-3. Staining antibodies and respective dilutions for lung-MSC isolation with FACS. 22
Table III-4. Staining antibodies and respective dilutions for BM-MSC isolation with FACS. 23
Table III-5. Staining antibodies and respective dilutions for BM-MSC characterization in flow cytometry. 24
Table III-6. Staining antibodies for proliferation, infection, and apoptosis analysis of AEC. 27
Table III-7. Staining antibodies and respective dilutions for sorting BASC with FACS, for the generation of BALO. 29
Table III-8. Staining antibodies and respective dilutions for FACS recovery of labelled BM-MSC. 31

IX.5. Affirmation

I declare that I have completed this dissertation single-handedly without the unauthorized help of a second party and only with the assistance acknowledged therein. I have appropriately acknowledged and referenced all text passages that are derived literally from or are based on the content of published or unpublished work of others, and all information that relates to verbal communications. I have abided by the principles of good scientific conduct laid down in the charter of the Justus Liebig University of Giessen in carrying out the investigations described in the dissertation.

Gießen, 2023

_____

Margarida Maria Barroso

IX.6. Curriculum vitae

General information

Name Margarida Maria Pacheco Barroso

Academic Background

2017-Present, PhD thesis on "Therapeutic reprogramming of bone marrow derived mesenchymal stem cells during influenza infection is mediated by type I interferon signaling and interleukin 11", realized on Department of Medicine V, Internal Medicine, Infectious Diseases and Infection Control of the University Hospital Gießen and Marburg (UKGM) with supervision of Prof. Dr. Susanne Herold.

2017-2019, International Graduate Program on Molecular Biology and Medicine of the Lung, Universities of Gießen and Marburg Lung Center, Gießen, Germany.

2014-2016, Master in Science in Biotechnology by Instituto Superior Técnico da Universidade de Lisboa, Lisbon, Portugal. Master thesis in Stem Cell Bioengineering and Regenerative Medicine Laboratory (BERG, IST) on "Expansion of adipose-derived stem/stromal cells under dynamic culture conditions", supervised by Dr. Cláudia Lobato da Silva and Dr. Ana Margarida Platzgummer.

2011-2014, Bachelor in Science in Biochemistry by Faculdade de Ciências e Tecnologias da Universidade Nova de Lisboa, Lisbon, Portugal. Graduation in Molecular Biophysics, with bachelor thesis entitled "Expression and characterization studies of ferredoxin and rubredoxin from *Marinobacter hydrocarbonoclasticus* in *E.coli*" and supervised by Prof. Pedro Tavares and Prof. Alice Pereira.

Presentations

February 2018, Deutsches Zentrum fur Lungenforschung (DZL) Annual Meeting, Bad Nauheim. Poster presentation on "Mesenchymal (stem) cell heterogeneity and plasticity in influenza virus-induced lung injury: impact on therapeutic pre-conditioning to improve antiviral and tissue- regenerative MSC properties".

February 2019, Deutsches Zentrum fur Lungenforschung (DZL) Annual Meeting, Mannheim. Poster presentation on "Mesenchymal Stem Cell Plasticity and Therapeutic Programming in Acute Lung Injury".
May 2019, American Thoracic Society International Conference 2019 Dallas, Texas. Poster presentation on "Mesenchymal Stem Cell Plasticity and Therapeutic Programming in Acute Lung Injury".
June 2019, 5th International ARDS Conference (Berlin). Oral presentation entitled "Mesenchymal Stem Cell Plasticity and Therapeutic Programming in Acute Lung Injury".

January 2020, Deutsches Zentrum fur Lungenforschung (DZL) Annual Meeting, Travemunde. Poster presentation and poster teaser on "Anti-viral/anti-apoptotic effects of BM-MSC – a type I IFN signaling mediated response".

September 2021, Thomas L. Petty Aspen Lung Conference, 63rd Annual Meeting "ARDS in the 21st Century: New Insights into Clinical and Mechanistic Heterogeneity". Poster presentation on virtual poster session with "Anti-viral and anti-apoptotic effects of BM-MSC – a response mediated by type I IFN and IL-11".
September 2021, Deutsches Zentrum fur Lungenforschung (DZL) Online Annual Meeting. Poster presentation on "Anti-viral and anti-apoptotic effects of BM-MSC – a response mediated by type I IFN and IL-11".
September 2021, Cardio-Pulmonary Institute (CPI) Retreat, Frankfurt. Poster presentation on "Anti-viral and anti-apoptotic effects of BM-MSC – a response mediated by type I IFN and IL-11".

May 2022, American Thoracic Society International Conference 2022 San Francisco, California. Poster presentation on "Reprograming of Bone Marrow Mesenchymal Stem cells during Viral Kung Infection is Mediated by Type I Interferon Signaling and Interleukin 11 Axis".
June 2022, Cardio-Pulmonary Institute (CPI) Retreat, Bad Nauheim. Poster presentation and poster teaser on "Reprograming of Bone Marrow Mesenchymal Stem cells during Viral Kung Infection is Mediated by Type I Interferon Signaling and Interleukin 11 Axis"
July 2022, Deutsches Zentrum fur Lungenforschung (DZL) Annual Meeting, Hannover. Poster presentation on "Reprogramming of Bone Marrow Mesenchymal Stem Cells during Viral Lung Infection is Mediated by Type I Interferon Signaling and Interleukin 11 Axis".

February 2023, Keystone Symposium: Stem Cells – advances in the application of stem cells and their role *in vivo.* Poster presentation on "Reprogramming of Bone Marrow Mesenchymal Stem Cells during Viral Lung Infection is Mediated by Type I Interferon Signaling and Interleukin 11 Axis".

March 2023, European Respiratory Society, Lung Science Conference: Post-viral lung diseases – from basic immunology to clinical phenotypes and therapy. Poster presentation on "Reprogramming of Bone Marrow Mesenchymal Stem Cells during Viral Lung Infection is Mediated by Type I Interferon Signaling and Interleukin 11 Axis".

Publications

Barroso, M.M., A.I. Vazquez, L. Jankauskaite, T. Braun, and S. Herold. 2019. "Mesenchymal Stem Cell Plasticity and Therapeutic Programming in Acute Lung Injury." *American Thoracic Society International Conference Meetings Abstracts*, May, A5754–A5754. https://doi.org/10.1164/ajrccm-conference.2019.199.1_MeetingAbstracts.A5754

Barroso, M.M., A.I. Vazquez, L. Jankauskaite, S. Günther, T. Braun, and S. Herold. 2022. "Reprogramming of Bone Marrow Mesenchymal Stem Cells During Viral Lung Infection Is Mediated by Type I Interferon Signaling and Interleukin-11 Axis." *American Thoracic Society International Conference Meetings Abstracts*, May, A2522–A2522. https://doi.org/10.1164/ajrccm-conference.2022.205.1_MeetingAbstracts.A2522

Vazquez-Armendariz, A.I., **Barroso, M.M.,** El Agha, E., Herold, S. 3D In Vitro Models: Novel Insights into Idiopathic Pulmonary Fibrosis Pathophysiology and Drug Screening. *Cells* 2022, *11*, 1526. https://doi.org/10.3390/cells11091526

Kheirollahi, V., Khadim, A., Kiliaris, G., Korfei, M., **Barroso, M.M.,** Alexopoulos, I., Vazquez-Armendariz, A.I., Wygrecka, M.; Ruppert, C., Guenther, A., Seeger, W., Herold, S., El Agha, E. Transcriptional Profiling of Insulin-like Growth Factor Signaling Components in Embryonic Lung Development and Idiopathic Pulmonary Fibrosis. *Cells* 2022, *11*, 1973. https://doi.org/10.3390/cells11121973

Awards and Honors

May 2019, American Thoracic Society International Conference 2019 Dallas, Texas – Abstract Scholarship Award.

July 2022, Deutsches Zentrum fur Lungenforschung (DZL) Annual Meeting, Hannover – Poster Prize Award in Disease Area Pneumonia and Acute Lung Injury.

IX.7. Acknowledgments

My perseverance throughout these years would not be the same without the support of all these people. To them, I would like to express my sincere appreciation and gratitude for all their contributions.

To Prof. Dr. Susanne Herold, my supervisor, I show my deepest appreciation for the opportunity I was given to pursue my doctoral studies with a project I fell in love with from the moment it was presented to me. For all her guidance, advice and challenges that shaped the scientist I am today, I will be forever grateful. Also, a special thank you to Dr. Elie El Agha for accompanying me since I first started my PhD journey and guiding me through scientific challenges.

A very special thank you to Dr. Ivonne Vazquez-Armendariz for her guidance, expertise, and (a lot of) patience. Together with all the friendship, the scientific discussions during lunch or coffee breaks gave me most of the ideas presented here today. Without her support and knowledge, I would not have been ready to deal with science like I am today. I hope this thesis makes you proud.

To Prof. Dr. Thomas Braun, Dr. Ewelina Betleja and Dr. Isabelle Salwig from Max Plank Institute for Heart and Lung Research (Bad Nauheim), thank you for all our opinions, ideas and help in shaping this project. Also, to Dr. Stefan Günther, thank you for the assistance and knowledge provided in RNA-bulk sequencing. To Dr. Balachandar Selvakumar and Dr. Maximiliano Ferrero, and all the team in Max-Planck Heart and Lung Laboratory (MP-HL lab) at IbioBA, a special thank you for guiding me in Buenos Aires and allowing me to perform essential experiments under their supervision.

To all my lab mates that have worked closely to me, a very special thank you for keeping the (in)sanity in the laboratory so refreshing. It was a pleasure to share my journey with Monika, Theresa, Anna-Lena, Marie, Ioannis, Irina, Ali, Georgios, Ully, Learta, Julian and Mo. A very special thank you to my office partner, Christina, whose extensive discussions greatly contributed to my personal and scientific development. To Steffi, Florian, Larissa and Julia, thank you for all the assistance in the laboratory. To my MBML-friends, thank you for your

support and encouragement. To Despina, a special acknowledgement for all the friendship during these challenging years – you were my family far from home.

Um agradecimento especial à minha família que sempre me apoiou a perseguir os meus sonhos e me amou incondicionalmente durante todo este processo. Para os meus pais, Luís e Maria José, e para a minha irmã Matilde, um agradecimento escrito nunca vai ser suficiente para retribuir tudo o que fizeram por mim. Espero que esta tese vos deixe orgulhosos. Aos meus avós, Lurdinhas, Odete e Elmano, e aos meus tios Paula e Nuno (e Joana), obrigada por sempre acreditarem em mim. Ao meu avô Zé, um eterno agradecimento cheio de saudade.

To João, my chosen family, I can never thank enough for being my emotional and physical support for everything I do. Thank you for believing in me even when I had the highest doubts, for transforming this "international experience" into a home, and for all the love and respect. To you, I am forever grateful. Also, a big appreciation to the cat who chose me, Rosie.

"Happiness can be found, even in the darkest of times,
if one only remembers to turn on the light."
— *Albus Dumbledore.*